Université Fédérale
Toulouse Midi-Pyrénées

THÈSE

En vue de l'obtention du
DOCTORAT DE L'UNIVERSITÉ DE TOULOUSE

Délivré par l'Université Toulouse 3 - Paul Sabatier

Présentée et soutenue par

Linjie ZHENG

Le 26 août 2021

Structure, solvation, thermodynamics and fragmentation of molecular clusters

Ecole doctorale : **SDM - SCIENCES DE LA MATIERE - Toulouse**

Spécialité : **Physico-Chimie Théorique**

Unité de recherche :
LCPQ-IRSAMC - Laboratoire de Chimie et Physique Quantiques

Thèse dirigée par
Jérôme CUNY et Mathias RAPACIOLI

Jury

Mme Céline TOUBIN, Rapporteure
Mme Carine CLAVAGUÉRA, Rapporteure
Mme Julie DOUADY, Examinatrice
M. Romuald POTEAU, Examinateur
M. Jérôme CUNY, Directeur de thèse
M. Mathias RAPACIOLI, Co-directeur de thèse

- **Ionic bond** which exists in ionic clusters such as NaCl[23] or NaF clusters.[24]

Properties of clusters stem from both their size and composition. Clusters can therefore exhibit very specific physical and chemical properties that are strongly influenced by their structures, which themselves are strongly determined by the number of atoms or molecules they are made of. Furthermore, when a given cluster of a well defined composition switches between different stable configurations, chemical and physical properties can also be strongly impacted. For instance, for different conformational isomers of small Ni and Fe clusters, compact structures are more stable than open structures and the photoabsorption spectra of two isomers of Ni_4 are different.[25] This becomes all the more true as the chemical complexity of the cluster increases, *i.e.* when it consists of more than one chemical element, for instance several types of molecules for a molecular cluster or different atoms for an atomic cluster. Depending on the cluster type, see above, intermolecular interactions can be rather weak.[26] This is true for atomic or molecular clusters when cohesion is governed by Van der Waals and/or hydrogen-bond interactions. In that case, the potential energy surface (PES), or energy landscape, can be extremely complex and a large variety of local minima displaying equivalent stabilities exist. The properties of a given cluster can significantly differ from the properties of the corresponding bulk material. For instance, the magnetic moment of small iron particles at room temperature is smaller than that of the bulk.[27] However, a gradual transition occurs between the properties of the clusters and those of the corresponding bulk as cluster size increases.[28] This transition can be rough or continuous depending on the considered species and properties. For instance, U. Landman *et al.* reported that anionic gold clusters favor planar structures up to $\sim$13 atoms.[4] J.-M. L'Hermite *et al.* also reported that the transition temperature extracted from he heat capacity curve of protonated water clusters $(H_2O)_nH^+$ has a strong size dependence as seen in Figure 1.1.[29] Consequently, the study of clusters allow to bridge the gap between single molecule or atom properties and bulk materials, which can be of help in revealing microscopic aspects which are hardly observable in the bulk only.

The field of cluster research can be traced back to 1857 when M. Faraday gave his lecture entitled "*Experimental Relation of (Colloidal) Gold to Light*" which paved the way for modern work on both metal clusters and the interaction of photons with clusters.[32] Cluster research has since drawn a lot of interest and the field has undergone a dramatic growth which can be explained by two main reasons. The first one is the **development of efficient and accurate characterization techniques**. Indeed, experimental techniques now enable the investigation of

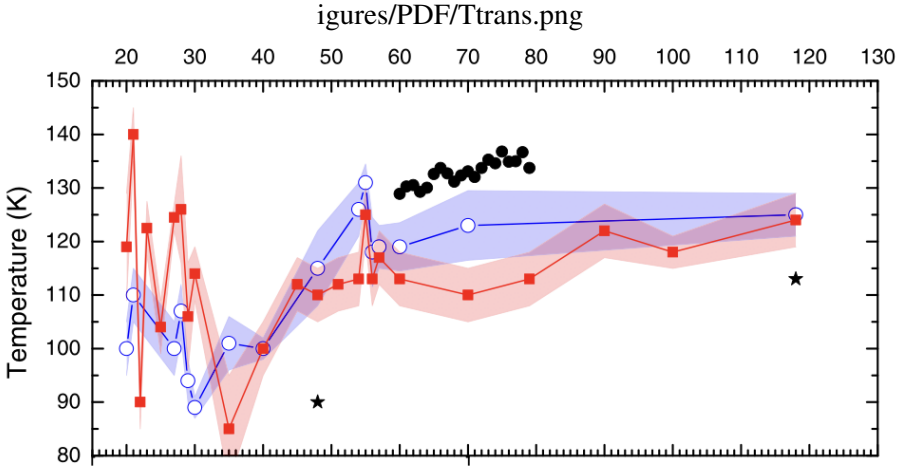

Figure 1.1: Transition temperature of $(H_2O)_nH^+$ clusters (red squares) and $(H_2O)_{n-1}OH^-$ (blue circles) as a function of n. The results obtained by M. Schmidt *et al.* on $(H_2O)_nH^+$ are also presented (black circles)[30] as well as those by C. Hock *et al.* on $(H_2O)_n^-$ clusters (black stars).[31] Figure extracted from reference [29].

clusters of interest in several scientific domains such as astrophysics and astrochemistry,[16] atmospheric physico-chemistry,[33] biochemistry,[34] and environmental science.[35] With the help of mass spectrometer, well-defined cluster sizes can now be isolated and observed.[36] The advent of the laser technology also provides a new dimension to the field as it enables detailed spectroscopic observations.[37] The second reason is related to **application of clusters**. Indeed, clusters may offer ways to develop new kinds of materials,[38] to carry out chemical reactions in new ways,[39] and to gain new kinds of understanding of bulk matter by learning how the bulk properties emerge from properties of clusters as the cluster grows larger and larger.[28] For instance, the study of clusters has provided new insights into phase transition, e.g. condensation of gas mixtures,[40] evaporation,[41] precipitation,[42] solidification of liquid mixtures[43] and melting of solids.[44] The study of clusters also helps to understand nucleation phenomena, for instance the formation of nanoscale materials and aerocolloids, as well as ultrafine particles.[45, 46, 47, 48] Study of clusters in gas phase can provide detailed structural, energetic, and spectroscopic information which are hardly accessible from measurements on the bulk.[49, 50, 51, 52] Finally, clusters containing organic/inorganic molecules or ions and water molecules can be viewed as intermediates between a dilute gas phase and a solution. Consequently, their study allows to explore the effects of solvents on the chemistry

2

Computational Methods

Chemistry is a central scientific discipline dealing with the construction, transformation and properties of molecules. It provides a foundation for understanding both basic and applied scientific disciplines at a fundamental level.[153] Chemistry started out as an experimental science. So, historically, all the chemical processes studied and the theories developed have been through experience. However, with the development of theoretical concepts dealing with the structure of matter and with recent developments in computer technology, a new trend in chemical research has developed: **theoretical chemistry**. **Computational chemistry**, as a subfield of theoretical chemistry, combines fundamental laws with mathematical methods to solve chemical problems through calculations or simulations. Nowadays, modelling of physico-chemical properties has become a important part of research in science of matter and the role of computational chemistry has become fundamental. However, when resorting to computational chemistry, one always has to choose **a balance between accuracy and computational efficiency**.

There exist many methods to model the interactions between different particles in atomic or molecular aggregates. Some of them are depicted in Figure 2.1 and are classified in terms of system sizes (y-axis) and simulation times (x-axis) they can tackle. If focusing on the y-axis, the closer a given method is from the origin of the graph, the more accurate it is. The farther from the origin a method is, the larger are the system sizes it can simulate. For instance, **force fields** (FF), also referred to as **molecular mechanics** (MM) methods, describe the interactions between particles by empirical interatomic potentials and electrons are not treated explicitly. FF methods thus bypass the solving of the **Schrödinger equation** and the quantum aspects of nuclear motion are neglected which allow them to model very large systems. On the opposite,

electronic structures methods such as **full configuration interaction** (Full CI) make it possible to describe electron distributions with a very high accuracy but only for very small systems.

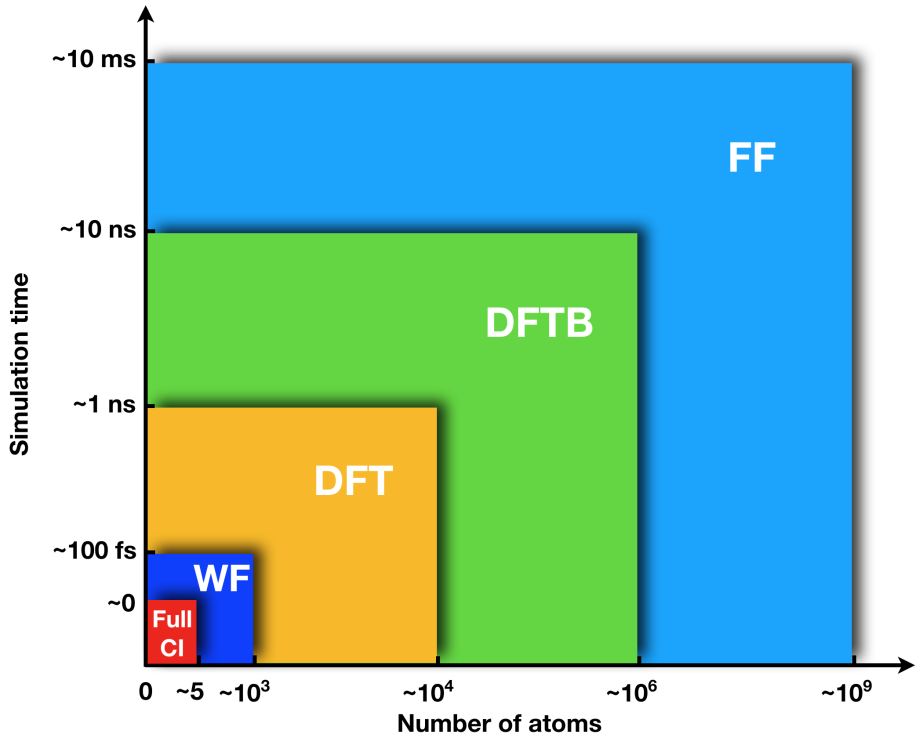

Figure 2.1: Comparison of the computational efficiency, *i.e.* system sizes and simulation times, of various computational chemistry methods. The *y*-axis indicates the length of time accessible from classical molecular simulations for average system sizes tackle by each method. The *x*-axis indicates the approximative maximum system size tractable by each method in a single-point energy calculation.

In parallel to the accuracy, the ability of a given method to efficiently and accurately explore PES is also of paramount importance to model a variety of properties. Here also, different methods allow for different possibilities. For instance, the multi-configuration time-dependent Hartree (MCTDH) method allows for a full quantum treatment of the nuclear degrees of freedom as long as only a limited number of them is taken into account.[154] For large systems, to access time-dependent information, one has to resort to **molecular dynamics simulations** which is dealt with **classical mechanics**, *i.e.* Newton's second law.

This chapter gives a brief description of the theoretical foundations of the computational methods that were used during this thesis. Two main aspects are developed. First, I de-

2.4 Exploration of PES

The PES is a function giving the energy of a system according to one or more nuclear coordinates. If there is only one coordinate, the PES is called the energy profile or potential energy curve. Figure 2.3 is a model of PES in two dimension. The analogy of a hilly landscape with peaks, valleys, mountain passes helps to understand the PES. Stable molecular structures correspond to the minima in the valleys on a PES. The shape of the valley around a minimum determines the vibrational spectrum. The key points on a PES can be classified according to the first and all second derivatives of the energy with respect nuclear coordinates, which correspond to the gradients and the curvatures, respectively. The points have a zero gradient (stationary points) and their second derivatives are positive, they correspond to **local minima** (physically stable structure). Among these local minima, the lowest energy minimum is called the **global minimum**. When at least one of the second derivatives is negative, the point is a transition state (saddle point).

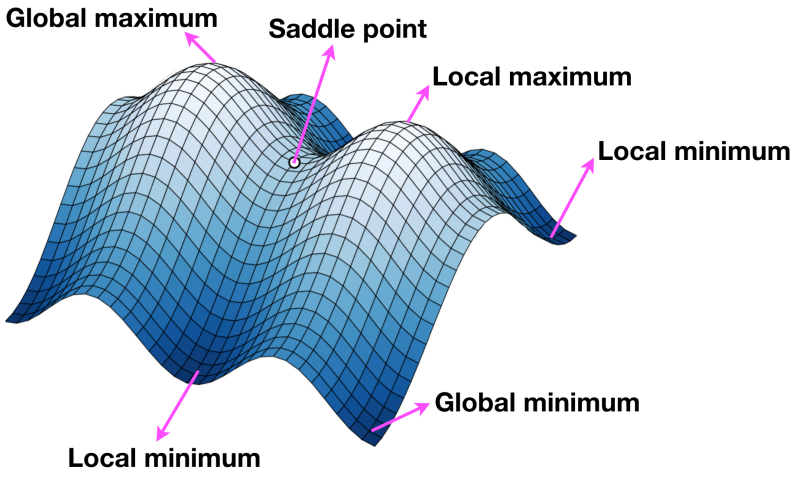

Figure 2.3: Schematic representation of some key points on a model potential energy surface.

Molecular structure, properties, chemical reactivity, dynamics, and vibrational spectra of molecules can be readily understood in terms of PES. Only very simple PES can be obtained from experiment whereas computational chemistry has developed different kinds of methods to efficiently explore PES. To survey the PES, the choice of an exploration method can be guided by the shape of the PES (the statistical set that one wishes to study) and the temporal aspect.

Monte Carlo and classical **MD** simulations are widely recognized approaches for the exploration of PES of systems containing a large number of degrees of freedom such as molecular

aggregates. Monte Carlo methods allow the sampling of a PES by performing random shifts in order to correctly reproduce the probability distribution of the configurations which are accessible from the phase space of a system as a function of state variables such as temperature, energy, or number of particles. One of the main advantages of Monte Carlo methods is that they do not require the calculation of gradients. In MD simulations, one needs to numerically integrate Newton's equations of motion of the interacting particles. One can then obtain statistical properties by performing time averaging along the resulting deterministic trajectory in phase space. **Parallel-tempering molecular dynamics** (PTMD) is an improvement of classical MD that allows for a more efficient sampling of the PES. The Monte Carlo, classical MD and PTMD methods are briefly described in the following sections.

2.4.1 Monte Carlo Simulations

The term Monte Carlo denotes a class of algorithmic methods that aims at a probabilistic description, relying on the use of random numbers. The name Monte Carlo alludes to the games of chance taking place at the Monte Carlo casino. The Monte Carlo method was introduced in 1947 by N. Metropolis,[256] and was first published in 1949 by N. Metropolis in collaboration with S. Ulam.[151] Monte Carlo methods have been widely applied in computational physics, computational statistics, biomedicine, machine learning, industrial engineering, economics and finance, and other fields.[257] **Monte Carlo methods can** generally be roughly **divided into two categories**. The first category is applied to problems that have inherent randomness, and the computing power of the computer can directly simulate this random process. For example, in nuclear physics, analysis of the transmission process of neutrons in a reactor. The second category applies to problems that can be transformed into randomly distributed characteristic numbers, such as the probability of a random event. Through the random sampling method, the probability of random events is estimated by the frequency of occurrence, and this is used as the solution to the problem. This method is usually used to solve complicated multi-dimensional integration problems. Monte Carlo methods are mainly used in the field of optimization, numerical integration, and generating draws from a probability distribution.

To illustrate the general application of Monte Carlo techniques, here the standard example of the one-dimensional integral I over integration space Ω is taken:

$$I = \int_{\Omega} f(\mathbf{x}) d\mathbf{x} \tag{2.56}$$

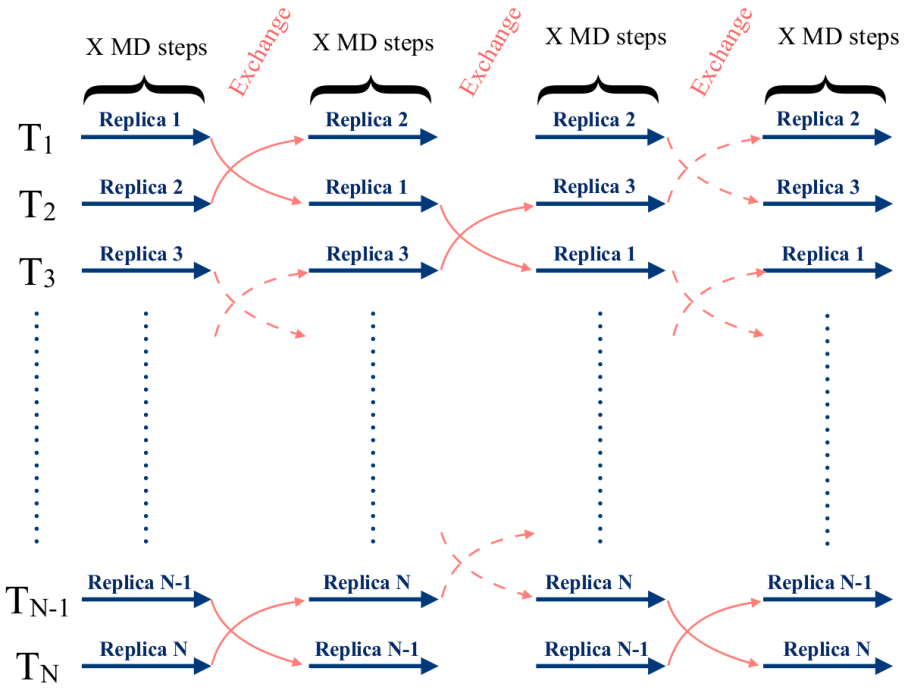

Figure 2.4: Schematics of the PTMD algorithm in its synchronous version. Replicas of the same system, numbered from C_1 to C_N, are simulated subject to different temperatures (from T_1 to T_N). Once X MD steps (straight solid arrows) have been performed by each replica, configuration exchanges are attempted between neighbouring simulations according to the Metropolis criterion. Some of them undergo successful swapping (solid curved arrows) while other not (dashed curved arrows). MD simulations then proceed for X additional MD steps before new attempts of exchange.

replica is independent with each other but exchanges of configurations between adjacent replicas C_i and C_j, where $T_i < T_j$ and $i = j - 1$ are permitted at regular time intervals. The choice of the extreme temperatures T_1 and T_N is very important for the algorithm to be optimal. The lowest temperature (T_1) should be the one at which usual simulations are blocked in basins and the highest temperature (T_N) should be chosen so that all significant energy barriers can be overcome during the simulation. Moreover, the temperatures between T_1 and T_N must be chosen to lead to sufficient overlap between the density of states of the adjacent replicas. Indeed, if this overlap is too small, the probability of exchange is very low, which makes the PTMD simulations inefficient and leads to a bad exploration of the PES. In contrast, if the overlap is too large, a significant amount of redundant information will be produced, which will cost unnecessary computational resources. Configurations between two neighbouring replicas at

different T are exchanged based on the Metropolis–Hastings criterion with probability:

$$\rho(C_i \Leftrightarrow C_j) = \min\left(1, e^{(V_i - V_j)\left(\frac{1}{kT_i} - \frac{1}{kT_j}\right)}\right) = \min(1, e^m) \tag{2.78}$$

where V_i and V_j are the potential energies of replicas i and j, respectively. T_i and T_j are the temperatures of replicas i and j, respectively. If the energy of replica configuration C_j at high temperature T_j is lower than the energy of replica configuration C_i at low temperature T_i, which means the exponent (m) of e is positive, then the exchange is allowed. If m is negative, the exchange between neighbouring replicas is only allowed when e^m is greater than ω (a random value between 0 and 1). To accelerate the equilibration of the system after the exchange, the velocities of all particles can be renormalized as follows:

$$\mathbf{v}_\alpha^{\text{new}} = \left(\frac{T_{\text{new}}}{T_{\text{old}}}\right)^{\frac{1}{2}} \mathbf{v}_\alpha^{\text{old}} \tag{2.79}$$

2.4.4 Global Optimization

Global optimization refers to the determination of the lowest energy point on a PES, *i.e.* the global minimum. As this latter usually includes a large number of stationary points, it is not straightforward to find the global minimum. Local optimization methods do not make it possible to cross the energy barriers between local minima. Therefore, a global optimization scheme such as MD or Monte Carlo simulations is needed to perform a more exhaustive exploration of the PES to get to the lowest energy minimum.

There exits a vast amount of methods to perform global optimization and each one has its strength and weaknesses. The ergodicity problem appears in all of these global optimization methods. In principle, one can only be sure of having found the real global minimum after an infinite number of iterations. The Basin-Hopping method is a particular useful global optimization technique in high-dimensional landscapes that iterates by performing a random perturbation of coordinates, making a local optimization, and rejecting or accepting new coordinates based on a minimized function value.[58, 60] Genetic algorithms are also among the most used methods to find a global minimum.[329, 330, 331, 332] A genetic algorithm is inspired by the process of natural selection. Genetic algorithms are usually applied to generate high-quality solutions of optimization.

In order to avoid ergodicity problems, an interesting tool is to combine global and local optimization methods. A very popular combination is the simulated annealing method combined with local optimizations. The PTMD algorithm coupled with a great number of local

For $(H_2O)_{4-10,20}NH_4^+$ and $(H_2O)_{4-10}NH_3$ clusters, 500 geometries were periodically selected from each replicas leading to 20000 optimized geometries per cluster. For $(H_2O)_{20}NH_4^+$, the initial structure used for the global optimization process was the lowest-energy structure reported by J. Douady *et al.*[340] The five lowest-energy isomers among the 4848 or 20000 optimized geometries were further optimized using the MP2/Def2TZVP method. See below for the details on MP2/Def2TZVP calculations.

Detailed parameters for PTMD simulations of $(H_2O)_{1-7,11,12}UH^+$ clusters are as follows. 40 replicas with temperatures ranging linearly from 50 to 350 K were used. Each trajectory was 4 ns long, and the integration time step was 0.5 fs. A reasonable time interval for the PT exchanges was 2.5 ps. A Nosé-Hoover chain of five thermostats with frequencies of 800 cm^{-1} was applied to achieve an exploration in the canonical ensemble.[310, 311] To avoid any spurious influence of the initial geometry on the PES exploration, three distinct PTMD simulations were carried out with distinct initial proton location: on the uracil in two cases and on a water molecule in the other one. In the former cases, I used two isomers u178 and u138 of UH^+ shown in Figure 3.1 as the initial geometries.[341, 342] 600 geometries per temperature were periodically selected along each PTMD simulation for subsequent geometry optimization leading to 72000 structures optimized at SCC-DFTB level. These structures were sorted in ascending energy order and checked for redundancy. 9, 23, 46, 31, 38, 45, 63, 20, and 29 structures were then selected for $(H_2O)UH^+$, $(H_2O)_2UH^+$, $(H_2O)_3UH^+$, $(H_2O)_4UH^+$, $(H_2O)_5UH^+$, $(H_2O)_6UH^+$, $(H_2O)_7UH^+$, $(H_2O)_{11}UH^+$ and $(H_2O)_{12}UH^+$ respectively, to perform geometry optimizations at the MP2/Def2TZVP level. See below for the details on MP2/Def2TZVP calculations.

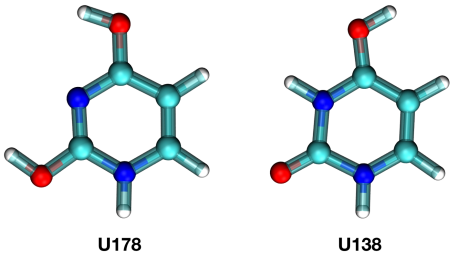

Figure 3.1: Structures of the two protonated uracil isomers, u178 (keto-enol form) and u138 (di-keto form), used as initial conditions in the PTMD simulations.

3.1.3 MP2 Geometry Optimizations, Relative and Binding Energies

Some low-energy isomers obtained at the SCC-DFTB level were further optimized at the MP2 level of theory in combinationwith an all electron Def2TZVP basis-set.[343, 344] All calculations used a tight criteria for geometry convergence and an ultrafine grid for the numerical integration. All MP2 calculations were performed with the Gaussian 09 package.[345]

Detailed parameters for $(H_2O)_{1-10,20}NH_4^+$ and $(H_2O)_{1-10}NH_3$ clusters. Following SCC-DFTB optimizations, the five lowest-energy isomers of $(H_2O)_{1-10}NH_4^+$ and $(H_2O)_{1-10}NH_3$ clusters were further optimized at the MP2/Def2TZVP level of theory. In section 3.2, relative energy with respect to the lowest-energy isomer of each cluster will be shown. Impact of zero-point vibrational energy (ZPVE) corrections on relative energies were evaluated at MP2/Def2TZVP level. To evaluate the strength of water-ammonium and water-ammonia interactions and to assess the accuracy of the SCC-DFTB method, binding energies are also calculated. Two distinct approaches were used to calculate binding energies. The first one considers only the binding energy between the water cluster as a whole and the impurity, NH_4^+ or NH_3 that the corresponding binding energy is denoted as $E_{bind.}^{whole}$, while the second one considers the binding energy between all the molecules of the cluster corresponding to $E_{bind.}^{sep.}$. In both cases, the geometry of the molecules is the one found in the optimized cluster. Using these two methods, relative binding energies ($E_{bind.}$(SCC-DFTB)-$E_{bind.}$(MP2/Def2TZVP)) $\Delta E_{bind.}^{whole}$ and $\Delta E_{bind.}^{sep.}$ were obtained. For all binding energies of $(H_2O)_{1-10}NH_4^+$ and $(H_2O)_{1-10}NH_3$ clusters calculated at MP2/Def2TZVP level, basis set superposition errors (BSSE) correction was considered by using the counterpoise method of Boys and Bernardi.[346]

Detailed parameters for $(H_2O)_{1-7,11,12}UH^+$ clusters. Following SCC-DFTB optimizations, the six lowest-energy isomers of $(H_2O)_{1-7,11,12}UH^+$ clusters were further optimized at the MP2/Def2TZVP level of theory. The binding and relative energies calculated at MP2/Def2TZVP level without BSSE correction of clusters $(H_2O)_{2-7,11,12}UH^+$ are discussed in section 3.3.

3.1.4 Structure Classification

To classify clusters $(H_2O)_{1-10}NH_4^+$ and $(H_2O)_{1-10}NH_3$, "n-x"and "n′-x" labels are used to distinguish between the reported $(H_2O)_nNH_4^+$ and $(H_2O)_nNH_3$ isomers, respectively, obtained at the SCC-DFTB level. In these notations, n and n′ denote the number of water molecules in the ammonium and ammonia water clusters, respectively. x is an alphabetic character going from a to e that differentiates between the five low-energy isomers reported for each cluster

In this section, I first propose an improvement of the SCC-DFTB scheme to describe ammonium and ammonia water clusters by modifying both Hamiltonian and overlap N-H integrals and introducing optimized atomic charges.[121, 335] By combining this improved SCC-DFTB scheme with PTMD simulations, global optimization of the $(H_2O)_{1-10}NH_4^+$ and $(H_2O)_{1-10}NH_3$ clusters is then performed which allows to report a number of low-energy isomers for these species. Among them, a selected number of structures are further optimized at the MP2/Def2TZVP level of theory to confirm they are low-energy structures of the PES and to rationalize the difference in relative energy between both methods. A detailed description of the reported low-energy isomers is then provided as well as comparisons with the literature. The heat capacity curve of $(H_2O)_{20}NH_4^+$ is also obtained at the SCC-DFTB level and compared to previously published simulations. Some conclusions are finally presented. A very small part of this work has been published in 2019 in a review in *Molecular Simulation*.[384] A full paper devoted to this work is in preparation.

3.2.2 Results and Discussion

3.2.2.1 Dissociation Curves and SCC-DFTB Potential

In order to define the best SCC-DFTB parameter to model ammonia and ammonium water clusters, I have tested various sets of corrections. Each correction involves two modifications of the potential, the first one is the CM3 charge parameter D_{NH} and the second one is the multiplying factor, noted xNH, applied to the NH integrals in the Slater-Koster tables. So a given set is noted D_{NH}/xNH. Two sets of corrections have provided satisfactory results, 1.16/0.12 and 1.28/0.14. Figure 3.2 and 3.3 present dissociation curves obtained at the MP2/Def2TZVP, MP2/Def2TZVP with BSSE correction, original SCC-DFTB, SCC-DFTB 1.28/0.14 and SCC-DFTB 1.16/0.12 levels of theory. These curves are obtained using the same set of geometries regardless of the method applied to calculate the binding energies. They are obtained from the MP2/Def2TZVP optimized structures in which the distance between the water and the ammonium/ammonia was shifted along the N–O vector, all other geometrical parameters being kept fixed.

From Figure 3.2, the five curves display the same trends with a minimum located at almost the same N—O distance. At the curve minimum, binding energies vary between -25.57 and -21,07 kcal.mol^{-1} at the original SCC-DFTB and SCC-DFTB 1.28/0.14 levels, respectively. The binding energy obtained at the SCC-DFTB 1.16/0.12 level is the closest to that

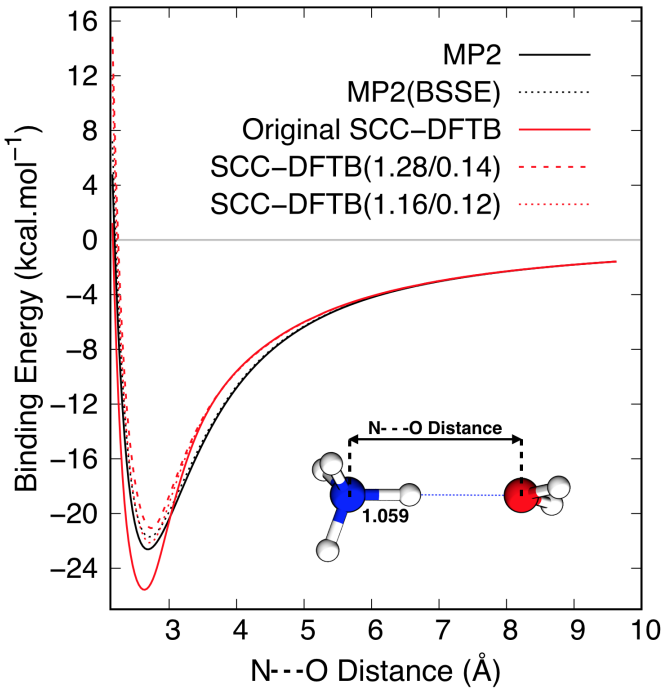

Figure 3.2: Binding energies of $(H_2O)NH_4^+$ as a function of the N—O distance at MP2/Def2TZVP (plain black), MP2/Def2TZVP with BSSE correction (dotted black), original SCC-DFTB (plain red), SCC-DFTB (1.28/0.14) (dotted red) and SCC-DFTB (1.16/0.12) (dashed red) levels of theory.

obtained at MP2/Def2TZVP level with BSSE correction with a binding energy difference of only 0.47 kcal.mol^{-1}. The SCC-DFTB 1.28/0.14 curve is also very close with a difference in binding energy only 0.16 kcal.mol^{-1} higher. It is worth mentioning that both sets of corrections lead to improved results as compared to the original SCC-DFTB parameters which leads to a too low binding energy as compared to MP2/Def2TZVP level with BSSE correction. Also the position of the minimum is more shifted at the original SCC-DFTB level (2.64 Å) than with corrections (2.73 Å). So from structural and energetic point of views, both sets of corrections are satisfactory.

From Figure 3.3, the five curves display significant differences. This effect is accentuated by smaller binding energy values: they vary from -3.82 to -7.39 kcal.mol^{-1} at the original SCC-DFTB and MP2/Def2TZVP levels, respectively, at the minimum of the curves. The binding energy obtained at the SCC-DFTB 1.16/0.12 level is the closest to that obtained at MP2/Def2TZVP level with BSSE correction with a binding energy difference of only 0.01 kcal.mol^{-1}. The SCC-DFTB 1.28/0.14 curve is also rather close with a difference in binding energy of only

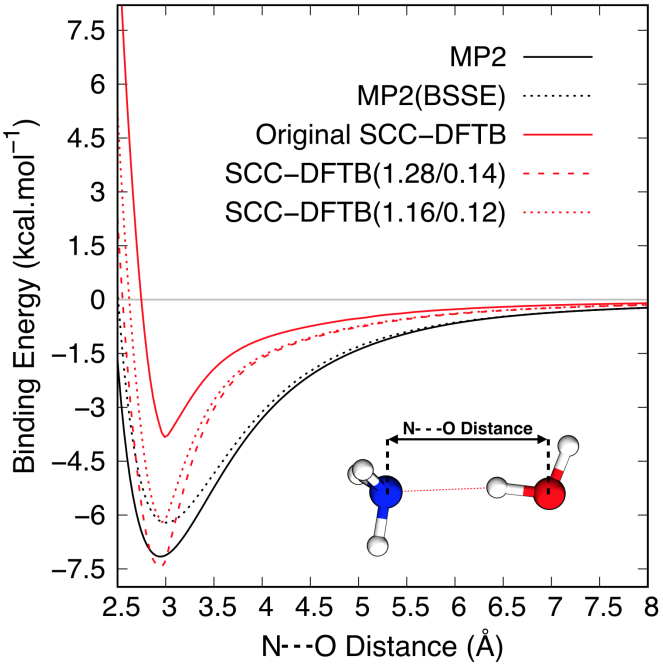

Figure 3.3: Binding energies of $(H_2O)NH_3$ as a function of the N—O distance at MP2/Def2TZVP (plain black), MP2/Def2TZVP with BSSE correction (dotted black), original SCC-DFTB (plain red), SCC-DFTB (1.28/0.14) (dotted red) and SCC-DFTB (1.16/0.12) (dashed red) levels of theory.

1.3 kcal.mol^{-1} higher. Here also, both sets of corrections lead to improved results as compared to the original SCC-DFTB parameters. The position of the minimum is also well reproduced by the corrected potentials. In contrast to $(H_2O)NH_4^+$, the shape of the curves for $(H_2O)NH_3$ obtained at the SCC-DFTB level differs significantly from those obtained at MP2 level. Vibrational frequencies calculated at the SCC-DFTB level for this systems are therefore expected to be inacurate. It is worth mentioning that the large difference in binding energy between $(H_2O)NH_4^+$ and $(H_2O)NH_3$ was expected owing to a stronger electrostatic contribution of NH_4^+ to the binding energy.

Another very important point when comparing the original SCC-DFTB potential and the corrected potentials, is the structure obtained for the $(H_2O)NH_4^+$ dimer. Figure 3.4 compares the structure obtained from geometry optimization at the SCC-DFTB 1.28/0.14 and original SCC-DFTB levels. The N-H covalent bond involved in the hydrogen bond is longer with the original potential while the N—O distance is smaller by 0.14 Å. This is reminiscent of the too low proton affinity of NH_4^+ predicted by the original SCC-DFTB potential. This discrepancy has been previously highlighted in other studies,[334, 386] and makes this potential unusable

in any realistic molecular dynamics simulation as it leads to a spurious deprotonation. Both sets of corrections are free of this error.

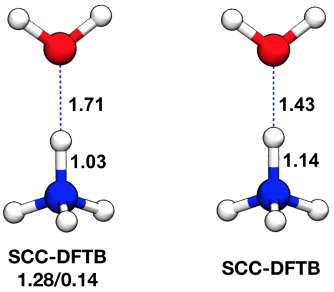

Figure 3.4: Structure of $(H_2O)NH_4^+$ obtained from geometry optimization at the SCC-DFTB 1.28/0.14 (right) and original SCC-DFTB (left) levels.

Figures 3.2 and 3.3 show that SCC-DFTB 1.16/0.12 better describe both $(H_2O)NH_3$ and $(H_2O)NH_4^+$ dissociation curves. Furthermore, as $(H_2O)NH_3$ is characterized by a much lower binding energy than $(H_2O)NH_4^+$, an error of the order of $\sim$1.0 kcal.mol^{-1} is more likely to play a significant role for ammonia than ammonium containing species. All the following discussion therefore involve the SCC-DFTB 1.16/0.12 potential.

3.2.2.2 Small Species: $(H_2O)_{1-3}NH_4^+$ and $(H_2O)_{1-3}NH_3$

As a first test case for the application of the SCC-DFTB 1.28/0.14 potential is the study of small ammonium and ammonia water clusters: $(H_2O)_{1-3}NH_4^+$ and $(H_2O)_{1-3}NH_3$. Due to the limited number of low-energy isomers for these species, we only consider the lowest-energy isomer of $(H_2O)_{1-2}NH_4^+$ and $(H_2O)_{1-3}NH_3$ and the two lowest-energy isomers for $(H_2O)_3NH_4^+$. As displayed in Figure 3.5 and 3.6, the reported low-energy isomers 1-a, 1′-a, 2-a, 2′-a, 3-a, 3-b, and 3′ display structures very similar to those obtained at the MP2/Def2TZVP level (1-a*, 1′-a*, 2-a*, 2′-a*, 3-a*, 3-b* and 3′-a*). Indeed, although differences in bond lengths are observed, they are rather small. In terms of energetics,

From an energetic point of view, it is interesting to first look at the relative energy between the two reported isomers of $(H_2O)_3NH_4^+$. Isomer 3-b is 2.12 kcal·mol^{-1} higher than 3-a at the SCC-DFTB level. At the MP2/Def2TZVP level, 3-b is 0.30 kcal·mol^{-1} lower than 3-a when ZPVE is not considered while it is 1.21 kcal·mol^{-1} higher when it is considered. In comparison, in the experimental results by H. Chang and co-workers, 3-a is more stable than 3-b.[367, 369] The authors also complemented their measurements by theoretical calculations which show

that at the B3LYP/6-31+G(d) level, 3-a is higher than 3-b. In contrast, at the MP2/6-31+G(d) level corrected with ZPVE, the energy of 3-a is lower than that of 3-b while it is inverted if ZPVE is taken into account.[367, 369] Additionally, F. Spiegelman and co-workers, conducted a global Monte Carlo optimizations with an intermolecular polarizable potential that lead to 3-a as lowest-energy isomer.[371] All these results show that for the specific question of lowest-energy isomer of $(H_2O)_3NH_4^+$, SCC-DFTB has an accuracy close to other *ab initio* methods which confirms its applicability.

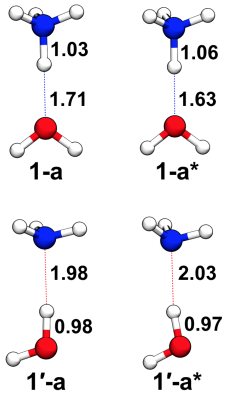

Figure 3.5: Structure of 1-a and 1′-a isomers obtained at the SCC-DFTB level and corresponding structures obtained at MP2/Def2TZVP level (1-a* and 1′-a* isomers). Selected bond lengths are in Å.

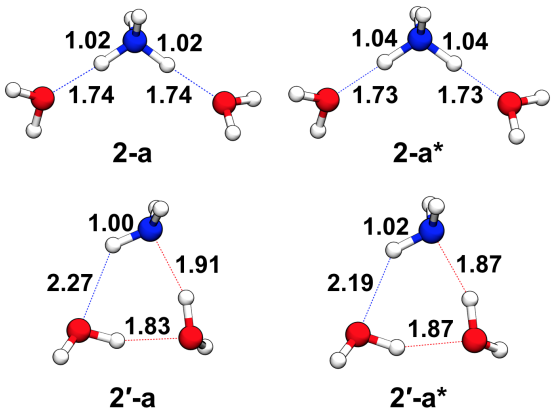

Figure 3.6: Structure of 2-a and 2′-a isomers obtained at the SCC-DFTB level and corresponding structures obtained at MP2/Def2TZVP level (2-a*, 2′-a* isomers). Selected bond lengths are in Å.

As listed in Table 3.1, the relative binding energies $\Delta E_{bind.}^{whole}$ or $\Delta E_{bind.}^{sep.}$ of $(H_2O)NH_4^+$ and $(H_2O)NH_3$ are 1.21 and -1.17 kcal·mol^{-1}, respectively, which again highlights that SCC-

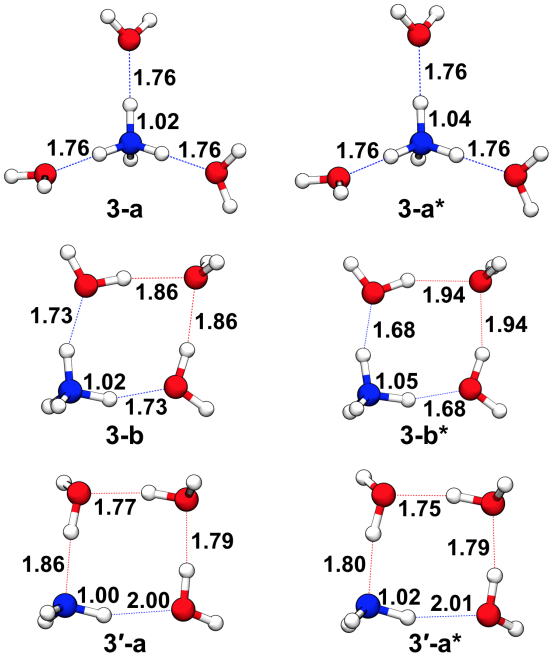

Figure 3.7: Structure of 3-a, 3-b and 3′-a isomers obtained at the SCC-DFTB level and corresponding structures obtained at MP2/Def2TZVP level (3-a*, 3-b* and 3′-a* isomers). Selected bond lengths are in Å.

DFTB is in agreement with MP2/Def2TZVP. For $(H_2O)NH_3$, the negative value shows that MP2/Def2TZVP binding energy is smaller than the SCC-DFTB value. This is inverse to what is shown in Figure 3.3 and results from structural reorganization after optimization. All other values of Table 3.1 are equal or smaller than these values, whether considering $\Delta E_{bind.}^{whole}$ or $\Delta E_{bind.}^{sep.}$, which again demonstrates that the presently proposed SCC-DFTB potential provides results in line with reference MP2/Def2TZVP calculations.

$(H_2O)_{4-10}NH_4^+$ clusters have been studied by molecular dynamic and Monte Carlo simulations in combination with DFT and MP2 approaches although these latter are computationally expensive.[340, 367, 369, 371, 372, 387] In contrast, to the best of our knowledge, no theoretical calculation about $(H_2O)_{5-10}NH_3$ clusters have been conducted. The low computational cost of SCC-DFTB and its seemingly good performances on small clusters provide an appealing opportunity to thoroughly explore the PES of both large ammonium and ammonia containing water clusters. In the following section, the five lowest-energy isomers of clusters $(H_2O)_{4-10}NH_4^+$ and $(H_2O)_{4-10}NH_3$ are presented and discussed in details.

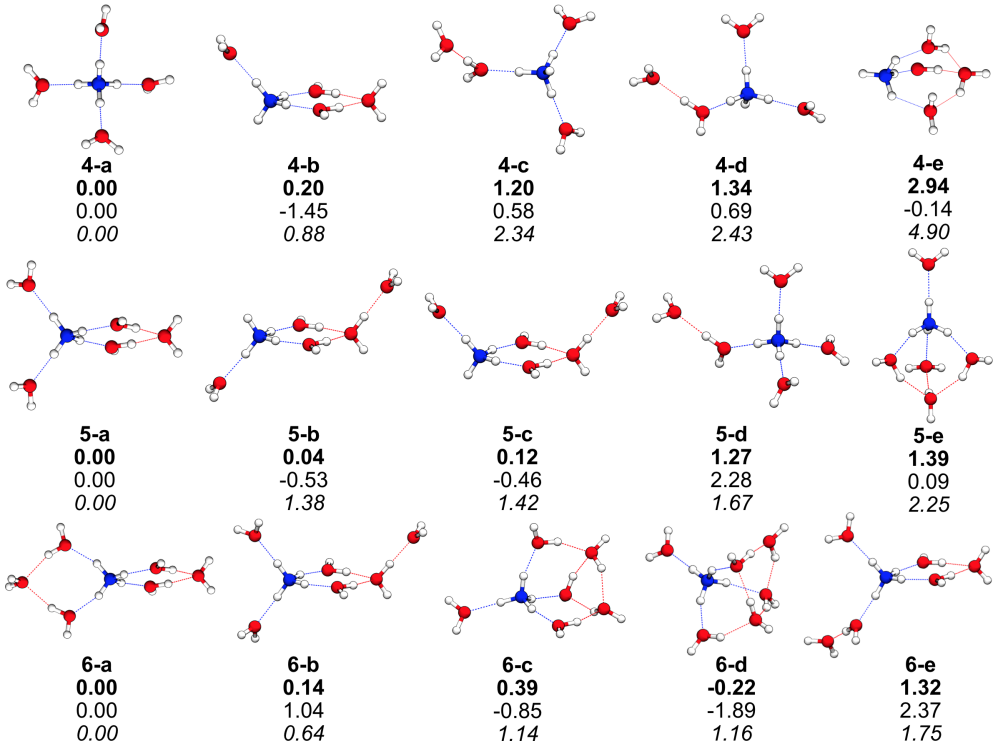

Figure 3.8: Five lowest-energy isomers of $(H_2O)_{4-6}NH_4^+$ and corresponding relative energies at MP2/Def2TZVP level with (bold) and without ZPVE (roman) correction and SCC-DFTB level (italic). Relative energies are given in kcal·mol^{-1}.

Cluster $(H_2O)_5NH_4^+$. For cluster $(H_2O)_5NH_4^+$, the five low-energy isomers are illustrated in Figure 3.8. The isomer 5-a is the most stable one, which is consistent with F. Spiegelman's result using the global Monte Carlo optimization and G. Shields's results obtained with a mixed molecular dynamics/quantum mechanics moldel.[371, 372] The energy order of 5-a to 5-e at SCC-DFTB level is consistent with that at MP2/Def2TZVP level with ZPVE correction. 5-a, 5-d and 5-e have a complete solvation shell while one dangling N-H bond is exposed in 5-b and 5-c. For the five low-energy isomers, the energy order of our results are not exactly the same with H. Chang's calculation results at MP2/6-31+G(d)level with ZPVE correction.[369] In H. Chang's results, 5-d is the low-energy isomer and 5-a is the second low-energy isomer. They didn't find isomers 5-b and 5-c. From the comparison, it implies the combination of SCC-DFTB and PTMD is good enough to find the low-energy isomer and the basis set can affect the energy order when using the MP2 approach.

When all the water molecules are considered as a whole part, the obtained binding energy

has a deviation due to the interaction of water molecules. As listed in Table 3.2, for isomers 5-a to 5-e, the relative binding energy $\Delta E_{bind.}^{whole}$ are -1.62, 0.72, 0.69, -1.08 and -2.08 kcal·mol^{-1} and $\Delta E_{bind.}^{sep.}$ are -0.56, 0.48, 0.55, -0.78 and 0.88 kcal·mol^{-1}, respectively. The $\Delta E_{bind.}^{whole}$ is bigger than corresponding $\Delta E_{bind.}^{sep.}$, which indicates it is better to calculate the binding energy with considering the water molecules separately. The $\Delta E_{bind.}^{sep.}$ is less than 1.00 kcal·mol^{-1} for the five low-energy isomers of cluster $(H_2O)_5NH_4^+$, so the SCC-DFTB method is good enough compared to MP2/Def2TZVP with BSSE correction for cluster $(H_2O)_5NH_4^+$.

Cluster $(H_2O)_6NH_4^+$. For cluster $(H_2O)_6NH_4^+$, no N-H bond is exposed in the five low-energy isomers displayed in Figure 3.8. 6-a is the first low-energy isomer at SCC-DFTB level, which is a symmetric double-ring species connected together by eight hydrogen bonds making it a robust structure. 6-a is also the first low-energy isomer obtained using the Monte Carlo optimizations with the intermolecular polarizable potential.[371] 6-d is the first low-energy isomer at MP2/Def2TZVP level with ZPVE correction but it is only 0.22 kcal·mol^{-1} lower than 6-a. In Shields's results, 6-d is also the first low-energy isomer at MP2/aug-cc-pVDZ level.[372] In H. Chang's study, 6-b with a three-coordinated H_2O molecule is the first low-energy isomer for cluster $(H_2O)_6NH_4^+$ at B3LYP/6-31+G(d) level.[367] 6-b is also the first low-energy isomer at B3LYP/6-31++G(d,p) level including the harmonic ZPVE contribution.[371] The energy of 6-b is only 0.14 kcal·mol^{-1} higher than that of 6-a at MP2/Def2TZVP level with ZPVE correction. The energies of 6-a, 6-b and 6-d are very close at both MP2/Def2TZVP with ZPVE correction and SCC-DFTB levels, which implies it is easy to have a transformation among 6-a, 6-b and 6-d. It shows SCC-DFTB is good to find the low-energy isomers of cluster $(H_2O)_6NH_4^+$ compared to MP2 and B3LYP methods.

As shown in Table 3.2, for isomers 6-a to 6-e, the relative binding energy $\Delta E_{bind.}^{whole}$ are -1.71, -1.14, -2.06, -2.90 and -1.18 kcal·mol^{-1} and the $\Delta E_{bind.}^{sep.}$ are -0.38, -0.76, 0.27, -1.06 and -0.60 kcal·mol^{-1}, respectively. It indicates the binding energies are very close at SCC-DFTB and MP2/Def2TZVP with BSSE correction levels when water molecules are calculated separately. The $\Delta E_{bind.}^{whole}$ is bigger than corresponding $\Delta E_{bind.}^{sep.}$ because of the interaction of water molecules when all the water molecules are considered as a whole part.

Cluster $(H_2O)_7NH_4^+$. For cluster $(H_2O)_7NH_4^+$, the five low-energy isomers are shown in Figure 3.9. The ion core NH_4^+ has a complete solvation shell in isomers 7-a to 7-e. 7-a and 7-b with three three-coordinated H_2O molecules are the first low-energy isomers at SCC-DFTB level. In F. Spiegelman's study, 7-a is also the first low-energy isomer using the Monte Carlo optimizations with the intermolecular polarizable potential.[371] 7-c is the

first low-energy isomer at MP2/Def2TZVP with ZPVE correction level including three three-coordinated water molecules. 7-c is also the first low-energy isomer at B3LYP/6-31++G(d,p) level including the harmonic ZPVE contribution.[371] 7-e is the first low-energy isomer with three three-coordinated H_2O molecules at MP2/aug-cc-pVDZ level in G. Shields's study.[372] As illustrated in Figure 3.9, the energy difference between 7-a, 7-c and 7-e at MP2/Def2TZVP with ZPVE correction and SCC-DFTB levels are less than 0.61 kcal·mol^{-1} so it is possible that the first low-energy isomer is different when different method are applied. The energy of 7-a and 7-b are the same at both MP2/Def2TZVP with ZPVE correction and SCC-DFTB levels and their structures are similar, which indicates it is easy for them to transform to each other. The results for cluster $(H_2O)_7NH_4^+$ verify the accuracy of SCC-DFTB approach.

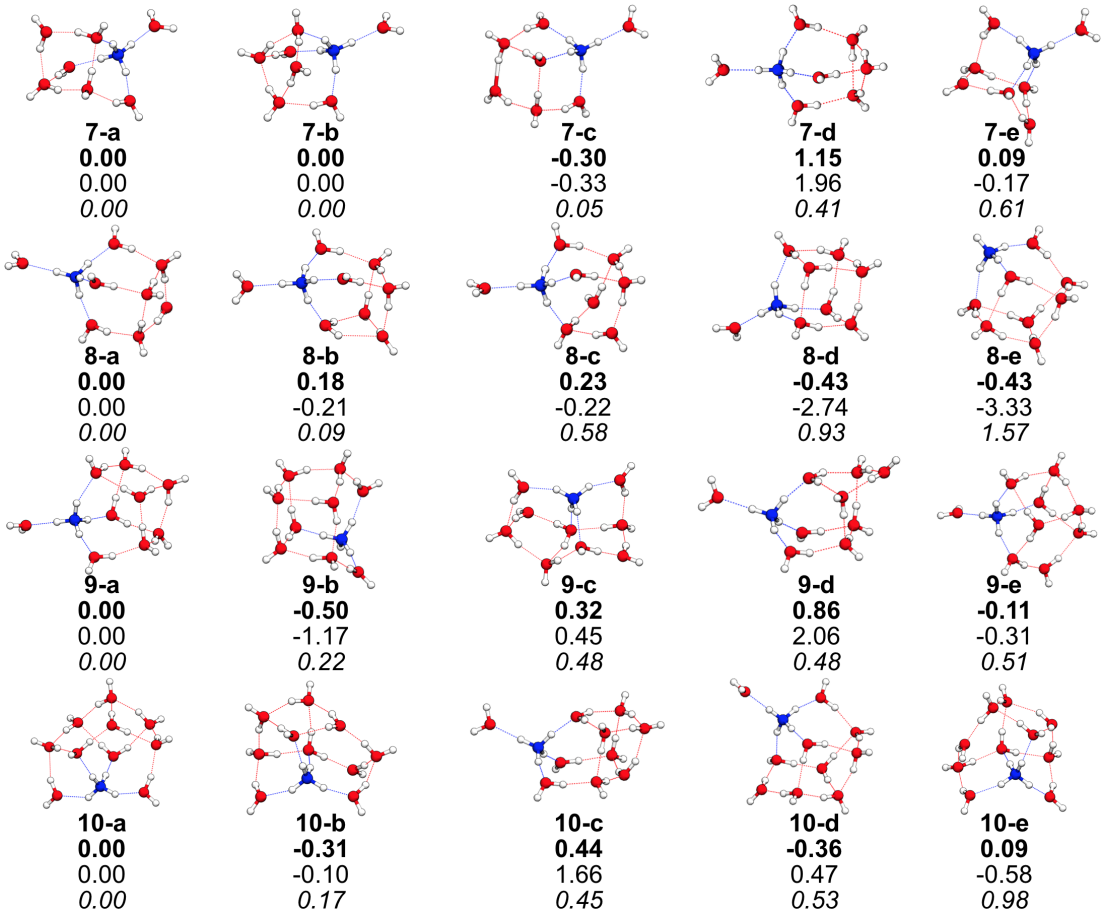

Figure 3.9: The five low-energy isomers of clusters $(H_2O)_{7-10}NH_4^+$ and the associated relative energies (in kcal·mol^{-1}) at MP2/Def2TZVP level with (bold) and without ZPVE correction and SCC-DFTB level (italic).

As shown in Table 3.2, for isomers 7-a to 7-e, the relative binding energy $\Delta E_{bind.}^{whole}$ are -2.95, -2.92, -2.17, -1.28 and -3.22 kcal·mol^{-1} and the $\Delta E_{bind.}^{sep.}$ are only -0.39, -0.38, 0.09, -1.35 and -2.27 kcal·mol^{-1}, respectively. It indicates the binding energies of 7-a to 7-e at SCC-DFTB agree well especially for 7-a to 7-d with those at MP2/Def2TZVP with BSSE correction level when water molecules are calculated separately. When all the water molecules are regarded as a whole part, the results of SCC-DFTB are not as good as those of the MP2 with BSSE method.

Cluster $(H_2O)_8NH_4^+$. For cluster $(H_2O)_8NH_4^+$, 8-a to 8-e are the five low-energy isomers displayed in Figure 3.9. In 8-a to 8-d, the ion core NH_4^+ has a complete solvation shell. 8-a is the first low-energy isomer in our calculation at SCC-DFTB level. In F. Spiegelman's study, 8-b is the first low-energy isomer at B3LYP/6-31++G(d,p) level including the harmonic ZPVE contribution.[371] The structures of 8-a and 8-b are very similar and the energy differences are only 0.18 and 0.09 kcal·mol^{-1} at MP2/Def2TZVP with ZPVE correction and SCC-DFTB levels, respectively. 8-d with seven three-coordinated H_2O molecules in the cube frame is the first low-energy isomer in our calculation at MP2/Def2TZVP with ZPVE correction level, which is consistent with F. Spiegelman's results obtained using Monte Carlo optimizations.[371] In 8-e, NH_4^+ has an exposed N-H bond and it also has seven three-coordinated H_2O molecules in its cage frame. The energies of isomers 8-a to 8-e are very close calculated using SCC-DFTB and MP2 methods, so it's possible that the energy order will change when different methods or basis sets are applied. The results certificate the SCC-DFTB is good enough to find the low-energy isomers for cluster $(H_2O)_8NH_4^+$.

As shown in Table 3.2, for isomers 8-a to 8-e, the relative binding energy $\Delta E_{bind.}^{whole}$ are -2.20, -1.61, -3.71, -2.43 and -0.55 kcal·mol^{-1}, respectively and the biggest $\Delta E_{bind.}^{sep.}$ is -2.01 kcal·mol^{-1}. It shows the binding energies at SCC-DFTB level agree well with those at MP2/Def2TZVP with BSSE correction level when water molecules are calculated separately. From these results, when all the water molecules are considered as a whole part, the results of SCC-DFTB didn't agree well with those of the MP2 with BSSE correction method.

Cluster $(H_2O)_9NH_4^+$. For cluster $(H_2O)_9NH_4^+$, the five low-energy structures of $(H_2O)_9NH_4^+$ are illustrated in Figure 3.9. 9-a with seven three-coordinated H_2O molecules in the cage frame is the first low-energy isomer at SCC-DFTB level. 9-a is also the first low-energy structure at B3LYP/6-31++G(d,p) level including the harmonic ZPVE contribution in F. Spiegelman's study.[371] 9-b with one N-H bond exposed in NH_4^+ is the second low-energy isomer whose energy is only 0.22 kcal·mol^{-1} higher than that of 9-a in the results of SCC-DFTB calculation.

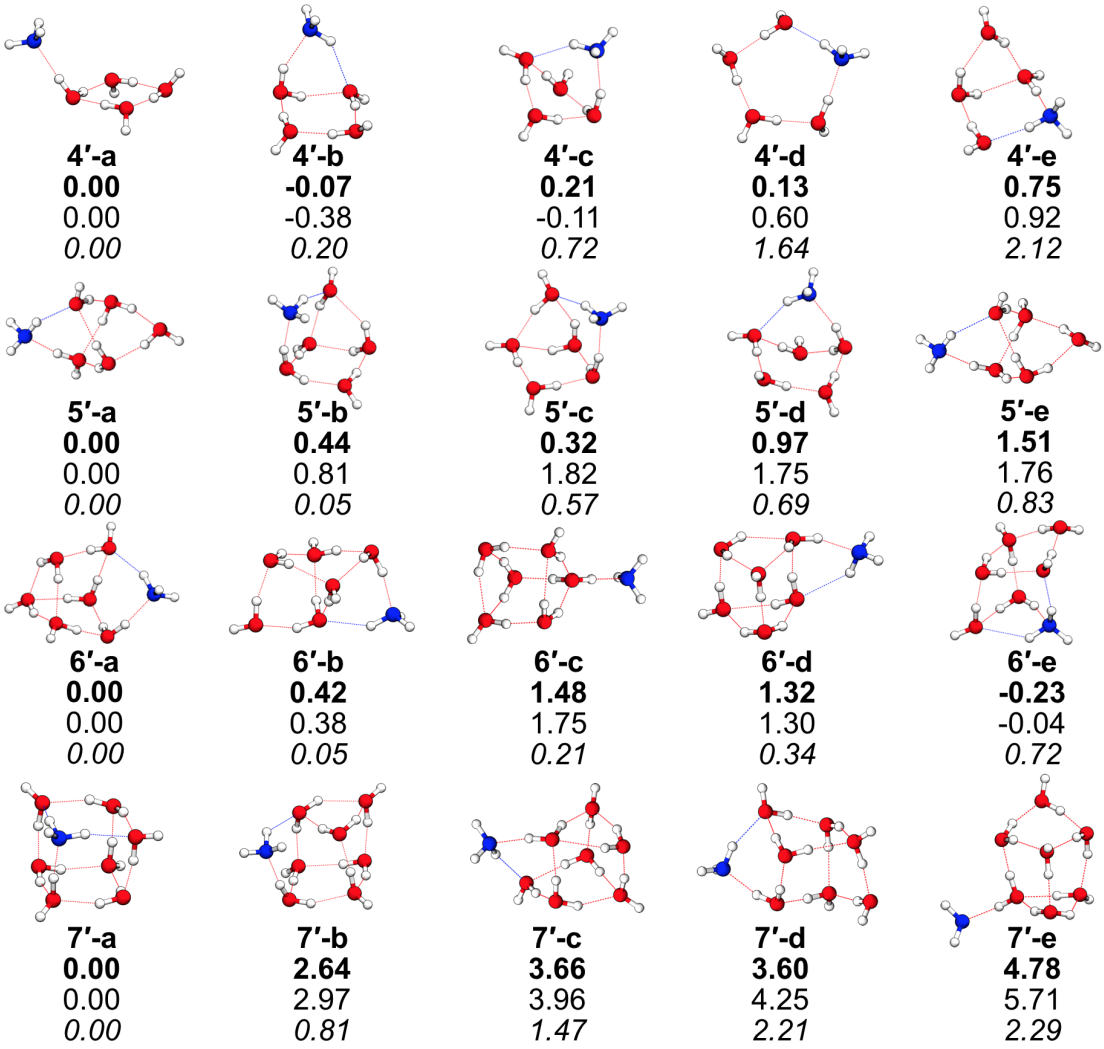

Figure 3.10: The five low-energy isomers of cluster $(H_2O)_{4-7}NH_3$ and the associated relative energies (in kcal·mol^{-1}) at MP2/Def2TZVP level with (bold) and without ZPVE correction and SCC-DFTB level (italic).

are the second and third isomers at SCC-DFTB level and they are the third and second isomers at MP2/Def2TZVP level with ZPVE. The energy difference between 5′-b and 5′-c is only 0.44 and 0.05 kcal·mol^{-1} at MP2/Def2TZVP with ZPVE correction level and SCC-DFTB level, respectively. In addition, the structures of 5′-b and 5′-c are very similar so it is possible for them to transform to each other. 5′-d with two three-coordinated water molecules is the fourth low-energy structure at both MP2/Def2TZVP with ZPVE correction and SCC-DFTB levels. 5′-e with four three-coordinated water molecules is the fifth low-energy structure at

both MP2/Def2TZVP with ZPVE correction and SCC-DFTB levels. The frames of 5′-a and 5′-e are almost the same but the water molecule who offers the hydrogen or oxygen to form the O-H···O hydrogen bonds has a small difference. The energy of 5′-e is 1.51 kcal·mol^{-1} higher than that of 5′-a at MP2/Def2TZVP with ZPVE correction level, which implies the intermolecular connection mode has an influence on the stability of the isomers. The results show the SCC-DFTB approach performs well to find the low-energy isomers for cluster $(H_2O)_5NH_3$ compared with MP2/Def2TZVP with ZPVE correction method.

The relative binding energies of isomers 5′-a to 5′-e are shown in Table 3.2. The values of $\Delta E_{bind.}^{whole}$ are less than 0.82 kcal·mol^{-1} for 5′-a to 5′-e. The values of $\Delta E_{bind.}^{sep.}$ are bigger than the corresponding values of $\Delta E_{bind.}^{whole}$. It indicates SCC-DFTB agrees better with MP2/Def2TZVP $\Delta E_{bind.}^{whole}$ when all the water molecules are regarded as a whole part than considering separately for calculating the binding energy of cluster $(H_2O)_5NH_3$.

Cluster $(H_2O)_6NH_3$. For cluster $(H_2O)_6NH_3$, the five low-energy structures 6′-a to 6′-e are displayed in Figure 3.10. 6′-a is the first low-energy structure at SCC-DFTB level. All water molecules in 6′-a are three-coordinated. 6′-b is the second low-energy isomer at SCC-DFTB level and it's only 0.42 and 0.05 kcal·mol^{-1} higher than the ones of 6′-a at MP2/Def2TZVP with ZPVE correction level and SCC-DFTB level, respectively. 6′-c to 6′-d are the third and fourth low-energy isomers in which the six water molecules form a triangular prism structure and there are one and two four-coordinated water molecules in 6′-c to 6′-d, respectively. 6′-e is the fifth low-energy structure at SCC-DFTB level but it's the first low-energy isomer at MP2/Def2TZVP with ZPVE correction level. The energy of 6′-a to 6′-e are very close at both both MP2/Def2TZVP with ZPVE correction and SCC-DFTB levels that it is difficult to keep the energy order when different methods or basis sets are applied. This also shows the SCC-DFTB method used is efficient to find the low-energy isomers of cluster $(H_2O)_6NH_3$.

The relative binding energies of isomers 6′-a to 6′-e are listed in Table 3.2. The smallest and the biggest values of $\Delta E_{bind.}^{whole}$ are -0.05 and -1.11 kcal·mol^{-1}, respectively. The smallest absolute value of $\Delta E_{bind.}^{sep.}$ is 1.96 kcal·mol^{-1}. The binding energies calculated with SCC-DFTB agree well with those calculated at MP2/Def2TZVP level for cluster $(H_2O)_6NH_3$ when all the water molecules are considered as a whole part.

Cluster $(H_2O)_7NH_3$. For cluster $(H_2O)_7NH_3$, the five low-energy isomers 7′-a to 7′-e are illustrated in Figure 3.10. 7′-a with a cubic structure is the first lowest energy structure at both MP2/Def2TZVP with ZPVE correction and SCC-DFTB levels. 7′-b is the second low-energy structure at both MP2/Def2TZVP with ZPVE correction and SCC-DFTB levels. 7′-b

has a similar structure with 7′-a but the NH_3 in it has two exposed N-H bonds. 7′-c and 7′-d have similar structures and they are the third and fourth lowest energy isomers at SCC-DFTB level and their energy difference is only 0.74 kcal·mol^{-1}. 7′-e with three exposed N-H bonds is the fifth low-energy isomer at both MP2/Def2TZVP with ZPVE correction and SCC-DFTB levels. The results of SCC-DFTB method agree well with those of MP2/Def2TZVP with ZPVE correction for the five low-energy isomers of cluster $(H_2O)_7NH_3$.

The smallest and the biggest values of $\Delta E_{bind.}^{whole}$ of isomers 7′-a to 7′-e are -0.02 and -1.11 kcal·mol^{-1}, respectively and the smallest absolute value of $\Delta E_{bind.}^{sep.}$ is 2.02 kcal·mol^{-1} shown in Table 3.2. The binding energies calculated with SCC-DFTB agree well with those obtained using MP2/Def2TZVP for cluster $(H_2O)_7NH_3$ when all the water molecules are considered as a whole part.

Cluster $(H_2O)_8NH_3$. For cluster $(H_2O)_8NH_3$, 8′-a to 8′-e are the five low-energy structures shown in Figure 3.11. 8′-a in which eight water molecules constitute a cube is the first lowest energy structure in SCC-DFTB calculation results. 8′-b also with a water-cube structure is the second low-energy structure at SCC-DFTB level and it is the first low-energy isomer at MP2/Def2TZVP with ZPVE correction level. The energy differences between 8′-a and 8′-b are only 0.30 and 0.93 kcal·mol^{-1} at MP2/Def2TZVP with ZPVE correction level and SCC-DFTB level. From Figure 3.11, the fifth low-energy isomer 8′-e includes less hydrogen bonds than other isomers and its energy has a clearly increase compared to other isomers. The results show the SCC-DFTB method performs well to obtain the low-energy isomers of cluster $(H_2O)_8NH_3$.

The smallest and the biggest values of $\Delta E_{bind.}^{whole}$ of isomers 8′-a to 8′-e are -0.1 and -1.28 kcal·mol^{-1}, respectively while the smallest absolute value of $\Delta E_{bind.}^{sep.}$ is 3.04 kcal·mol^{-1} shown in Table 3.2. The binding energies calculated with SCC-DFTB agree better with those obtained at MP2/Def2TZVP level when all the water molecules are considered as a whole part in cluster $(H_2O)_8NH_3$ than the ones when water molecules calculated separately.

Cluster $(H_2O)_9NH_3$. For cluster $(H_2O)_9NH_3$, 9′-a to 9′-e are the five lowest energy structures displayed in Figure 3.11. 9′-a with a "chair" structure is the first low-energy structure at SCC-DFTB level. 9′-b, 9′-c and 9′-d in which the nine water molecules have the similar configuration are the second, third and fourth isomers. In 9′-b and 9′-c, the NH_3 has three exposed N-H bonds and the energies of 9′-b and 9-c are very close at both MP2/Def2TZVP with ZPVE correction and SCC-DFTB levels. The NH_3 has two exposed N-H bonds in 9′-d. 9′-e is the fifth low-energy isomer in the SCC-DFTB calculation results but it is the first low-energy isomer in the calculation results of MP2/Def2TZVP with ZPVE correction. 9′-e has a

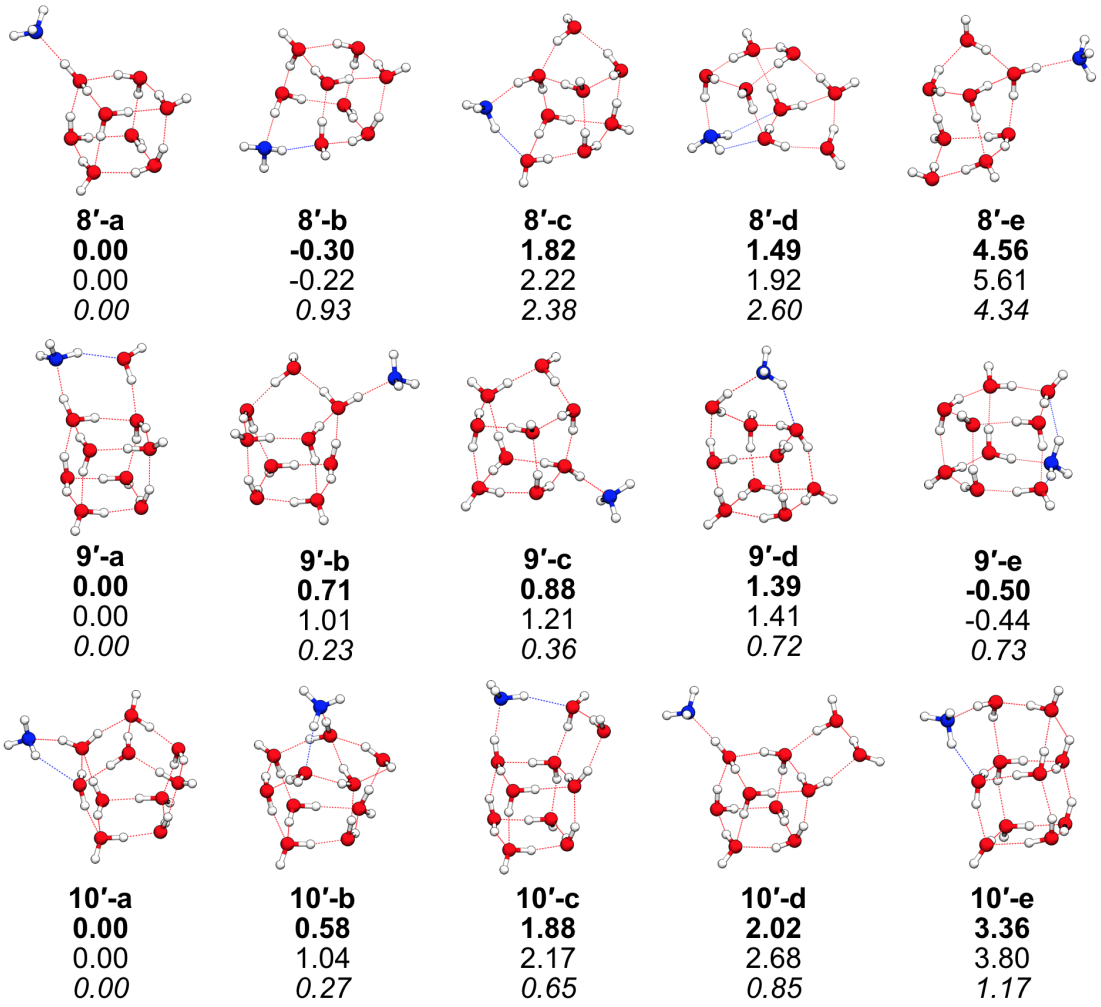

Figure 3.11: The five low-energy isomers of clusters $(H_2O)_{8-10}NH_3$ and the associated relative energies (in kcal·mol^{-1}) at MP2/Def2TZVP level with (bold) and without ZPVE correction and SCC-DFTB level (italic).

pentagonal prism structure and all the water molecules in it are three-coordinated. The relative energy for each isomer between SCC-DFTB level and MP2/Def2TZVP with ZPVE correction level is less than 1.23 kcal·mol^{-1}. This shows our SCC-DFTB calculation results are consistent with the calculation results of MP2/Def2TZVP with ZPVE correction for low-energy isomers optimization of cluster $(H_2O)_9NH_3$.

The relative binding energies of isomers 9′-a to 9′-e are shown in Table 3.2. The absolute values of $\Delta E_{bind.}^{whole}$ are less than 1.09 kcal·mol^{-1} while the smallest absolute value of $\Delta E_{bind.}^{sep.}$ is 2.57 kcal·mol^{-1}. The binding energies calculated with SCC-DFTB agree well with those

acquired at MP2/Def2TZVP level when all the water molecules are considered as a whole part for cluster $(H_2O)_9NH_3$.

Cluster $(H_2O)_{10}NH_3$. For cluster $(H_2O)_{10}NH_3$, 10′-a to 10′-e are the five low-energy structures illustrated in Figure 3.11. The energy order for the five low-energy structures is the same at SCC-DFTB level and MP2/Def2TZVP with ZPVE correction level. 10′-a and 10′-b are the first and second low-energy isomer in which the ten water molecules constitute the pentagonal prism. The energy differences of 10′-a and 10′-b are only 0.58 and 0.27 kcal·mol^{-1} at MP2/Def2TZVP with ZPVE correction and SCC-DFTB levels. 10′-c and 10′-d are the third and fourth low-energy isomers in which eight water molecules constitute a cube and the energy differences between 10′-c and 10′-d are very small calculated with SCC-DFTB or MP2/Def2TZVP with ZPVE correction. 10′-e is the fifth low-energy structure in which eight water molecules also constitute a cube but its energy is obviously higher than those of 10′-c and 10′-d. The calculation results of SCC-DFTB are consistent with those of MP2/Def2TZ for the optimization of the low-energy isomers of cluster $(H_2O)_{10}NH_3$. According to the structures of the five low-energy isomers of clusters $(H_2O)_{1-10}NH_3$, in most cases, the NH_3 usually contains two or three exposed N-H bonds.

The smallest and biggest values of $\Delta E_{bind.}^{whole}$ of isomers 10′-a to 10′-e are -0.03 and -1.10 kcal·mol^{-1} while the smallest absolute value of $\Delta E_{bind.}^{sep.}$ is 4.80 kcal·mol^{-1} shown in Table 3.2. The values of $\Delta E_{bind.}^{whole}$ implies that SCC-DFTB agree very well with MP2/Def2TZVP for cluster $(H_2O)_{10}NH_3$ when all the water molecules are regarded as a whole part.

3.2.2.5 Properties of $(H_2O)_{20}NH_4^+$ Cluster

The lowest-energy isomer of $(H_2O)_{20}NH_4^+$ was previously reported by Douady *et al.*[340, 371] as well as by other studies.[389, 390] Douady *et al.* conducted a Monte Carlo simulation in combination with the Kozack-Jordan polarizable potential.[379, 391] This isomer displays a closed-shell structure, similar to the well-know structure of $(H_2O)_{21}H^+$, with the NH_4^+ ion fully solvated at the center of the aggregate. The structure of $(H_2O)_{20}NH_4^+$ is depicted in Figure 3.12. Starting from the coordinates Douady *et al.* kindly sent to us, our PTMD exploration of the PES does not lead any lower-energy isomer. We thus consider this isomer to be also the lowest-energy isomer at the SCC-DFTB level.

Douady *et al.* further computed the heat capacity of $(H_2O)_{20}NH_4^+$ as a function of the temperature.[340] In order to further demonstrate the accuracy of SCC-DFTB we have conducted a similar calculation. The modelling of heat capacity as a function of the temperature

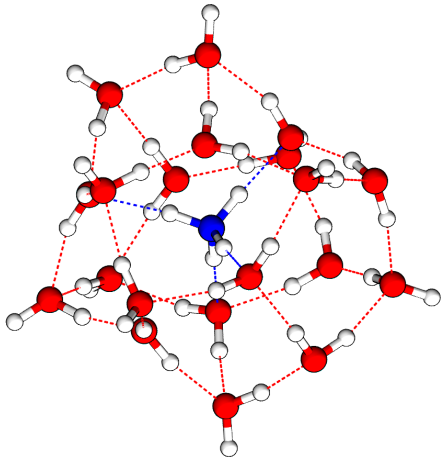

Figure 3.12: Lowest-energy isomer of $(H_2O)_{20}NH_4^+$.

can be achieved in different ways. The simplest one consists in performing MC or MD simulations at different temperatures and extracting for each one the heat capacity from a direct calculation of the variance of the potential energy. This approach is somewhat statistically inefficient and thus alternative approaches have been proposed. Indeed, to reduce the statistical noise and to extrapolate heat capacities at temperatures not explicitly simulated, one can benefit from the fact that in MD or MC simulations a given configuration may be visited at different temperatures. Labastie and Whetten,[392] proposed a method to take advantage of these overlaps to calculate heat capacity curves. It is referred to as the multiple histogram method. It uses probability densities, extracted from a 10 ns PTMD simulation, of finding an energy at a given temperature leading to a set of histograms for each simulated temperature. The entropy and partition functions are extracted from these histograms which can then give access to internal energy at any given temperature. The heat capacity at temperature T is finally calculated as:

$$C(T) = \frac{N_{dof} k_B}{2} + \frac{\langle V^2 \rangle - \langle V \rangle^2}{k_B T^2} \tag{3.1}$$

where k_B is the Boltzmann constant, N_{dof} the number of degrees of freedom, $\langle V \rangle$ and $\langle V^2 \rangle$ the internal energy and square of internal energy at temperature T, respectively. The first term of equation 3.1 is the classical limit of the heat capacity at T = 0 K. Figure 3.13 displays the heat capacity curve we obtained. It is very similar to the one obtained by Douady and co-workers. It is flat up to ∼150 K with a sharp increase starting at ∼165 K. This behaviour also exits in $(H_2O)_{21}H^+$,[62, 340] and was interpreted by a weak density of low-energy isomers above the

global minimum, *i.e.* a particularly stable lowest-energy structure.[62] Douady*et al.* observed a slightly higher transition temperature of $(H_2O)_{20}NH_4^+$ as compared to $(H_2O)_{21}H^+$. This is also true at the SCC-DFTB level as the transition temperature of $(H_2O)_{21}H^+$ was evaluated at $\sim$140 K.[62] This confirms that SCC-DFTB with the improved set of N—H parameters, besides properly describing structures and binding energies, also lead to correct thermodynamical properties.

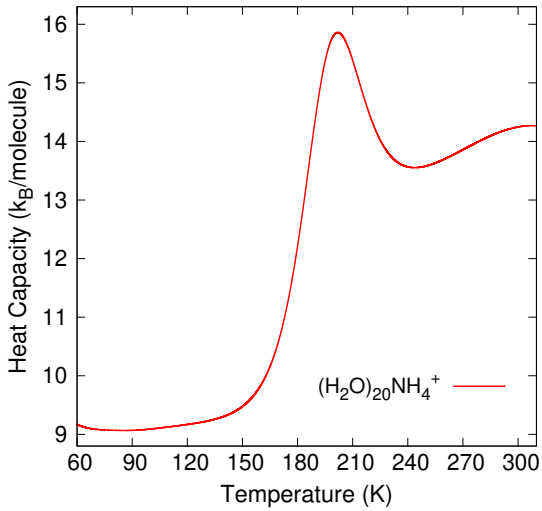

Figure 3.13: Canonical heat capacity as a function of the temperature of $(H_2O)_{20}NH_4^+$.

3.2.3 Conclusions for Ammonium/Ammonia Including Water Clusters

In this paper, we have introduced a modification to the N-H set of parameters by modifying both the original mio-set of N—H integrals and the evaluation of the charges. The proposed new set of parameters solve the spurious deprotonation observed for NH_4^+ using the original set of parameters. We first demonstrate that this new set of parameters leads also to improved description of the dissociation curves of both $(H_2O)NH_4^+$ and $(H_2O)NH_3$ dimers as compared to MP2/Def2TZVP method with BSSE correction reference calculations. By combining this new potential, SCC-DFTB (0.12/1.16), to PTMD simulations, a number of low-energy isomers are reported for $(H_2O)_{1-10}NH_4^+$ and $(H_2O)_{1-10}NH_3$ clusters. Further geometry optimizations at the MP2/Def2TZVP lead to structures very similar to those reported at the SCC-DFTB level and also reported in the literature. The SCC-DFTB binding energies also agree well with those calculated with the MP2/Def2TZVP approch including with BSSE correction. This demon-

strates that SCC-DFTB (0.12/1.16) approach is well suited to the description of ammonium and ammonia containing water clusters.

Among the five lowest-energy structures of $(H_2O)_4NH_4^+$, four of them display a dangling N-H bond. Among the five lowest-energy structures of $(H_2O)_5NH_4^+$, only two structures display a dangling N-H bond. Among the five lowest-energy isomers of $(H_2O)_{6-10}NH_4^+$, all the structures, except 8-e, display a ion core NH_4^+ that has a complete solvation shell but it is not located at the center of the water cluster. In the most stable structures of $(H_2O)_{20}NH_4^+$, reported in a previous study, the ion core NH_4^+ has a complete solvation shell and it is located in the center of the water cluster. $(H_2O)_{1-10}NH_3$ clusters display significantly different structures. Indeed, NH_3 is never fully solvated by the water molecules whatever the cluster size. It either participates to the surface hydrogen bond network in a few cases, or acts as a surface molecule, only bonded to the water molecules by a unique hydrogen bond.

Application of the presently proposed potential to the calculation of the heat capacity curve of $(H_2O)_4NH_4^+$ further demonstrates the quality of the potential as the SCC-DFTB curve is close to the previously reported curve. The present study therefore demonstrates the ability of SCC-DFTB to model small size ammonium and ammonia containing water clusters. Due to the low computational cost of SCC-DFTB as compared to *ab initio* methods, one can envisage its application to describe the larger size ammonium and ammonia containing water clusters. One can also envisage the study of water clusters containing a mixture of nitrogen and sulphur compounds, for instance, ammonium and sulfate ions. These species, their conjugated basis and acid in combination with dimethylamine and water molecules represent the basis for nucleation of atmospheric particles and SCC-DFTB could play a major in the theoretical description of these species.

3.3 Structural and Energetic Properties of Protonated Uracil Water Clusters

3.3.1 General Introduction

Gas phase investigations of molecules help to understand the intrinsic properties of molecules that are free from the effects of solvents. The gas phase study needs to be extended towards more realistic biomolecular systems, to reveal how the intrinsic molecular properties are affected by the surrounding medium when the biomolecules are in a natural environment.[147, 393, 394, 395] The hydration study of biomolecules is of paramount importance to get insights

The fragmentation cross sections obtained by N. Dalleska and coworkers [411] for protonated water clusters are within our error bars for $n = 5, 6$ and about a factor of 2 lower for $n = 3, 4$. However their cross section is notably lower for $(H_2O)_2H^+$ as compared to our measurement for $(H_2O)UH^+$. This difference may be explained by the fact that UH^+ forms a weaker bond with water than H_2OH^+ does. Indeed the dissociation energy $D[H_2OH^+–H_2O]$ is 1.35 eV [411, 414] whereas the value for $D[UH^+–H_2O]$ is estimated between 0.54 [396] and 0.73 eV. [404] The same behavior is observed for $n = 3$, and the dissociation energy $D[(H_2O)_2H^+–H_2O] = 0.86$ eV [411, 414] is greater than the dissociation energy $D[U(H_2O)H^+–H_2O] = 0.49$ eV.[396] Hence the dissociation of water molecules is more favored in the protonated uracil cluster than in the pure water clusters.

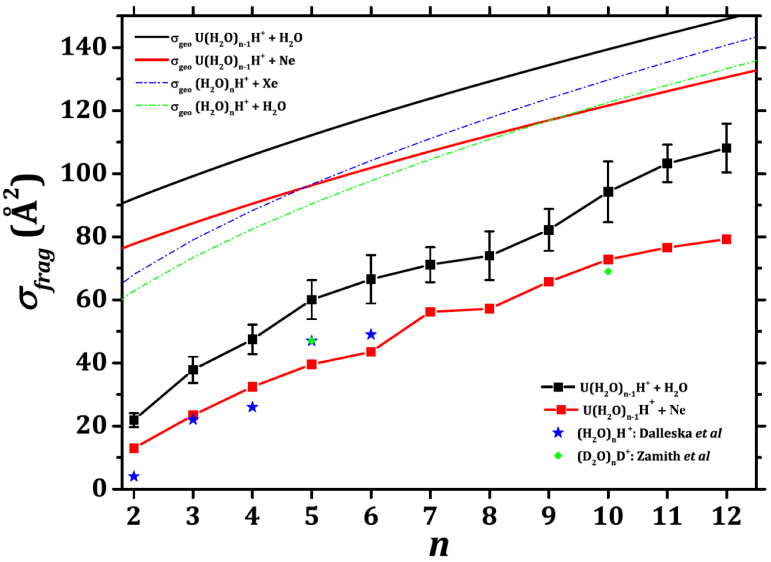

Figure 3.15: Fragmentation cross sections of clusters $(H_2O)_{n-1}UH^+$ at a collision energy of 7.2 eV plotted as a function of the total number n of molecules in the clusters. The experimental results and geometrical cross sections are shown for collision with H_2O and Ne. The results from N. Dalleska et al.[411] using Xe as target atoms on pure protonated water clusters $(H_2O)_{2-6}H^+$ and from S. Zamith *et al.* [412] using water as target molecules on deuterated water clusters $(D_2O)_{5,10}H^+$ are also shown. The geometrical collision cross sections of water clusters in collision with Xe atoms and water molecules are also plotted. Error bars represent one standard deviation.

Intermolecular fragmentation. Figure 3.16 displays the percentage of the fragments that have lost a neutral uracil molecule over all the fragments, plotted as a function of the number of water molecules in the parent cluster $(H_2O)_nUH^+$. It shows that for the cluster $(H_2O)_nUH^+$

with a small number of water molecules, almost no neutral uracil is evaporated. From n = 5 and more clearly from n = 6, the loss of neutral uracil molecule increases up to about 20% for $(H_2O)_9UH^+$.

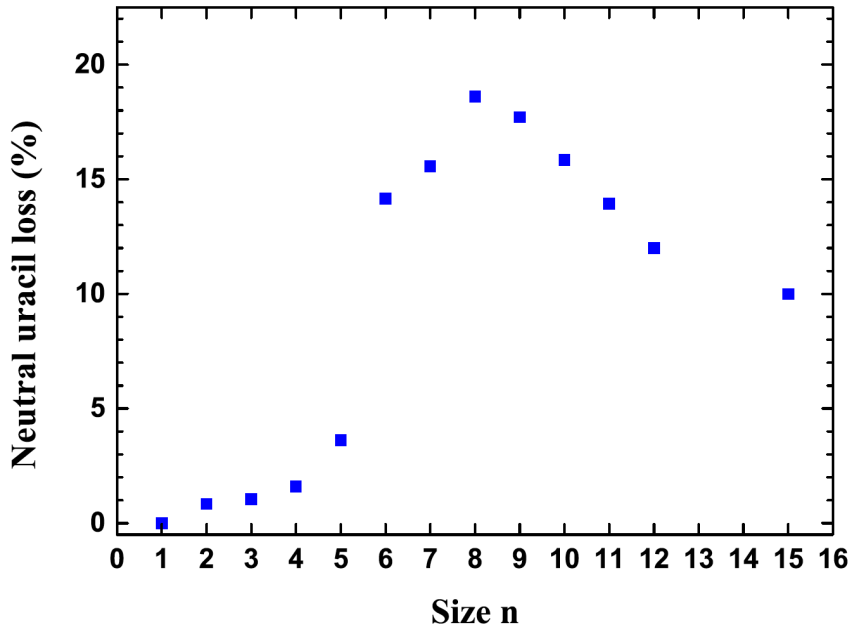

Figure 3.16: Proportion of neutral uracil molecule loss plotted as a function of the number of water molecules n in the parent cluster $(H_2O)_nUH^+$. Results obtained for collisions with Ne atoms at 7.2 eV center of mass collision energy.

The fragmentation can arise from two distinct mechanisms (direct and statistical fragmentation processes) depending on the life time of the collision complex. On the one hand, if the fragmentation occurs in a very short time after collision, the dissociation is impulsive (direct). In this case, I thus assume that the nature of the collision products is partly determined by the nature of the lowest-energy isomers of parent clusters and especially by the location of the excess proton in the structure. In other words, the lowest-energy isomer of the parent cluster obviously plays a major role in determining the fragmentation channels. On the other hand, in the case of long-lived collision complexes, collision energy is transferred to the parent cluster and is redistributed among all degrees of freedom. This is a slow process, and the structures involved during the fragmentation are no longer the lowest-energy isomer, *i.e.*, the structure of the cluster can undergo structural reorganizations before evaporation. Furthermore, the excess proton can also diffuse in the structure and for instance, recombine with the uracil. Then

the role of the initial structure of the parent clusters is strongly reduced in determining the fragmentation channels.

In Figure 3.16, I focus on the loss of the neutral uracil molecule in the detected fragments since it indicates where the proton lies after collision, namely, on the uracil or on a water cluster. A transition in the nature of fragmentation product is clearly seen from n = 5-6. To account for this transition, the evaporation originates from a direct fragmentation process is considered. A short discussion about the implications of possible structural rearrangement prior to dissociation, which occurs in a statistical process, will be provided in section 3.3.2.2.

The relative proton affinities of each component of the mixed clusters gives a first estimate of which molecule, uracil or water, is more likely to carry the positive charge prior to collisions. Experimentally, the gas phase proton affinity of uracil is bracketed to 9 $\pm$ 0.12 eV.[415] For the proton affinity of water molecule, an experimental value is reported at 7.31 eV [416] and a theoretical one at 7.5 eV.[417] In the work of H. Cheng, it shows that the proton affinity of water clusters increases with their size.[417] The proton affinities extracted from the different studies for the uracil molecule and for water clusters as a function of the number of water molecules are displayed in Figure 3.17.

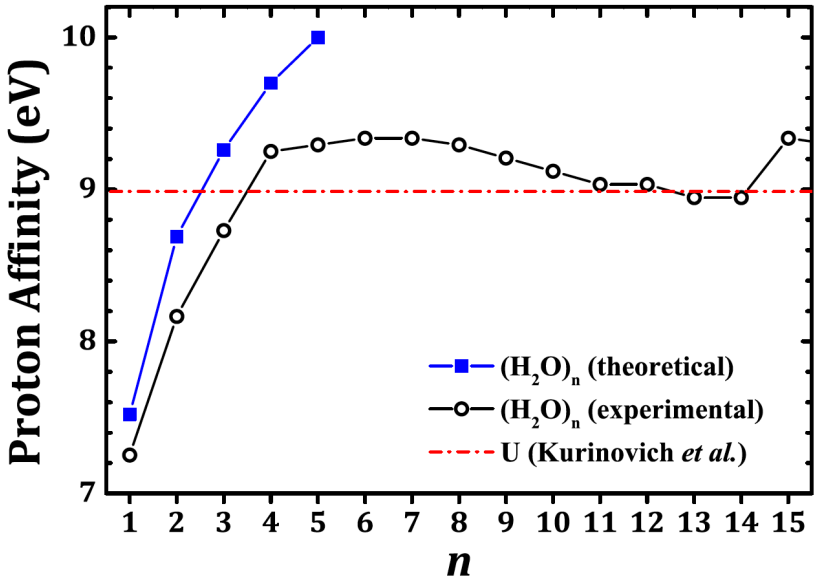

Figure 3.17: The proton affinities of water clusters as a function of the number of water molecules n, which are taken from the work of T. Magnera (black circles) [416] and from the work of Cheng (blue squares).[417] The value of the proton affinity of uracil (red dotted dashed line) is also plotted.[415]

It clearly shows that the proton affinity of uracil, PA[U], is larger than the one of water monomer PA[H_2O]. Thus, for the mono-hydrated uracil, from the energetic point of view, the proton is on the uracil molecule and the only observed fragments are indeed protonated uracil molecules. Moreover, an experimental work [404] confirms that there is no proton transfer from the uracil to the water molecule in mono-hydrated clusters. Proton affinity of the uracil molecule is also larger than that of the water dimer, or even the trimer: PA[U] $>$ PA[$(H_2O)_n$], n = 2 or 3 depending on the considered data for water. This is still consistent with our experimental observation of no neutral uracil molecule loss for n = 2 and 3. However from the PA values, one would predict that the appearance of neutral uracil should occur for n $\approx$ 3-4. For instance, for n = 4, assuming a statistical fragmentation for which the energies of final products are expected to be of relevance, the channel U + $(H_2O)_4H^+$ is energetically favorable. If one now assumes a direct dissociation, where the parent protonation state remains unchanged, one also expects that neutral uracil evaporates. However, experimentally, for n = 4, no neutral uracil evaporation is observed. The loss of neutral uracil starts at n = 5 and becomes significant only at n = 6.

This analysis based on PA is however quite crude. Indeed, it assumes that the protonated uracil cluster would be composed of a uracil molecule attached to an intact water cluster. However, one expects that the hydration of uracil may be more complicated than this simple picture. Therefore, the uracil hydration is explored theoretically in the next Section, Section 3.3.2.2, in order to determine the proton location more realistically.

3.3.2.2 Calculated Structures of Protonated Uracil Water Clusters

As discussed in section 3.2, I have proposed a modified set of N—H parameters to describe sp^3 nitrogen atoms. For, sp^2 nitrogen atoms there is no need to modify the integral parameters as SCC-DFTB describe them rather correctly. Consequently, only the D_{NH} parameter needs to be defined for the present calculations. Table 3.3 presents the binding energies of the two $(H_2O)U$ isomers represented in Figure 3.18 at MP2/Def2TZVP and SCC-DFTB levels of theory. Both D_{NH} = 0.12 and D_{NH} = 0.14 lead to reasonable binding energies. So, to be consistent with the work performed in the previous section, we have used D_{NH} = 0.12 in the following.

The lowest-energy isomers determined theoretically for hydrated uracil protonated clusters $(H_2O)_{1-7,11,12}UH^+$ are shown in Figures 3.19-3.28. In the experiments, clusters are produced at a temperature of about 25 K, so only a very few isomers are likely to be populated. Indeed, the clusters are produced in the canonical ensemble at the temperature $T_c \approx$ 25 K, so

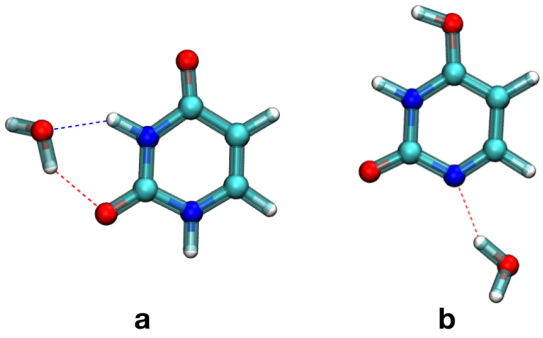

Figure 3.18: Structure of two (H_2O)U isomers used for binding energy calculations.

Table 3.3: Binding energy of two (H_2O)U isomers at MP2/Def2TZVP and SCC-DFTB levels of theory.

isomer	$E_{bind_{MP2}}$	$E_{bind_{DFTB}}$ $D_{NH_{0.0}}$	E_{Re} $D_{NH_{0.0}}$	$E_{bind_{DFTB}}$ $D_{NH_{0.12}}$	E_{Re} $D_{NH_{0.12}}$	$E_{bind_{DFTB}}$ $D_{NH_{0.14}}$	E_{Re} $D_{NH_{0.14}}$
a	-8.3	-8.6	-0.3	-9.8	-1.5	-10.0	-1.7
b	-6.9	-6.6	0.3	-6.9	0.0	-6.9	0.0

only isomers for which the Boltzmann factor exp(-$\Delta E k_B T_c$) is larger than 10^{-7} are considered here. In this formula, ΔE represents the relative energy of a considered isomer with respect to the lowest-energy one. Thus for each isomer, only the six lowest-energy structures of $U(H_2O)_{1-7,11,12}UH^+$ obtained from the PES exploration will be discussed.

Cluster (H_2O)UH^+. Figure 3.19 displays the six lowest-energy isomers obtained for (H_2O)UH^+. Two (1a and 1b) of them contain the u138-like isomer of U (each one with a different orientation of the hydroxyl hydrogen). Three of them (1c, 1d, and 1e) contain the u178 isomer and 1f contains the u137[341] isomer with a reverse orientation of the hydroxyl hydrogen. From those isomers, different sites are possible for the water molecule attachment which leads to variety of isomers even for such small size system. To the best of our knowledge, (H_2O)UH^+ is the most studied protonated uracil water cluster and our results are consistent with previous published studies. Indeed, S. Pedersen and co-workers [342] conducted ultraviolet action spectroscopy on (H_2O)UH^+ and discussed their measurements in the light of theoretical calculations performed on two isomers: ur138w8 (1a in the present study) and ur178w7 (1c).[342] Their energy ordering at 0 K is the same whatever the computational method they used: B3LYP/6-311++G(3df,2p), M06-2X/6-311++G(3df,2p),

MP2/6-311++G(3df,2p), CCSD(T)/6-311++G(3df,2p), and CCSD(T)/augcc-pVTZ and is similar to what I obtained. Similarly, J. Bakker and co-workers[404] considered three isomers: U(DK)H_W^+ (1a), U(KE)H_{Wa}^+ (1c), and U(KE)H_{Wb}^+ (1e) at the B3LYP/6-311++G(3df,2p) level of theory and obtained the same energy ordering as I did. Our methodology has thus allowed us to retrieve those isomers and to locate two new low-energy structures (1b and 1d). 1f is too high in energy to be considered in low-temperature experiments that are in the same range of relative energies but have never been discussed. To ensure that they are not artificially favored in our computational method, calculations were also performed at the B3LYP/6-311++G(3df,2p) level of theory. The results are presented in Figure 3.20, which are consistent with the MP2/Def2TZVP ones. This makes us confident in the ability of the present methodology to locate meaningful low energy structures. Importantly, no isomer with the proton on the water molecule was obtained, neither at the DFTB or MP2 levels.

Cluster $(H_2O)_{2-3}UH^+$. Figures 3.21 and 3.22 display the six lowest-energy isomers obtained for $(H_2O)_2UH^+$ and $(H_2O)_3UH^+$, respectively. For $(H_2O)_2UH^+$, the lowest energy structure, 2a contains the u138 isomer of uracil. 2b, 2d, and 2e contain u178 and 2c contains u138 with reverse orientation of the hydroxyl hydrogen. 2f contains u178 with reverse orientation of the hydroxyl hydrogen. This demonstrates that, similarly to $(H_2O)UH^+$, a diversity of uracil isomers are present in the low-energy structures of $(H_2O)_2UH^+$ which makes an exhaustive exploration of its PES more difficult. The same behavior is observed for $(H_2O)_3UH^+$. The configuration of u138 does not allow for the formation of a water dimer which leads to two unbound water molecules in 2a. By contrast, a water-water hydrogen bond is observed for 2b and 2c. The existence of a water dimer was not encountered in the low-energy isomers of the unprotonated $(H_2O)_2U$ species due to the absence of the hydroxyl group on U. It is worth pointing out that 2a, 2b, 2c, and 2d are very close in energy which makes their exact energy ordering difficult to determine. However, no isomer displaying an unprotonated uracil in the low-energy isomers of $(H_2O)_2UH^+$ was located. The lowest-energy structure of $(H_2O)_3UH^+$, 3a, is characterized by two water-water hydrogen bond that forms a linear water trimer. Higher energy isomers display only one (3b, 3d, and 3e) or zero (3c and 3f) water-water bond (see Figure 3.22). Similarly to $(H_2O)_2UH^+$, no isomer displaying an unprotonated uracil was located for $(H_2O)_3UH^+$.

Cluster $(H_2O)_{4-5}UH^+$. The six lowest-energy isomers obtained for $(H_2O)_4UH^+$ and $(H_2O)_5UH^+$ are displayed in Figures 3.23 and 3.24, which constitute a transition in the behavior of the proton. Indeed, in $(H_2O)_4UH^+$, two kind of lowest energy structures appear: (i)

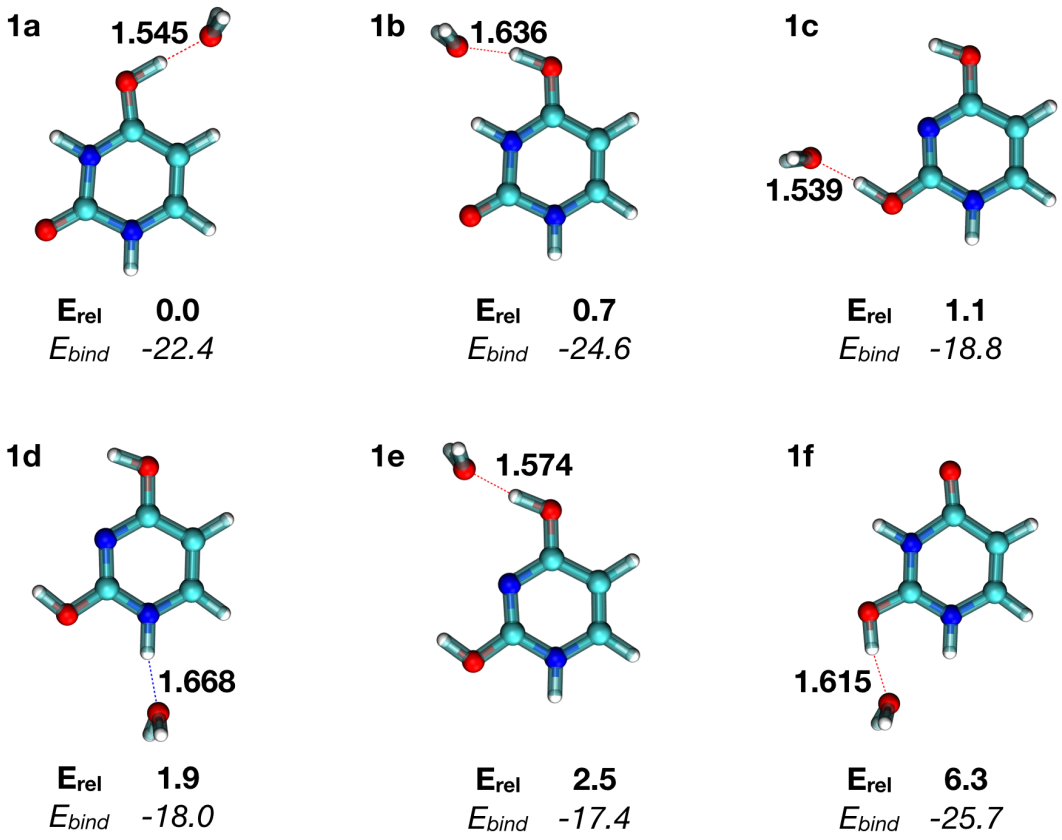

Figure 3.19: Lowest-energy structures of $(H_2O)UH^+$ obtained at the MP2/Def2TZVP level of theory. Relative (E_{rel}) and binding energies (E_{bind}) are given in kcal.mol^{-1}. Important hydrogen-bond distances are indicated in bold and are given in Å.

structures composed of UH^+, one water trimer, and one isolated water molecule (4b, 4d, 4e, and 4f); (ii) structures composed of U and a protonated water tetramer (4a and 4c). In the latter case, the hydronium ion is always bounded to an uracil oxygen atom. The U–H_2OH^+ bond is always rather strong as compared to U–H_2O bonds as highlighted by the corresponding short oxygen-hydrogen distance. Furthermore, speaking of distances, the difference between the U–H_2OH^+ and UH^+–H_2O forms is rather fuzzy and might be sensitive to computational parameters and also to quantum fluctuations of the hydrogen. This suggests that collision with $(H_2O)_4UH^+$ is more likely to induce evaporation of H_2O rather than H_2OH^+ or a protonated water cluster. The picture is significantly different in $(H_2O)_5UH^+$ where the lowest-energy structure displays a hydronium ion separated by one water molecule from U. Such structures do not appear in $(H_2O)_4UH^+$ due to the limited number of water molecules available to sepa-

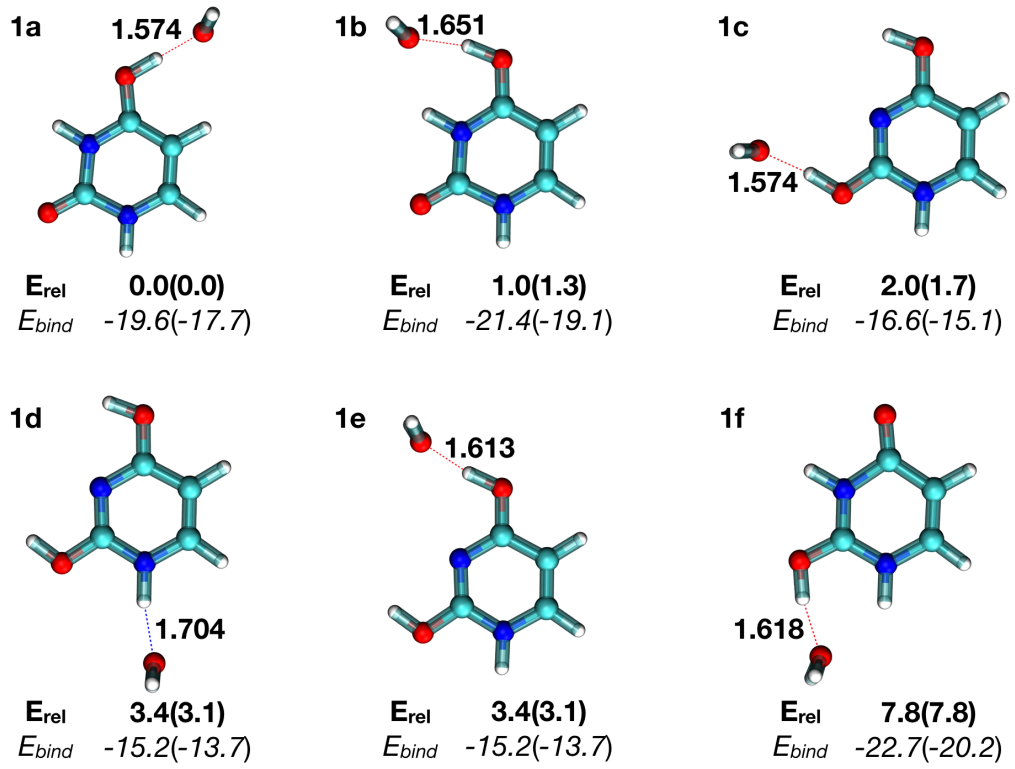

Figure 3.20: Lowest-energy structures of $(H_2O)UH^+$ obtained at the B3LYP/6-311++G(3df,2p) level of theory. Relative (E_{rel}) and binding energies (E_{bind}) are given in kcal.mol^{-1}. The corresponding values with ZPVE corrections are provided in brackets. Important hydrogen-bond distances are indicated in bold and are given in Å.

rate H_2OH^+ from U. Such separation suggests that, if considering a direct dissociation process, evaporation of neutral uracil can now occurs in agreement with the experimental observations (see discussion above). One can see that 5b, which is only 0.3 kcal.mol^{-1} higher in energy than 5a, still displays a U–H_2OH^+ link. This is in line with the low amount of neutral uracil that is evaporated in the experiment (see Figure 3.16).

Cluster $(H_2O)_{6-7}UH^+$. Figures 3.25 and 3.26 display the six lowest-energy isomers obtained for $(H_2O)_6UH^+$ and $(H_2O)_7UH^+$. Similarly to $(H_2O)_5UH^+$, the first lowest-energy structure, 6a and 7a, for both species $(H_2O)_6UH^+$ and $(H_2O)_7UH^+$ have the excess proton on a water molecule that is separated by one water molecule from the uracil. This appears to be common to the clusters with at least 5 water molecules. This is also observed for higher-energy isomers (6c, 6d, 7c, 7e, and 7f). Other characteristics of the proton are also observed: proton

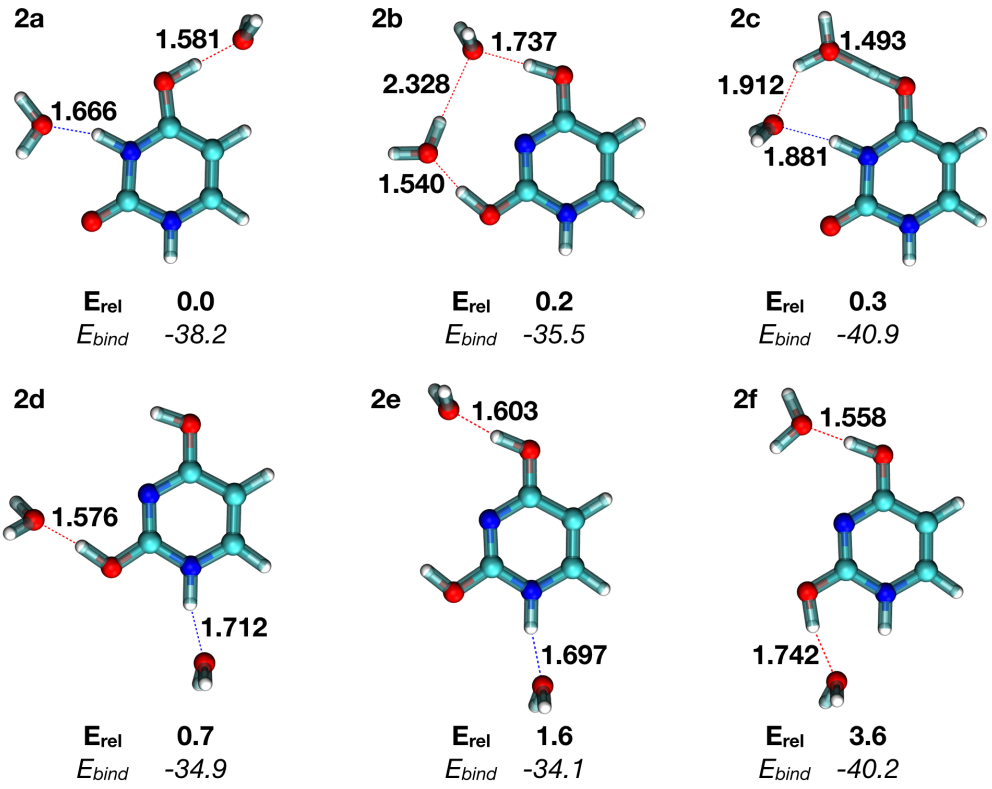

Figure 3.21: Lowest-energy structures of $(H_2O)_2UH^+$ obtained at the MP2/Def2TZVP level of theory. Relative (E_{rel}) and binding energies (E_{bind}) are given in kcal.mol^{-1}. Important hydrogen-bond distances are indicated in bold and are given in Å.

in a similar Zundel form [418] bounded to the uracil (6b, 6e, and 7d) or H_2OH^+ still bounded to uracil (6f and 7b).

Cluster $(H_2O)_{11-12}UH^+$. Finally, due to the neutral uracil loss proportion starts to decrease from n=9 (see Figure 3.16), which attracted us to perform the optimization of big cluster $(H_2O)_{11,12}UH^+$ as examples to explore why it has this change. The six lowest energy isomers obtained for cluster $(H_2O)_{11,12}UH^+$ are shown in Figures 3.27 and 3.28.

In all isomers (11a to 11f) of cluster $(H_2O)_{11}UH^+$, the excess is on the water cluster and was separated by water molecule from uracil. For 12a, 12b, 12c, and 12d, it is obvious that the excess proton is not directly bounded to the uracil. The uracil in 12a and 12d belongs to the di-keto form (there is a hydrogen atom on each nitrogen of uracil), and the excess proton was separated by one water molecule from uracil, additionally, the uracil is surrounded by the

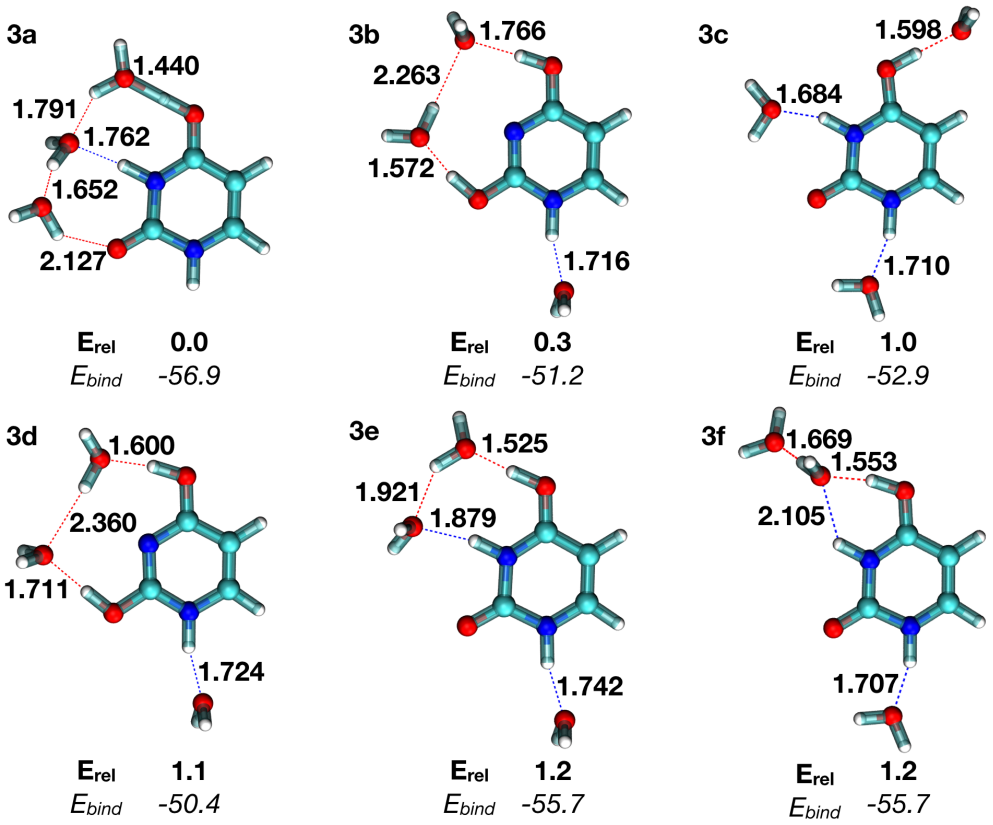

Figure 3.22: $(H_2O)_3UH^+$ lowest-energy structures obtained at the MP2/Def2TZVP level of theory. Relative (E_{rel}) and binding energies (E_{bind}) are given in kcal.mol^{-1}. Important hydrogen-bond distances are indicated in bold and are given in Å.

water cluster, all of these may lead the excess proton to go to the near oxygen atom of uracil. For 12b, the excess proton is on the water cluster and is very far from the uracil. For 12c, the excess proton was separately by one water molecule from uracil. For isomers 12e and 12f, the excess proton is between the uracil and a water molecule. The uracil is surrounded by the water cluster in 12e but it is not in 12f. Of course, for $(H_2O)_{11}UH^+$, $(H_2O)_{12}UH^+$, $(H_2O)_6UH^+$ and $(H_2O)_7UH^+$ and also $(H_2O)_4UH^+$ and $(H_2O)_5UH^+$, the amount of low-energy isomers is expected to be very large and do not intended to find them all. Furthermore, due to the limited number of MP2 geometry optimization I performed, there are few chances that I located the global energy minima for $(H_2O)_6UH^+$, $(H_2O)_7UH^+$, $(H_2O)_{11}UH^+$ and $(H_2O)_{12}UH^+$. However, the general picture I am able to draw from the present discussed structures fully supports the experimental results: from $(H_2O)_5UH^+$, it exists low-energy structures populated at very

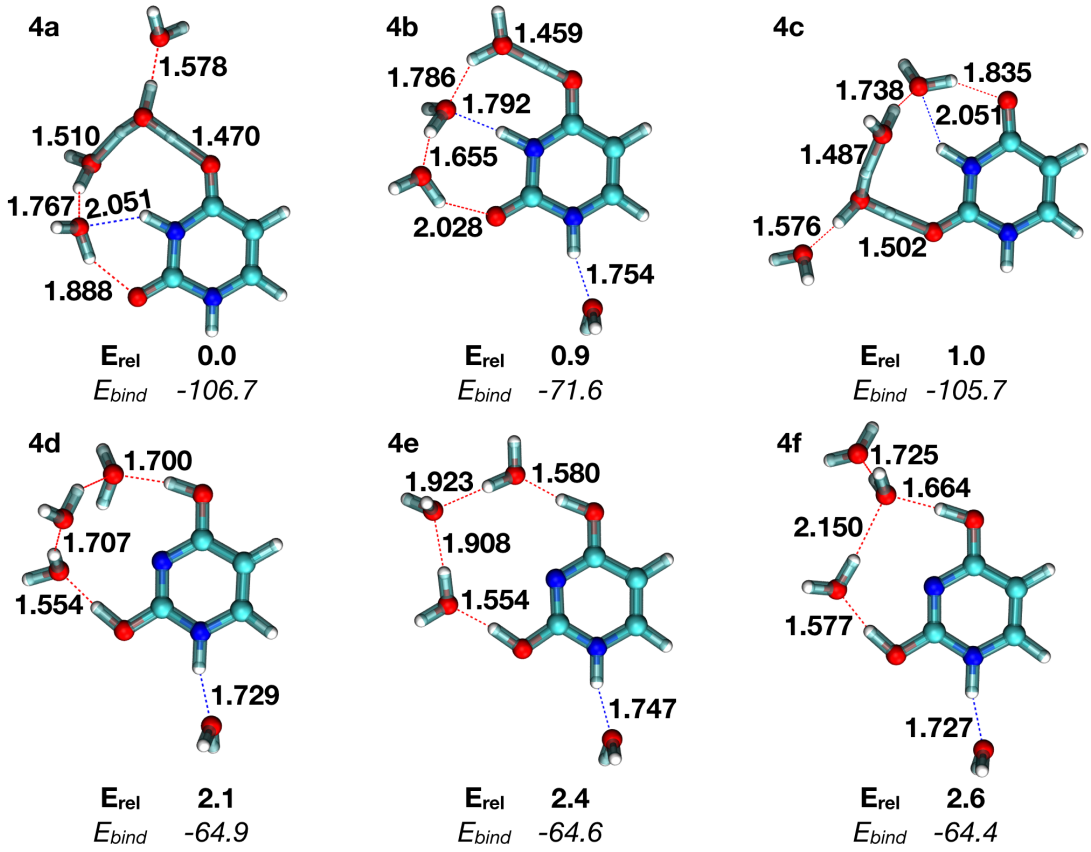

Figure 3.23: Lowest-energy structures of $(H_2O)_4UH^+$ obtained at the MP2/Def2TZVP level of theory. Relative (E_{rel}) and binding energies (E_{bind}) are given in kcal.mol^{-1}. Important hydrogen-bond distances are indicated in bold and are given in Å.

low temperature in which the excess proton is not directly bound to the uracil molecule. Upon fragmentation, this allows the proton to remain bounded to the water molecules.

All the aforementioned lowest energy structures are relevant to describe the $(H_2O)_{1-7,11,12}UH^+$ species at low temperature and to understand the relation between the parent cluster size and the amount of evaporated neutral uracil in the case of direct dissociation. However, as already stated, one has to keep in mind that upon collision statistical dissociation can also occur. In that case, structural rearrangements are expected to occur which are important to understand each individual mass spectra of the $(H_2O)_{1-15}UH^+$ clusters and the origin of each collision product. For instance, the fragment UH^+ is detected for all cluster sizes in experiment. This means that for the largest sizes, for which I have shown from the calculation that the proton is located away from the uracil, proton transfer does occur prior to dissociation.

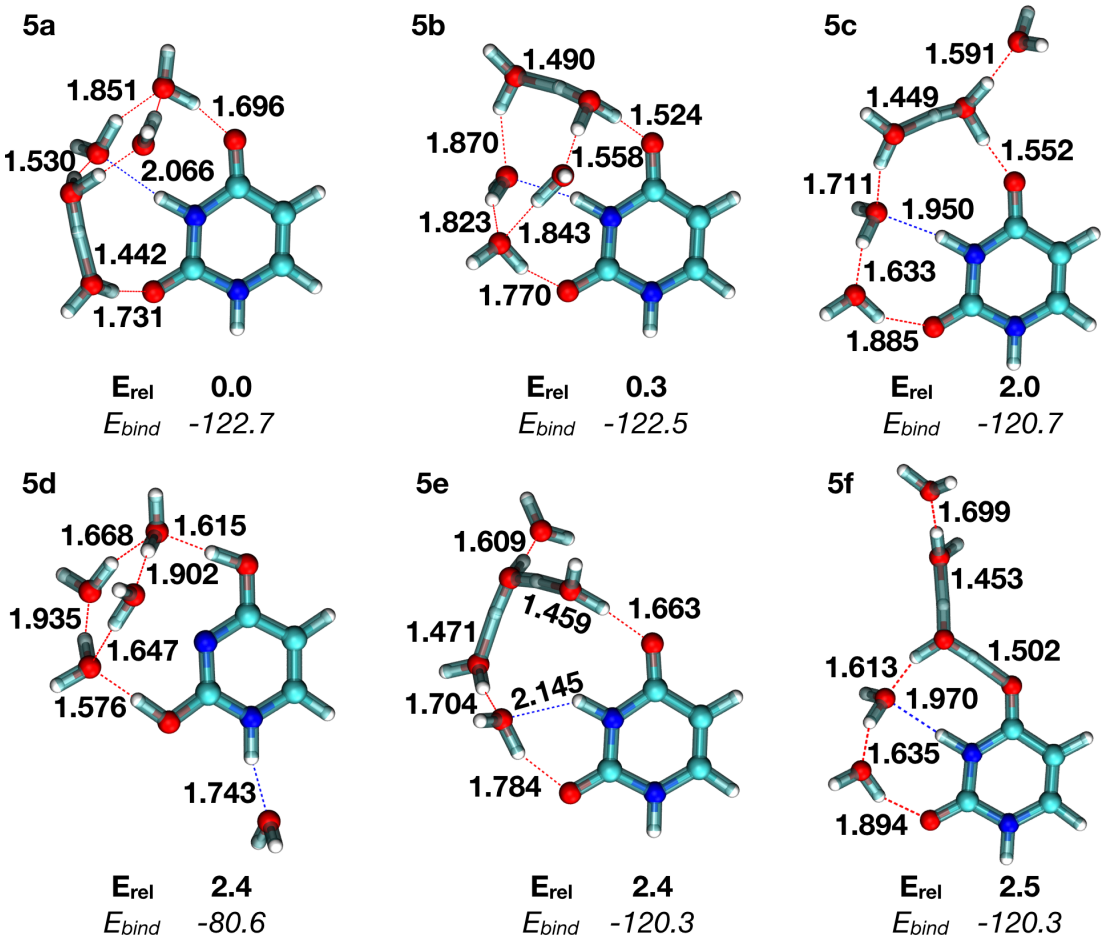

Figure 3.24: Lowest-energy structures of $(H_2O)_5UH^+$ obtained at the MP2/Def2TZVP level of theory. Relative (E_{rel}) and binding energies (E_{bind}) are given in kcal.mol^{-1}. Important hydrogen-bond distances are indicated in bold and are given in Å.

One possible scenario is that after collision, water molecules sequentially evaporates. When the number of water molecules is small enough, the proton affinity of uracil gets larger than the one of the remaining attached water cluster. Proton transfer is then likely and therefore protonated uracil can be obtained at the end.

If one turns to the neutral uracil evaporation channel, it appears that the smaller clusters H_2OH^+ and $(H_2O)_2H^+$ are not present in the time-of-flight mass spectra. This absence might have two origins. First, the dissociation energies of the protonated water monomers and dimers are substantially higher than larger sizes, and they are therefore less prone to evaporation. Second, as already mentioned, for such small sizes, the proton affinity of uracil gets larger than

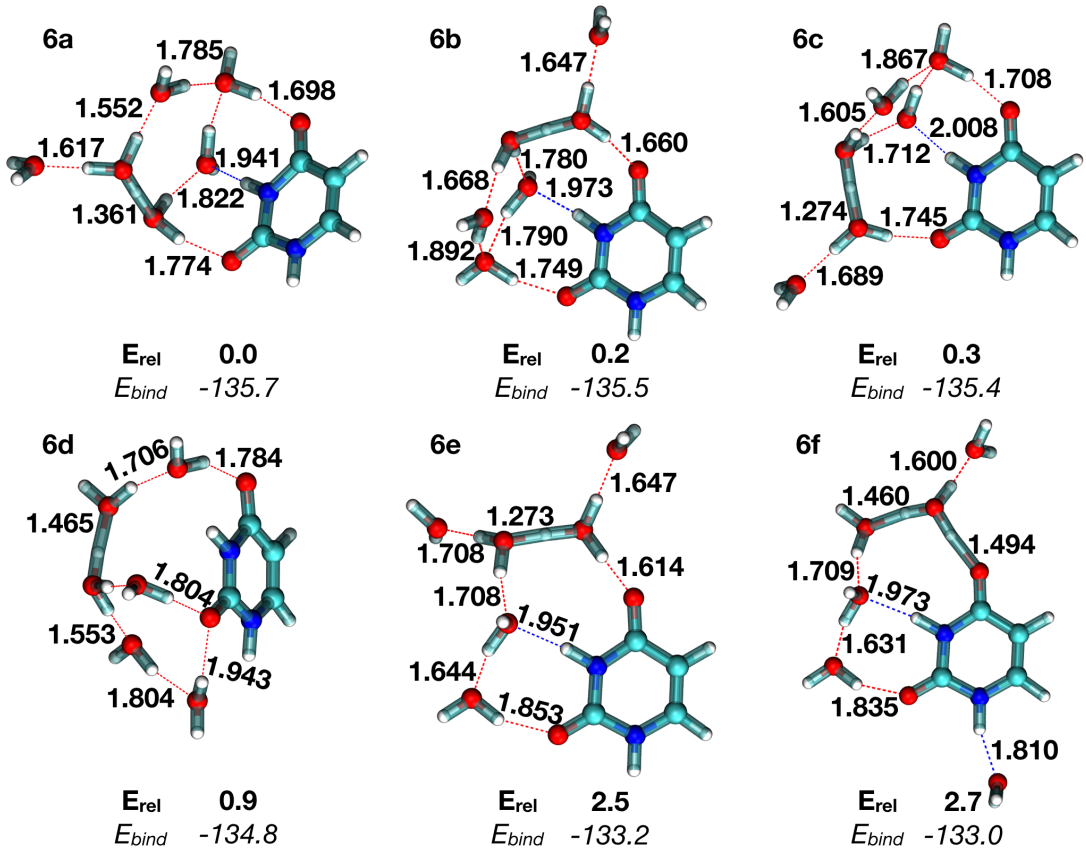

Figure 3.25: Lowest-energy structures of $(H_2O)_6UH^+$ obtained at the MP2/Def2TZVP level of theory. Relative (E_{rel}) and binding energies (E_{bind}) are given in kcal.mol^{-1}. Important hydrogen-bond distances are indicated in bold and are given in Å.

the one of the water dimer or trimer and proton transfer to the uracil is likely to occur.

In order to confirm the above scenarios, simulations and/or evaporation rate calculation would have to be conducted to describe the fragmentation channels in details. MD simulations of protonated uracil have already been performed by R. Spezia and co-workers to understand the collision-induced dissociation.[143, 403] Although, in the present case, the initial position of the excess proton appears as a key parameter to explain the evaporation of neutral uracil, such MD simulations could be additionally conducted to provide a clearer picture on the various evaporation pathways, which will be shown in section 4.3.

3.3.3 Conclusions on $(H_2O)_nUH^+$ clusters

The work in this section presents the collision-induced dissociation of hydrated protonated uracil $(H_2O)_{1-15}UH^+$ clusters and their experimental absolute fragmentation cross sections. The experiments demonstrate that the evaporation channels evolve with size: Below $n = 5$, the observed charged fragments always contain the uracil molecule, whereas from $n = 5$, the loss of a neutral uracil molecule becomes significant. To understand this transition, I conducted an exhaustive exploration of the potential energy surface of $(H_2O)_{1-7,11,12}UH^+$ clusters combining a rough exploration at the SCC-DFTB level with fine geometry optimizations at the MP2 level of theory. Those calculations show that below $n = 5$, the excess proton is either on the uracil or on a water molecule directly bound to uracil, *i.e.*, forming a strongly bound U–H_2OH^+ complex. From $n = 5$ and above, clusters contain enough water molecules to allow for a net separation between uracil and the excess proton: The latter is often found bound to a water molecule which is separated from uracil by at least one other water molecule. Upon direct dissociation, the excess proton and the uracil can thus belong to different fragments. This study demonstrates that combination of collision-induced dissociation experiments and theoretical calculation allows to probe the solvation and protonation properties of organic molecules such as nucleobases. This is a step toward a better understanding of the role of water in the chemistry of in vivo DNA and RNA bases. However, the knowledge of the lowest-energy isomers of the species involved in CID experiments is not enough to understand all the collision process. To get a deeper understanding of the collision mechanism, an explicit modelling of the collision is needed. This question is addressed in the next chapter of this thesis.

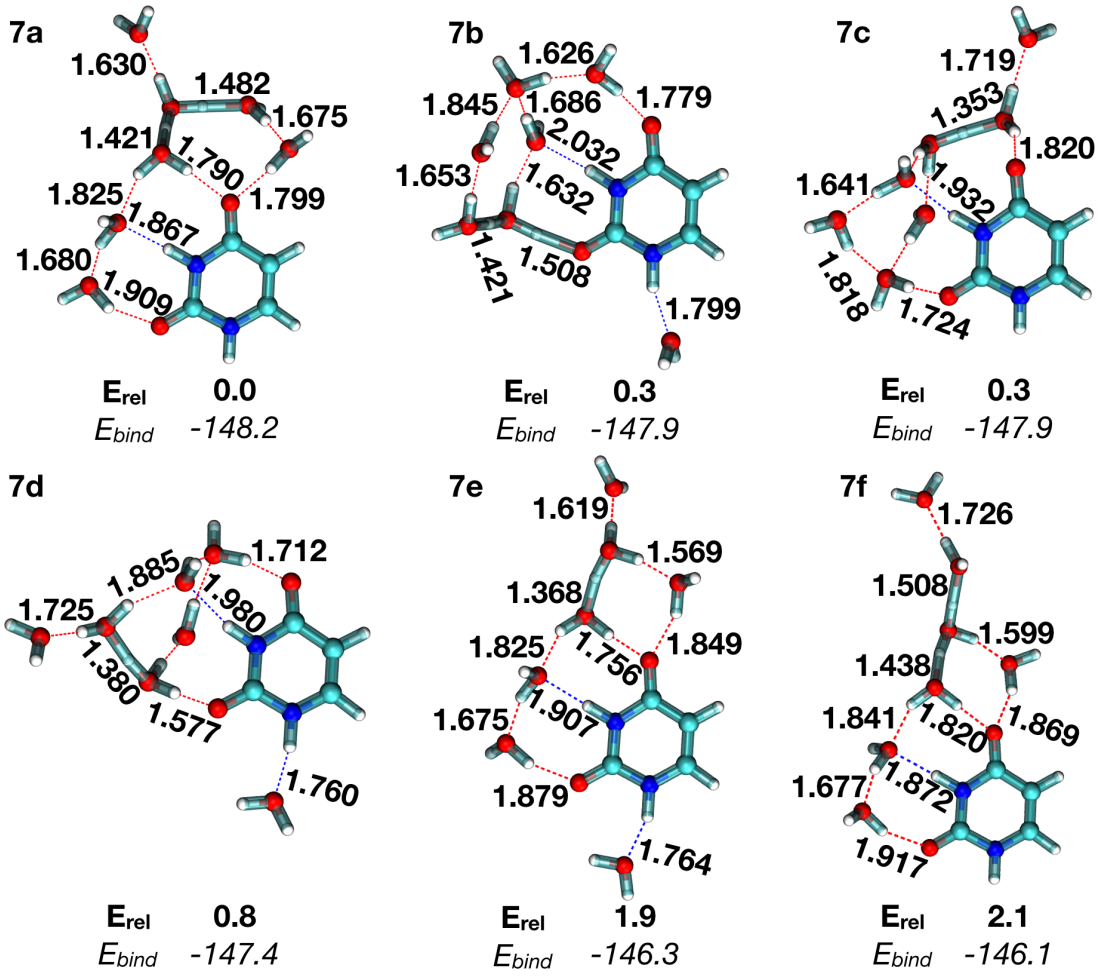

Figure 3.26: Lowest-energy structures of $(H_2O)_7UH^+$ obtained at the MP2/Def2TZVP level of theory. Relative (E_{rel}) and binding energies (E_{bind}) are given in kcal.mol^{-1}. Important hydrogen-bond distances are indicated in bold and are given in Å.

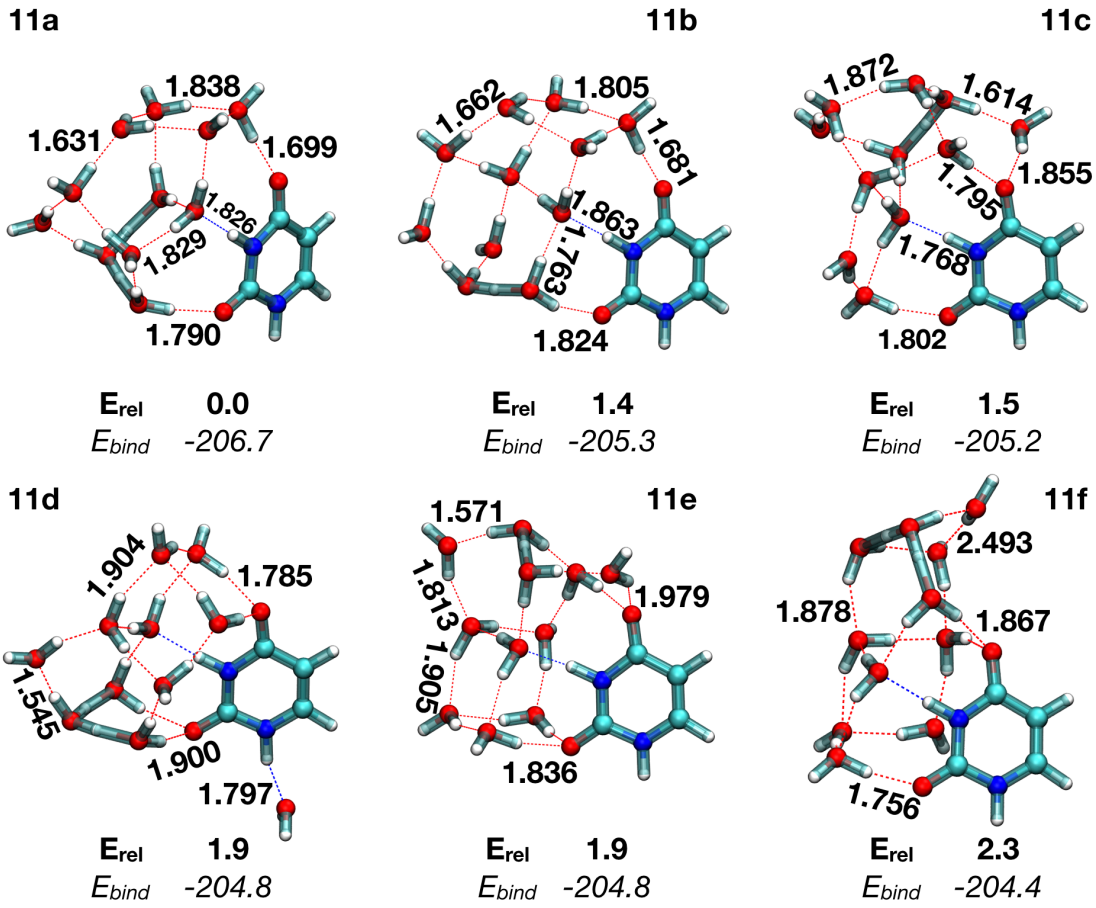

Figure 3.27: Lowest-energy structures of $(H_2O)_{11}UH^+$ obtained at the MP2/Def2TZVP level of theory. Relative (E_{rel}) and binding energies (E_{bind}) are given in kcal.mol^{-1}. Important hydrogen-bond distances are indicated in bold and are given in Å.

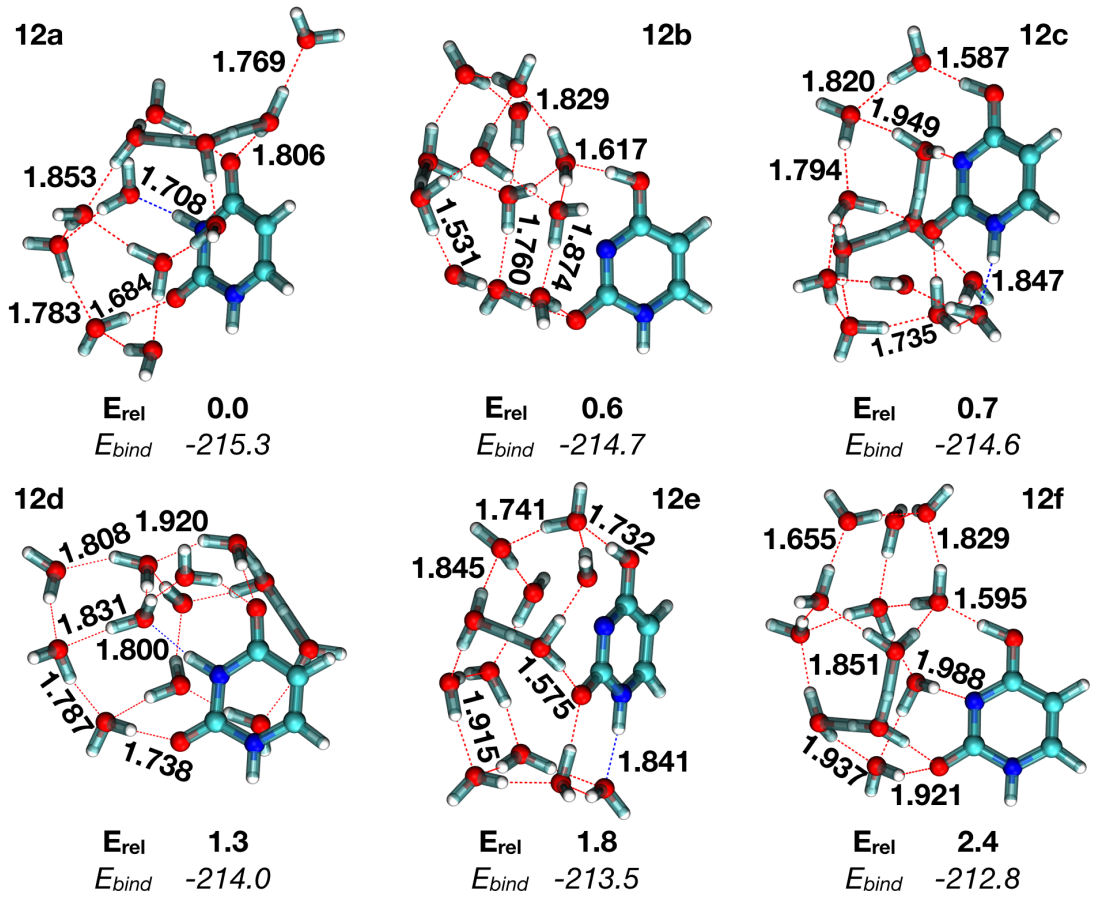

Figure 3.28: Lowest-energy structures of $(H_2O)_{12}UH^+$ obtained at the MP2/Def2TZVP level of theory. Relative (E_{rel}) and binding energies (E_{bind}) are given in kcal.mol^{-1}. Important hydrogen-bond distances are indicated in bold and are given in Å.

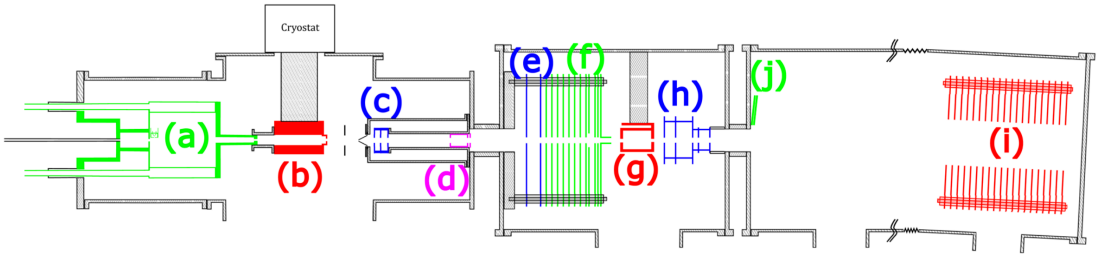

Figure 4.1: Schematic view of the experimental setup. (a) Cluster gas aggregation source. (b) Thermalization chamber. (c) First Wiley–McLaren acceleration stage. (d) Massfilter. (e) Energy focusing. (f) Deceleration. (g) Collision cell. (h) Second Wiley–McLaren acceleration stage. (i) Reflectron. (j) Micro-channel plate detector.

In the second mode, all the electrodes were used to mass-select the clusters. In order to perform collisions between the mass-selected clusters and the rare gas atoms, precisely delayed high voltage pulses were applied to electrodes (c)-(f). Pulsed high voltages applied to the first Wiley–McLaren electrodes (c) accelerate all the clusters, giving them an average kinetic energy of 622 eV. The applied voltages and the spacing between the electrodes of the Wiley-McLaren are chosen such that, 26 cm downstream, there is a linear relation (to first order) between the position of clusters and their kinetic energy. Using a pulsed high voltage, an electric field is created in this region (e) that compensates this linear kinetic energy dispersion, and all clusters finally have the same kinetic energy within a few electron volts. The time at which this pulsed high voltage is applied determines which cluster size is correctly energy focused. After this kinetic energy focusing, ions are decelerated by a potential barrier (f). At the end of the potential barrier, the potential is shut down in a field free zone and the mass-selected clusters then fly freely through the collision cell (g) up to the second Wile-McLaren acceleration stage (h). Clusters are then mass-analyzed using the reflectron (i) and the MCP detector (j). High voltage is applied on the mass filter (d) when the mass of interest enters the cylinder and shut down before it comes out. This allows us to eliminate part of the neighboring masses. In the experiments of pyrene clusters, the kinetic energy of the clusters in the laboratory frame is varied between 5 eV and 200 eV. For the experiments of protonated uracil water clusters, the kinetic energy of the clusters in the laboratory frame is 100 eV.

Kinetic energies of the ions can be easily deduced from experimental parameters. Indeed, since the distances in the apparatus are well-known, measuring, for instance, the time the ions take to travel from the end of the slowing down stage to the second acceleration stage gives the speed of the ions. More precise kinetic energy calibration is obtained by recording the

signal of the ions as a function of delays and/or voltages. These curves are then reproduced by simulations to obtain the kinetic energy distribution of the ions. [446]

The simplified experiment setup is shown in Figure 4.2. Clusters are produced in a gas aggregation source and thermalized at a temperature of 25 K. Clusters are then mass-selected with a chosen kinetic energy, which collide with argon atoms in a collision cell. The collision products are then analysed by TOFMS.

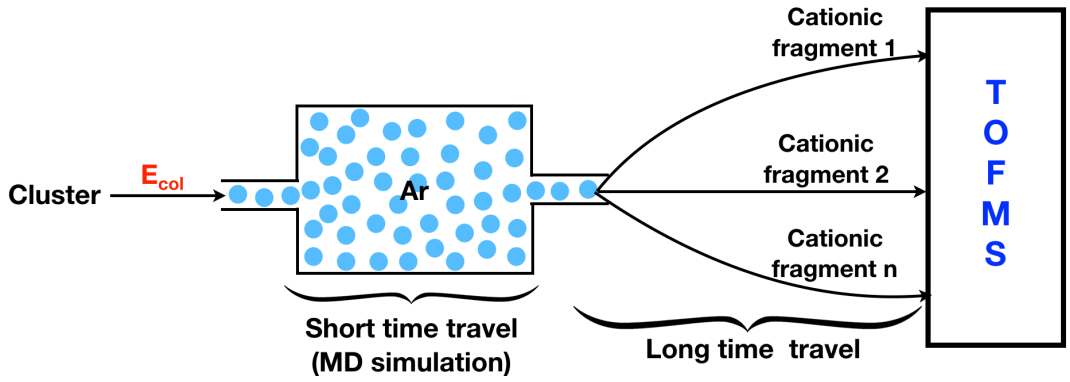

Figure 4.2: Schematic of the simplified experimental setup.

4.2 Computational Details

4.2.1 SCC-DFTB Potential

For the work in this chapter, the SCC-DFTB in combination with the mio-set for the Slater-Koster tables of integrals is applied. [168, 169, 218, 219, 447, 448] The SCC-DFTB potential for protonated uracil water clusters is shown in section 3.1.

DFTB is an efficient tool to perform MD simulations, in particular addressing the evaporation/dissociation processes in various chemical systems. [62, 449, 450, 451] The dynamics simulations of the collision process were performed with a QM/MM scheme [452] whose details can be found in the original paper[453, 454]. The projectile argon is treated as a polarisable MM particle interacting with the target (protonated uracil water cluster or pyrene dimer cation Py_2^+), the latter being treated at the DFTB level. The oscillation problem often appears for dissociated or close to dissociation systems. For the collision trajectories described below, a Fermi distribution (Fermi temperature 2000 K) was applied to avoid oscillation issues during the self-consistent procedure.[455] The Fermi distribution allows to recover the continuity in

energy and gradients in the case of level crossing. [455] It should be mentioned that, in order to keep a low computational cost, no correction has been used to improve the DFTB charge resonance description. However, this charge delocalization issue has been specifically addressed in the case of PAH cation dissociation and it was shown to have a minor effect on the final computed mass spectra [449]. I also mention that the collision energy is in principle high enough to have electronic excitation in the system, which is taken into account at a crude level by the use of a Fermi temperature. Finally, nuclear quantum effects are not taken into account. Although this may affect the results at very low collision energies, the effect is expected to be small for the experimental collision energies of 7.2 eV and 17.5 eV. Although all these limits should be kept in mind, I would like to emphasize that, recently, the dissociation of PAH molecules has been simulated and a good agreement with experimental results was obtained despite similar crude approximations, namely neglect of non-adiabatic and nuclear quantum effects, improper treatment of charge delocalization and use of a Fermi temperature [449, 451, 456].

4.2.2 Collision Trajectories

The preparation for the collisional trajectories for the collision of protonated uracil water clusters or Py_2^+ with Ar is the same. The schematic example for the collision of Py_2^+ with Ar is shown in Figure 4.3. Starting from the optimized Py_2^+ geometry [457], a preliminary thermalization run of 200 fs at 25 K (maintained by a Nosé-Hoover chain thermostat [309, 311]) is performed. Then, the argon atom projectile is introduced in the simulation with a velocity determined to reproduce a given collision energy. The target dimer Py_2^+ was positioned at the origin of the simulation referential and randomly rotated to allow all possible impact points on the dimer. The argon atom is initially positioned at x=10, y=b and z=0 Å, with b being the impact parameter. At each center of mass collision energy E_{col}, a series of 300 collision trajectories were conducted (the center of mass of the aggregate was kept at position (0, 0, 0)) for each of the 13 b values which are evenly distributed (interval being 0.5 Å) between 0 and R+0.5 Å. R refers to the radius of Py_2^+. 600 collision trajectories were performed per isomer of protonated uracil water clusters. Trajectory calculations have been performed with a time step of 0.5 fs and a total duration of 15 ps and 3 ps for the collision of argon with protonated uracil water clusters and Py_2^+, respectively. For the collision of Py_2^+ with argon, I have checked that for high collision energies such as 20 and 25 eV, a time step of 0.1 fs does not change significantly our numerical results, which will be shown in section 4.4.4.2.

It should be noted that the quaternion was used for rotation process in the generation of initial inputs. This approximation allows us to go from $3n-6$ degrees of freedom to $6N-6$, where n and N are the number of atoms and the number of molecules (3 degrees of translation and 3 degrees of rotation) in a system, respectively. The complex quaternion formalism ($\boldsymbol{q}$ = q_0, q_1, q_2, q_3) was used o describe the orientation of a solid body with respect to Euler angles ((θ, ϕ, ψ)) formalism. The quaternions involve an additional degree of freedom (similar to a homothety), which can be offset by using a normalization constraint on the vector $\boldsymbol{q}$:

$$q_0^2 + q_1^2 + q_2^2 + q_3^2 = 1 \tag{4.2}$$

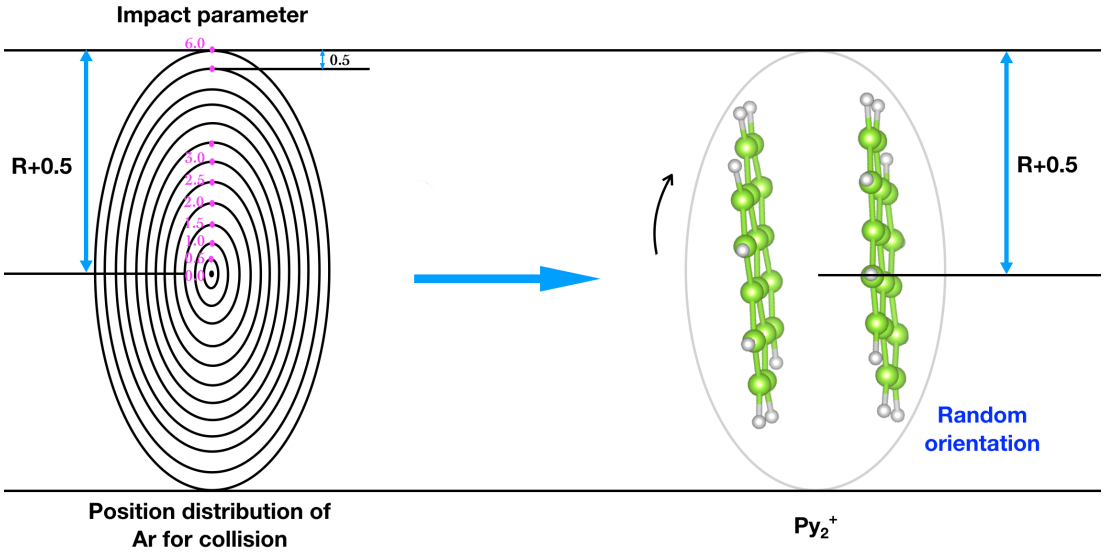

Figure 4.3: Schematic of the generation of the initial inputs.

4.2.3 Trajectory Analysis

During the results collection, the final snapshot was extracted for each trajectory. For collision of between Py_2^+ and argon, when the center of mass of the two pyrene monomer is more than 10 Å, a dissociation is defined. For the dissociaton definition of protonated uracil water clusters, it is a little more complicated than Py_2^+. A fragment is defined as a group of atoms in which the distance of any pair of adjacent atoms is less than 5.0 Å. The number of hydrogen, nitrogen and oxygen atoms in one fragment is denoted by k, l and m, respectively. For instance, a fragment

characterised by $l = 0$ and $k = 2m + 1$ is a pure water cluster containing the excess proton. Identifying such a fragment at the end of the trajectory means that a neutral uracil fragment exists, otherwise the excess proton is located on a uracil containing fragment. In practice, at each time step, the fragments are identified on the basis of their k, l, m values, allowing to record their time-dependent evolution. The mass spectrum is built retaining only the fragments containing the excess proton, as only charged fragments are detected in the experiment.

The opacity $P(b, E_{col})$, *i*.e. the dissociation probability as a function of impact parameter at a given collision energy is computed by averaging the results over the simulations corresponding to these conditions. The cross sections are then derived from the following formula:

$$\begin{aligned} \sigma_{frag}(E_{col}) &= \int_0^{b_{max}} 2\pi P(b, E_{col}) b db \\ &\simeq \sum_{i=0}^{b_{max}} \frac{P(b_i, E_{col}) + P(b_{i+1}, E_{col})}{2} \pi (b_{i+1}^2 - b_i^2) \end{aligned} \tag{4.3}$$

Mean values are computed using the same approach, followed by a division by πb_{max}^2. When mean values are restricted to trajectories leading to dissociation (noted $-d$) or not (noted $-ud$), additional normalisation by the total number of dissociated or undissociated trajectories is also necessary.

4.3 Dynamical Simulation of Collision-Induced Dissociation of Protonated Uracil Water Clusters

4.3.1 Introduction

Motivated by the recent CID experiments conducted by I. Braud *et al.* consisting in $(H_2O)_{1-15}UH^+$ clusters colliding with an impacting atom or molecule M (M = H_2O, D_2O, neon, and argon) at a constant center of mass collision energy of 7.2 eV,[104] the dynamical simulations of the collision between the protonated uracil water clusters $(H_2O)_{1-7,11,12}UH^+$ and an argon atom were performed. The low collision energy (7.2 eV) only leads to intermolecular bond breaking, without any electronic excitation, rather than intramolecular bond breaking. The branching ratios for different charged fragments were determined in experiment, which allows to deduce the fragmentation cross section for all $(H_2O)_{1-15}UH^+$ species and the location of the excess proton after collision: on a uracil containing cluster or on a pure water cluster. This allows to determine the proportion of neutral uracil loss (corresponding to cases where the excess proton is located on pure water clusters) as a function of the number n of water molecules. A

sharp increase of neutral uracil loss was observed for n = 5-6 (2.8% and 25.0% for n = 4 and 7, respectively). Those experiment were complemented by theoretical calculations that aim at characterizing the lowest-energy isomers of $(H_2O)_nUH^+$ (n = 1-7, 11, 12) clusters (see section 3.3), which shows that the location of the proton after collision recorded in the CID experiment is determined by its position in the lowest-energy parent isomer. In other words, a shattering mechanism occurs after collision. Despite these findings, static calculations can not provide a full picture for the fragmentation process and some issues are still not properly understood: (i) What is the main path of the fragmentation mechanisms? (ii) What are the fragments after collision? (iii) How does the proportion of fragments change according to time? (iv) Is the proportion of neutral uracil molecules loss only determined by the nature of the lowest-energy isomers?

To answer these questions, this simulations present a complete MD study of the fragmentation process for $(H_2O)_{1-7,11,12}UH^+$ aggregates colliding with an argon atom. Section 4.3.2 discusses the statistical convergence of collision trajectories, theoretical time-dependent proportion of fragments, proportion of neutral uracil loss, total fragmentation cross sections and mass spectra of fragments bearing the excess proton. These data are compared to available experimental results in order to discuss in details dissociation mechanism as a function of n. The main outcomes are summarized in section 4.3.7.

4.3.2 Results and Discussion

4.3.2.1 Statistical Convergence

In order to ensure that the statistical convergence is reached in the collision trajectories, initial conditions have to reproduce all possible collision orientation with good statistics. The procedure to generate a set of collision trajectories is described in section 4.2.2. As a visual proof, pictures a, b and c in Figure 4.4 represent 200, 400 and 600 random argon orientations with impact parameter being 0 for cluster $(H_2O)_3UH^+$, respectively. In these pictures, $(H_2O)_3UH^+$ is fixed and all initial positions for argon are orientated which leads to distribution maps of the initial positions of argon with respect to fixed $(H_2O)_3UH^+$. It is worth pointing out that in the collision trajectories, argon is fixed and uracil is rotated. Picture d in Figure 4.4 presents 200 random argon orientations with impact parameter being 0.0 and 6.0, respectively. The similar pictures for cluster $(H_2O)_{12}UH^+$ are displayed in Figure 4.5. These Figures demonstrate that

the more collision trajectories are performed, the more colliding opportunities of argon at all possible orientations are obtained.

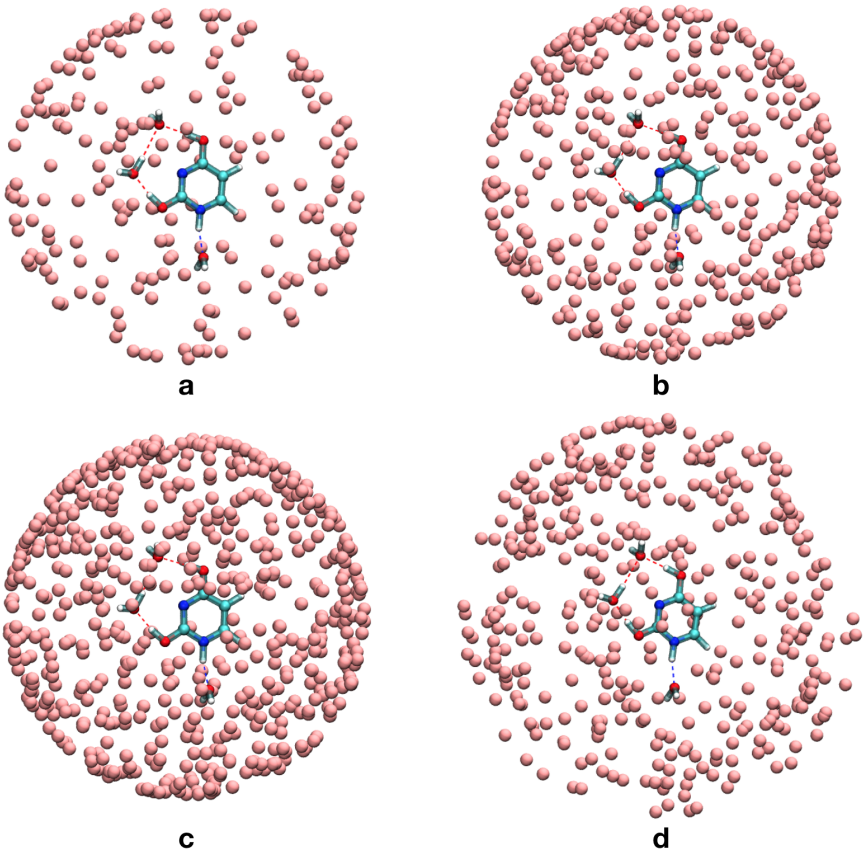

Figure 4.4: Schematic representation of random argon orientations for the collision with the second lowest-energy isomer of cluster $(H_2O)_3UH^+$. 200 (a), 400 (b) and 600 (c) random argon orientations are generated with impact parameter being 0. 200 orientations are generated with impact parameter being 0 and 6 (d), respectively.

In addition, to confirm that statistical convergence is reached for the properties discussed in sections 4.3.3, 4.3.4, 4.3.5, and 4.3.6, Tables 4.1 and 4.2 present the P_{NUL} involved from the

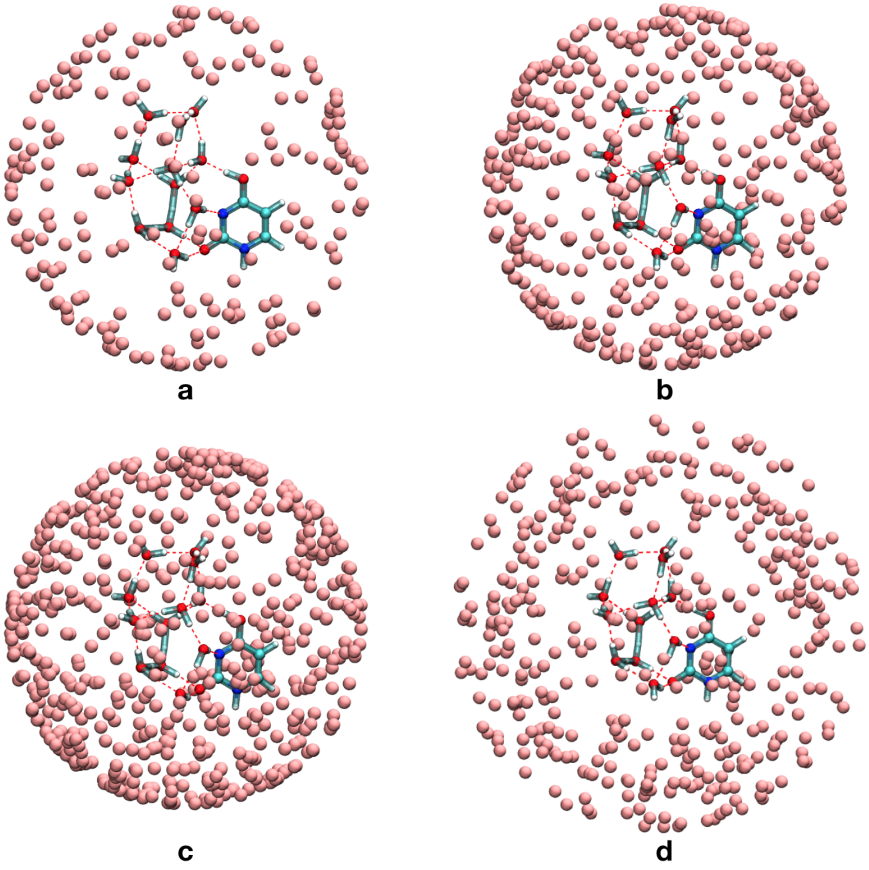

Figure 4.5: Schematic representation of random argon orientations for the collision with the second lowest-energy isomer of cluster $(H_2O)_{12}UH^+$. 200 (a), 400 (b) and 600 (c) random argon orientations are generated with impact parameter being 0. 200 orientations are generated with impact parameter value being 0 and 7 (d), respectively.

following formula 4.4

$$\begin{aligned} P_{NUL}(E_{col}) &= \int_0^{b_{max}} N_{NUL}(b,E_{col})2\pi b db \Big/ \int_0^{b_{max}} N_{frag}(b,E_{col})2\pi b db \\ &\simeq \frac{\sum_{i=0}^{b_{max}} \frac{1}{2}(N_{NUL}(b_i,E_{col})+N_{NUL}(b_{i+1},E_{col}))\pi(b_{i+1}^2-b_i^2)}{\sum_{i=0}^{b_{max}} \frac{1}{2}(N_{frag}(b_i,E_{col})+N_{frag}(b_{i+1},E_{col}))\pi(b_{i+1}^2-b_i^2)} \end{aligned} \tag{4.4}$$

and σ_{frag} of two isomers (the first lowest energy isomer and the one whose P_{NUL} fits best to the experiment results (in bold)) of each cluster $(H_2O)_{1-7,11,12}UH^+$ obtained from 200, 400, and 600 random argon orientations per impact parameter value.

Table 4.2: The proportions of P_{NUL} and σ_{frag} of first lowest-energy isomer and the isomer whose P_{NUL} fits the experiment (in bold) of $(H_2O)_{6,7,11,12}UH^+$ with simulations of 200, 400, and 600 as initial conditions.

Cluster	Simu	P_{NUL} (%)	σ_{frag} (Å^2)
6a	200	38.0	46.6
6a	400	38.0	45.6
6a	600	39.3	45.8
6f	200	18.9	54.2
6f	400	19.0	55.2
6f	600	18.5	55.0
7a	200	29.5	54.8
7a	400	31.3	53.4
7a	600	31.3	53.4
7d	200	22.6	55.3
7d	400	22.9	54.3
7d	600	23.0	54.0
11a	200	26.7	53.8
11a	400	28.2	53.5
11a	600	28.3	52.9
11d	200	14.5	55.2
11d	400	15.4	56.1
11d	600	15.6	56.5
12a	200	8.0	59.2
12a	400	7.5	60.5
12a	600	7.6	60.2
12c	200	10.4	55.3
12c	400	10.8	55.8
12c	600	10.8	55.4

4.6-4.8. In contrast, cluster with 11 (see Figure 4.9) and 12 water molecules shows a behavior compatible with a certain amount of statistical dissociation, namely a long-time evolution that allows structural rearrangements. These important observations can now be refined by looking at more detailed properties.

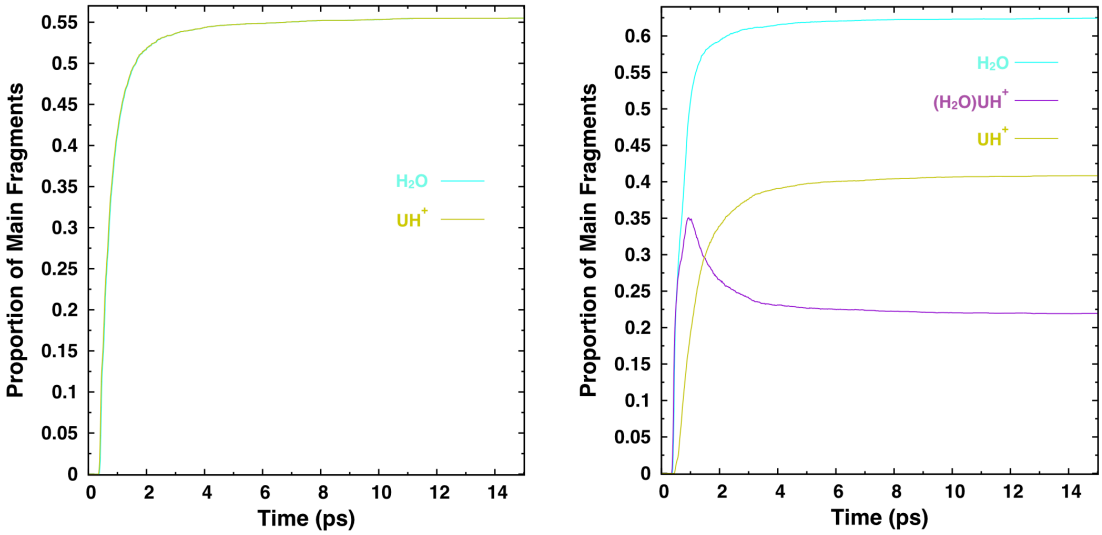

Figure 4.6: Time-dependent proportions of the main fragments obtained from the dissociation of the lowest-energy isomers of $(H_2O)_1UH^+$ (left) and $(H_2O)_2UH^+$ (right).

4.3.4 Proportion of Neutral Uracil Loss and Total Fragmentation Cross Sections for Small Clusters

In order to get more insights in the fragmentation, molecular dynamics trajectories were analysed in terms of proportion of neutral uracil loss (P_{NUL}) defined in section 4.3.2.1 and total fragmentation cross sections (σ_{frag}) defined in section 4.2.3. These two properties are also accessible from experiments. Another property extracted from the MD simulations, but not accessible from experiment, is the proportion of protonated uracil (P_{PU}) which is equal to the ratio of the number of simulations leading to a protonated uracil molecule over the number of simulations leading to a fragment containing the uracil and the excess proton. In order to correlate the outcome of the collision and the structure of the aggregate undergoing the collision, all considered low-energy isomers are characterized by there relative energies ($E_{rel.}$) and the location of the excess proton (LEP). For the latter, three distinct configurations were considered: The excess proton is bounded to the uracil molecule (noted U-H); The excess proton is

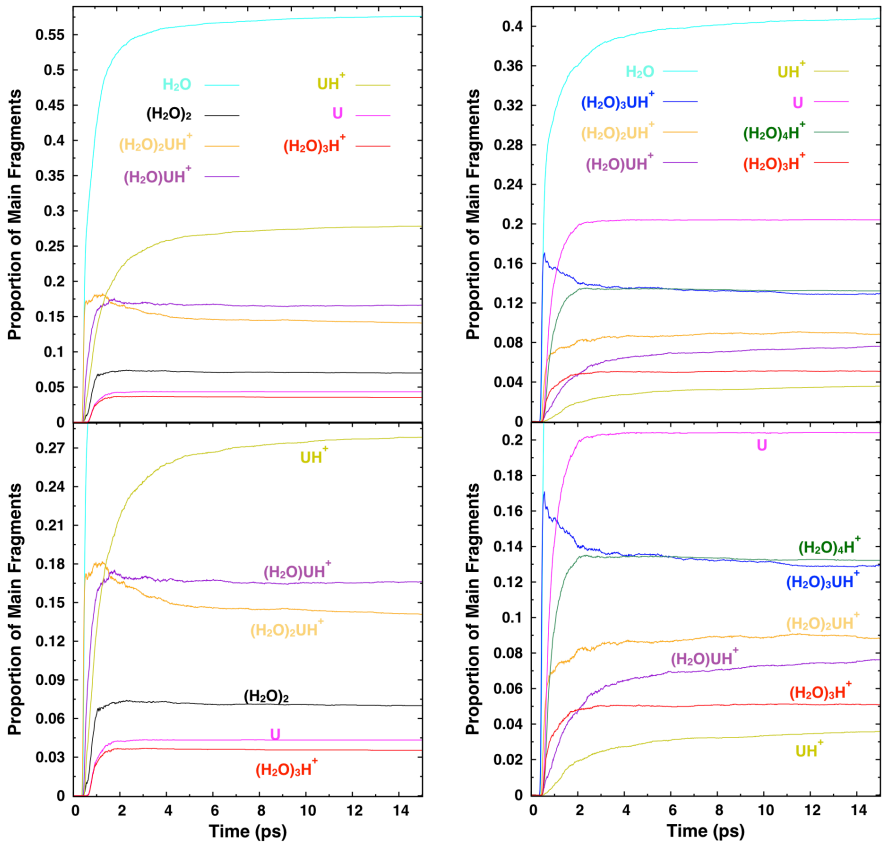

Figure 4.7: Time-dependent proportions of the main fragments obtained from the dissociation of the lowest-energy isomers of $(H_2O)_3UH^+$ (left) and $(H_2O)_4UH^+$ (right). Bottom panels correspond to a zoom over the lower proportions.

bounded to a water molecule that is adjacent to an oxygen atom of the uracil molecule (noted W-H-U); The excess proton is bounded to a water molecule that is separated by at least one other water molecule from the uracil molecule (noted W-H). All these data are gathered in Table 4.3 and will first discuss the behavior of the small species $(H_2O)_{1-7}UH^+$.

Various information can be inferred from these properties. Firstly, one observes a general increase of σ_{frag} as a function of cluster size with values ranging from 25.9 Å^2 for isomer 1b to 60.2 Å^2 for isomer 12a. Interestingly, only slight variations of σ_{frag} are observed for different isomers of the same aggregate. In contrast, P_{NUL} is much more sensitive to the nature of the considered isomers, in particular when these isomers display different LEP values. For instance, P_{NUL} is 46.6 % for 5a (W-H) while it is only 0.1 % for 5d (U-H). More interestingly, there seems to exist a strong correlation between P_{NUL} and LEP. Indeed, P_{NUL} values

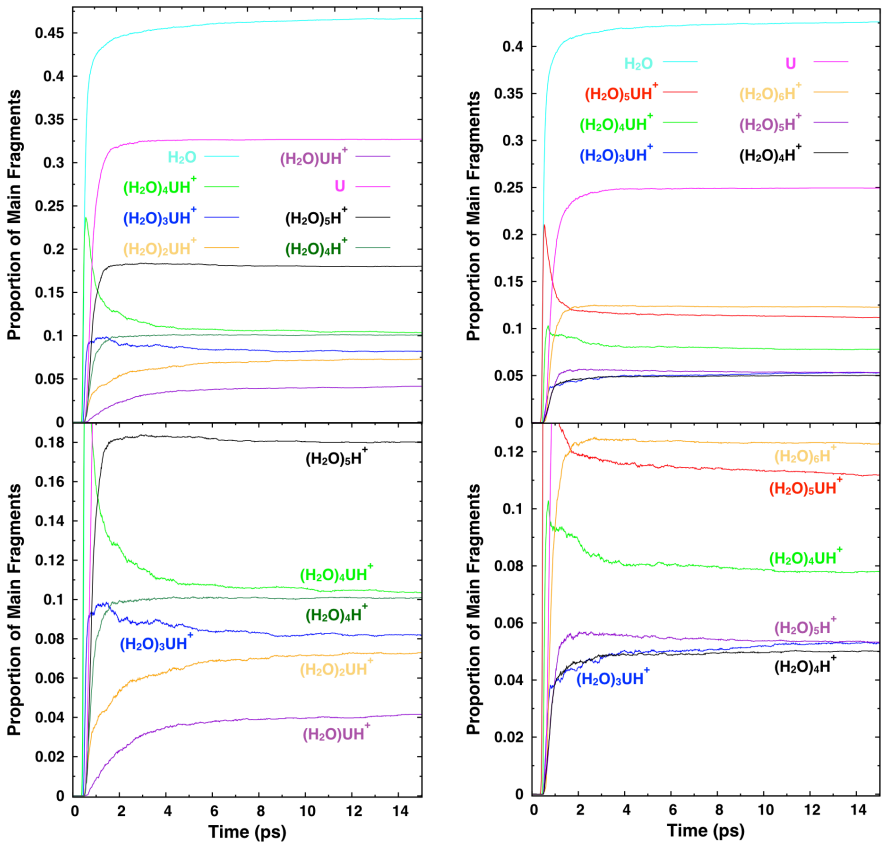

Figure 4.8: Time-dependent proportions of the main fragments obtained from the dissociation of the lowest-energy isomers of $(H_2O)_5UH^+$ (left) and $(H_2O)_6UH^+$ (right). Bottom panels correspond to a zoom over the lower proportions.

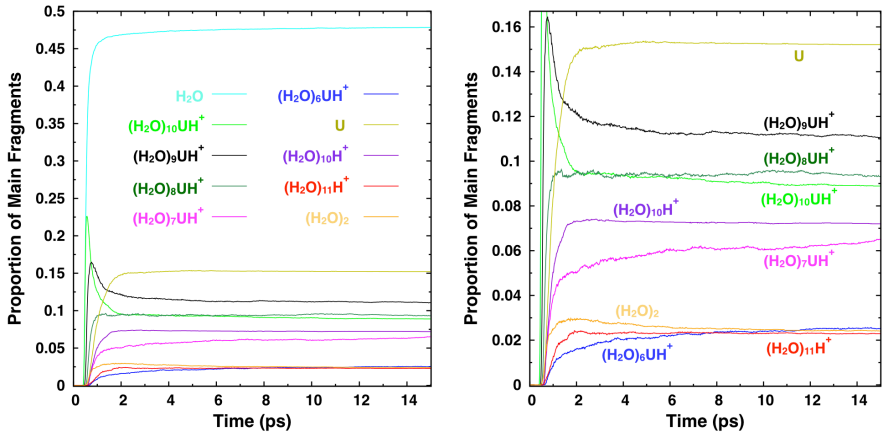

Figure 4.9: Time-dependent proportions of the main fragments obtained from the dissociation of the lowest-energy isomer of $(H_2O)_{11}UH^+$. Right panel corresponds to a zoom over the lower proportions.

Table 4.3: Relative energy $E_{rel.}$ (in kcal.mol^{-1}) at the MP2/Def2TZVP level, LEP, P_{PU} (in %), P_{NUL} (in %), σ_{frag} (in Å^2) of the considered low-energy isomers of $(H_2O)_{1-7,11,12}UH^+$ clusters. Isomers which P_{NUL} fit best to the experimental value are indicated in bold. $P_{NUL_{exp}}$ and $\sigma_{frag_{exp}}$ are the experimental values for P_{NUL} and σ_{frag}, respectively. For $(H_2O)_{12}UH^+$, experimental values were obtained for collision with Ne, whereas all other theoretical and experimental data are for collision with Ar.

Isomers	$E_{rel.}$	LEP	P_{PU}	P_{NUL}	$P_{NUL_{exp}}$	σ_{frag}	$\sigma_{frag_{exp}}$
1a	0.0	U-H	100	0.2	0.9	28.9	12.3
1b	0.7	U-H	100	0.1		25.9	
2a	0.0	U-H	100	0.0	0.4	36.3	22.8
2b	0.2	U-H	100	0.1		34.9	
3a	0.0	U-H	100	5.7	1.7	36.3	31.2
3b	0.3	U-H	100	0.0		41.9	
4a	0.0	W-H-U	98.0	29.4	2.8	40.1	43.4
4b	0.9	U-H	99.7	2.6		45.2	
5a	0.0	W-H	78.5	46.6	7.5	38.2	48.0
5b	0.3	W-H-U	89.0	28.5		38.7	
5c	2.0	W-H-U	87.8	27.1		44.6	
5d	2.4	U-H	100	0.1		47.5	
6a	0.0	W-H	44.1	39.3	18.0	45.8	54.3
6b	0.2	W-H	43.5	33.8		58.6	
6c	0.3	W-H	46.4	36.6		46.1	
6d	0.9	W-H	64.6	34.7		42.6	
6e	2.5	W-H	45.9	34.9		50.5	
6f	2.7	W-H-U	76.2	18.5		55.0	
7a	0.0	W-H	28.2	31.3	25.0	53.4	59.7
7b	0.3	W-H-U	52.4	21.4		51.7	
7c	0.3	W-H	41.3	31.1		49.5	
7d	0.8	W-H-U	40.9	23.0		54.0	
11a	0.0	W-H	4.6	28.3	11.8	52.9	63.8
11b	1.4	W-H	3.2	28.5		54.7	
11c	1.5	W-H	4.2	22.8		55.2	
11d	1.9	W-H	6.8	15.6		56.5	
11e	1.9	W-H	5.4	22.7		52.6	
11f	2.3	W-H	7.9	24.3		52.0	
12a	0.0	W-H	6.7	7.6	12.2	60.2	77.0
12b	0.6	W-H	34.0	22.4		52.2	
12c	0.7	W-H	48.7	10.8		55.4	
12d	1.3	W-H-U	5.4	9.7		54.3	
12e	1.8	W-H-U	67.5	6.0		54.2	
12f	2.4	W-H-U	55.0	17.1		54.1	

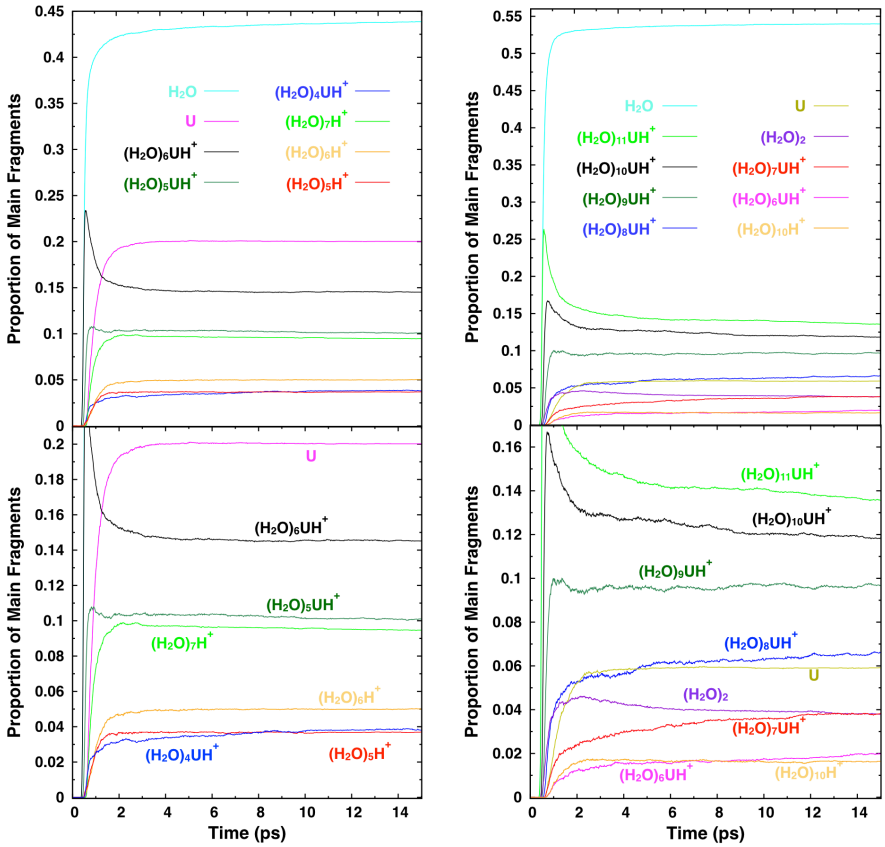

Figure 4.10: Time-dependent proportions of the main fragments obtained from the dissociation of the lowest-energy isomers of $(H_2O)_7UH^+$ (left) and $(H_2O)_{12}UH^+$ (right). Bottom panels correspond to a zoom over the lower proportions.

below 1.0 % are characterized by an excess proton initially bounded to uracil (U-H type). This suggests that when uracil is protonated, probability for deprotonation after collision is very low and thus P_{NUL} is close to 0%. P_{NUL} values between 9.7 and 29.4 % are obtained from W-H-U configurations while larger P_{NUL} values, above 31.1 %, arise from W-H configurations in clusters $(H_2O)_{5-7}UH^+$. This demonstrates that, from the excess proton point of view, the outcome of the collision is highly sensitive to the nature of the isomer undergoing the collision as hypothesised by I. Braud *et al.* [104] This important finding can be of help to determine which isomer, or set of isomers, is likely to undergo collision by comparing experimental and theoretical P_{NUL} as this is not necessarily the lowest-energy isomer as discussed below.

For $(H_2O)_{1-2}UH^+$, the theoretical and experimental P_{NUL} values, close to zero, are in good agreement regardless of the considered isomer. For $(H_2O)_3UH^+$, the experimental P_{NUL}

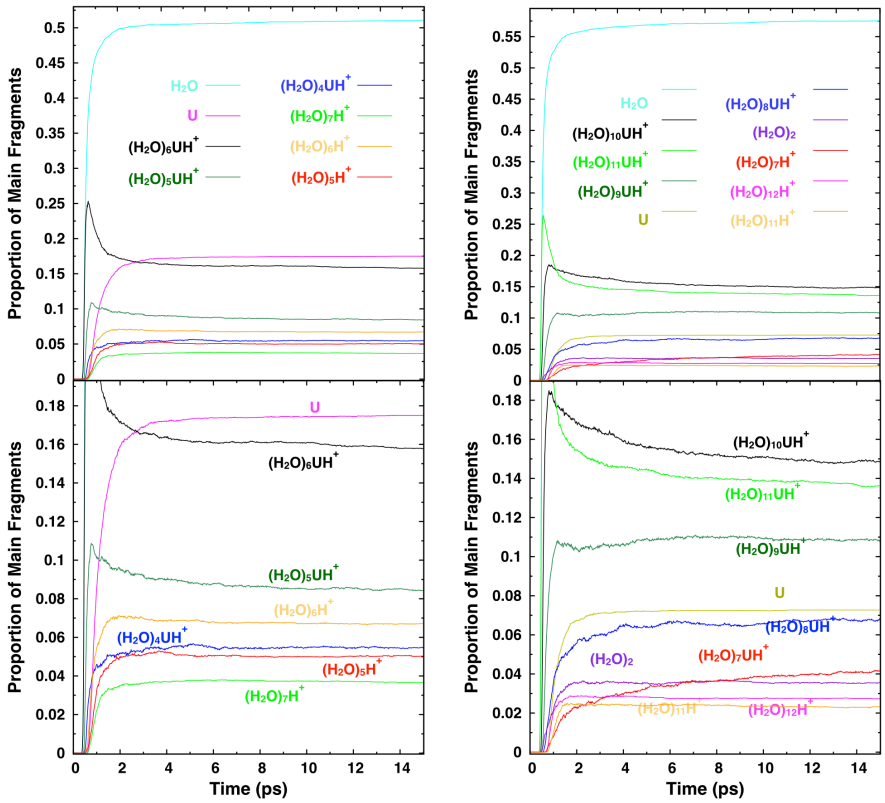

Figure 4.11: Time-dependent proportions of the main fragments obtained from the dissociation of the the third lowest-energy isomer of $(H_2O)_7UH^+$ (left) and the third lowest-energy isomer $(H_2O)_{12}UH^+$ (right). Bottom panels correspond to a zoom over the lower proportions.

is 1.7 % which is well reproduced by both isomers 3a and 3b although 3b is the one closer to the experimental value, 0.0 % against 5.7 % for 3a. This was expected as they are very close in energy, only 0.3 kcal.mol^{-1} difference, and in structure, as displayed in Figure 4.12, both being of U-H type structure. Consequently, in the experiment, each one of them could be at the origin of the experimental signal. $(H_2O)_4UH^+$ behaves differently. The two low-energy isomers, 4a and 4b, display very different P_{NUL} values, 29.4 and 2.6 %, respectively. The experimental value is 2.8 % which suggests that 4b, although slightly higher in energy by 0.9 kcal.mol^{-1}, is the isomer prevailing during the collision process. The difference in behavior can be explained by the U-H configuration of 4b, in which the excess proton is bounded to the uracil, whereas in 4a, it is bounded to a water molecule adjacent to uracil (see Figure 4.13). The case of $(H_2O)_5UH^+$ is more complex as this is the first species displaying the three types of LEP configuration among its four lowest-energy isomers as can be seen on Figure 4.13. This implies

very different P_{NUL} values: 46.6 % for 5a, 28.5 and 27.1 % for 5b and 5c, respectively, while it is only 0.1 % for 5d. The experimental P_{NUL} value for $(H_2O)_5UH^+$ is still relatively low, 7.5 %, which suggests that a U-H type structure prevails during the collision process. Although 5d is 2.4 kcal.mol^{-1} higher in energy than 5a, this isomer is thus expected to undergo the collision.

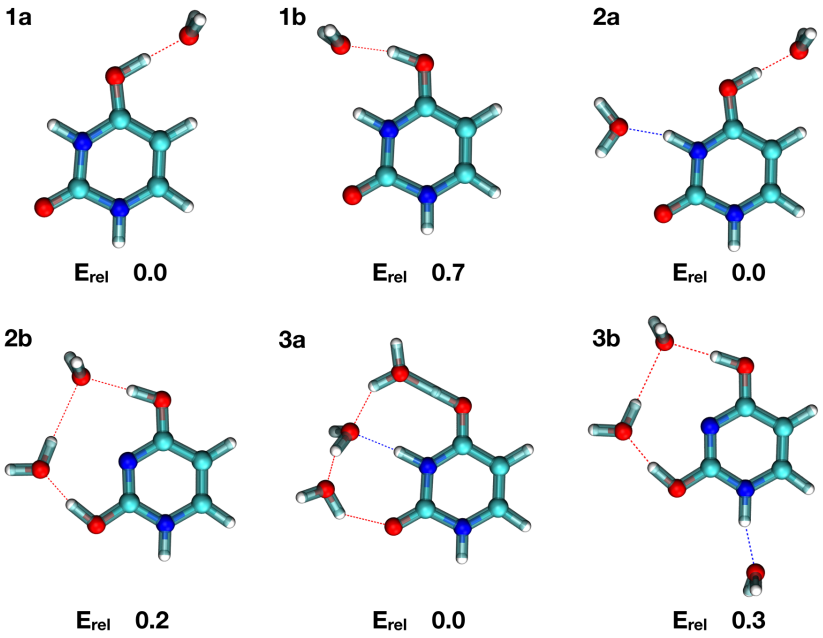

Figure 4.12: Selected low-energy configurations of $(H_2O)_{1-3}UH^+$. Relative energies at the MP2/Def2TZVP level are in kcal.mol^{-1}.

$(H_2O)_6UH^+$ and $(H_2O)_7UH^+$ are the first two aggregates for which no low-energy isomer belongs to the U-H type structure. As a consequence, in contrast to smaller species, the theoretical P_{NUL} values are all higher than 15 %. This is in line with the experimental values which display a net increase at $n = 6$. Isomers 6a, 6b, 6c, 6d, and 6e (see Figure 4.14) are all W-H type structures which leads to P_{NUL} values almost twice higher than the experimental one. Consequently, as for $(H_2O)_5UH^+$, one can assume that the isomer of $(H_2O)_6UH^+$ undergoing the collision is more likely to be a W-H-U type structure although it is higher in relative energy. Isomer 6f can be such a candidate as it displays of P_{NUL} value of 18.5% which is in agreement with the experimental value, 18.0%. Due to its increasing size, $(H_2O)_6UH^+$ displays W-H configurations with the excess proton at various distances from the recombining oxygen. Indeed, in 6a, 6c and 6d this distance is 1.774, 1.745 and 1.804 Å, while in 6b, 6e and 6f, it

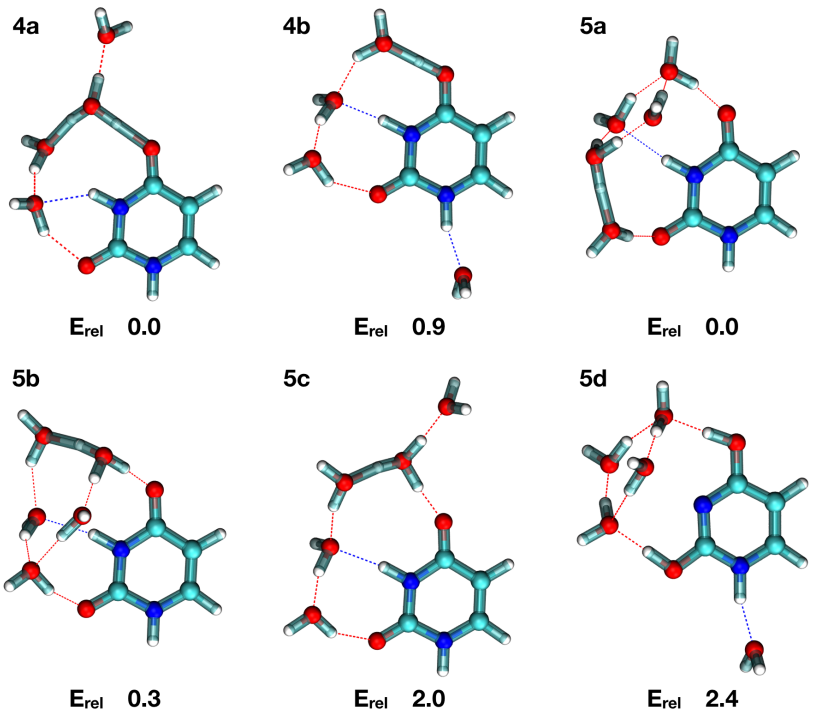

Figure 4.13: Selected low-energy configurations of $(H_2O)_{4-5}UH^+$. Relative energies at the MP2/Def2TZVP level are in kcal.mol^{-1}.

is shorter: 1.660, 1.614, and 1.494 Å, respectively. However, no net correlation is observed between this distance and the value of P_{NUL}: 39.3, 33.8, 36.6, 34.7, 34.9 and 18.5% for 6a, 6b, 6c, 6d, 6e and 6f, respectively. In particular, the behavior of 6e is striking. It has almost the same relative energy as 6f and they are structurally similar (see Figure 4.14) but display different P_{NUL} values. This suggests that, for n larger than 5, the ability of the water molecule network to stabilise the excess proton, *i.e* to promote or prevent its diffusion toward the uracil molecule, starts to be competitive with the configuration type of the isomer. In 6e, the excess proton is in a configuration close to the Zundel ion which may explain its high P_{NUL} value as compared to 6f. For $(H_2O)_7UH^+$, a W-U-H type configuration is also expected to fit best the experimental result. And indeed 7d, a W-H-U type structure, which is only 0.8 kcal.mol^{-1} above the lowest-energy isomer (see Figure 4.15), has a P_{NUL} value of 22.9 % as compared to 25.0 % experimentally. Isomers 7a and 7c have a W-H configuration and their P_{NUL} values (31.3 and 31.1 %, respectively) are higher than the ones of 7b and 7d which have a W-H-U configuration.

Finally, it is worth noting that even when the excess proton is initially bounded to a water molecule, *i.e.* when a W-H type structure is considered, the maximum P_{NUL} that has been obtained is only 46.6 %. This demonstrates that for small aggregates such as $(H_2O)_{5-7}UH^+$ ($(H_2O)_{1-4}UH^+$ do not display low-energy W-H type structures), dissociation mainly lead to protonated uracil containing fragments. This is in line with the experimental results. Analysis of P_{PU} values also show that uracil is protonated in a significant amount of these protonated uracil containing fragments. P_{PU} has a clear tendency to decrease with cluster size, but can be quite high even for W-H type structures, for instance 5a, 6d and 7c in Table 4.3. This demonstrates that upon collision, the excess proton is likely to transfer to uracil on a rather short time scale.

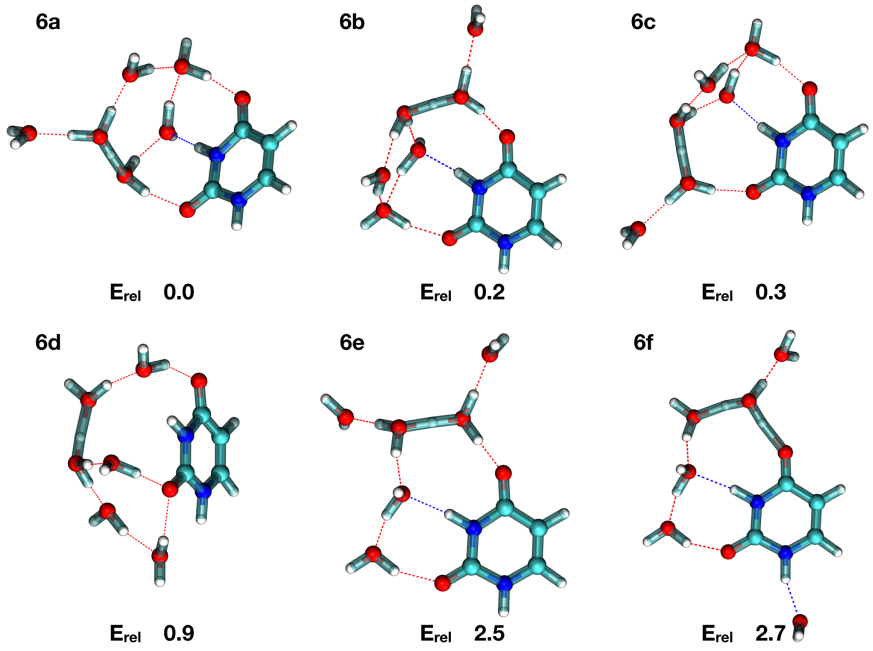

Figure 4.14: Selected low-energy configurations of $(H_2O)_6UH^+$. Relative energies at the MP2/Def2TZVP level are in kcal.mol^{-1}.

The clusters discussed above are characterized by complex potential energy surfaces characterized by several low-energy isomers, with relative energies that can be lower than 1 kcal.mol^{-1}, and which get more complex as the number of water molecules increases. Consequently, the exact energetic ordering between the low-energy isomers can not be precisely known as this is below chemical accuracy and thus can not claim here to have found the lowest-energy structure of each aggregate, or the isomer undergoing the collision. Nevertheless, what I show is that

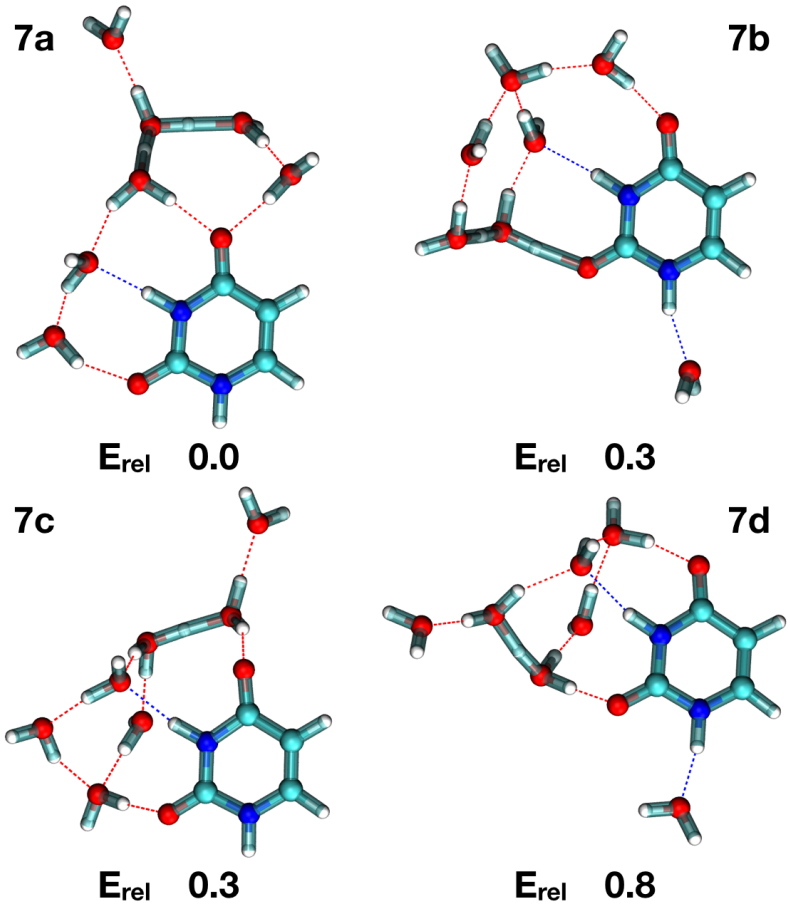

Figure 4.15: Selected low-energy configurations of $(H_2O)_7UH^+$. Relative energies at the MP2/Def2TZVP level are in kcal.mol^{-1}.

P_{NUL} is mainly determined by the initial position of the proton in the isomer undergoing the collision. Consequently, for the collision energy and the range of cluster size I have considered, the structure of the aggregate undergoing the collision plays a key role in determining the dissociation process and collision outcomes much more than energetics. This is consistent with the analysis of the time-dependent proportion of fragments which suggests a direct dissociation mechanism. This is further highlighted on Figure 4.16, which presents the experimental P_{NUL} for collision with Ar and Ne, respectively as a function of n and the corresponding theoretical values obtained from the lowest-energy isomers as well as from the isomers for which P_{NUL} matches best to the experimental data. As can be seen, a very good agreement can be obtained with the experimental data by considering a specific set of isomers. Interestingly, if a similar plot is drawn for σ_{frag} considering the same isomers (see Figure 4.17), a good agreement with

the experimental data and much better than σ_{geo} (calculated from formula 3.4)is also obtained with the two sets of isomers which confirms the weaker dependence upon isomer of σ_{frag}.

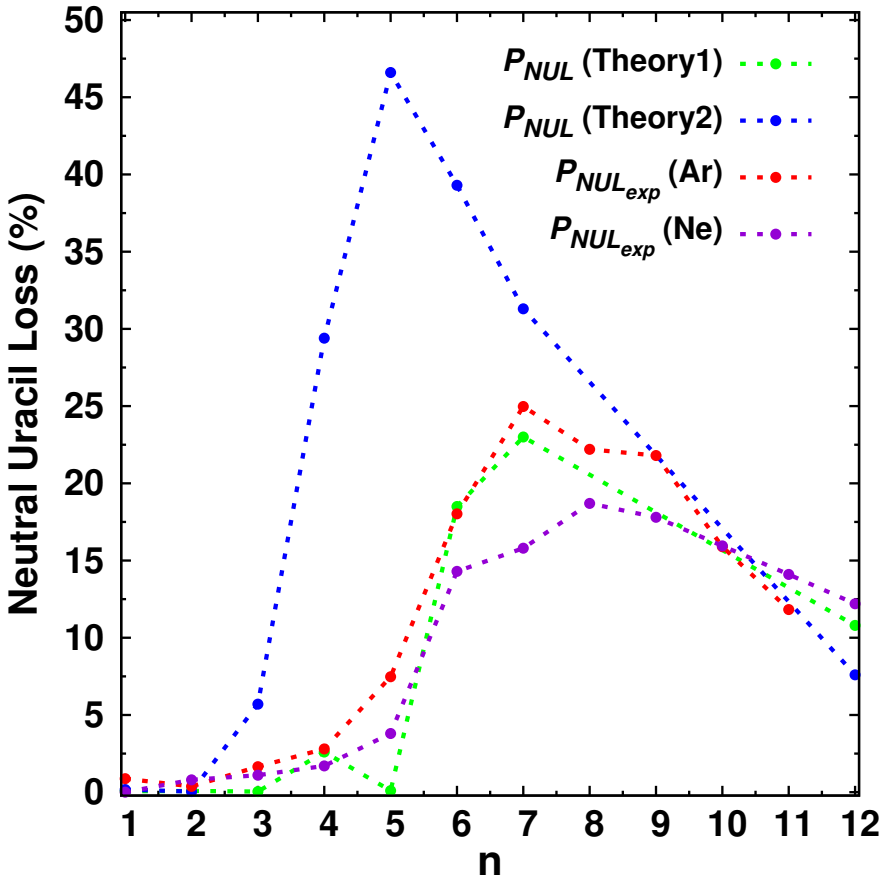

Figure 4.16: Theoretical (green and blue lines) and experimental (red line) P_{NUL} values for the $(H_2O)_{1-7,11,12}UH^+$ clusters. Theory 1 (green line) is obtained from the isomers which P_{NUL} matches best to the experimental data while Theory 2 (blue line) is obtained from lowest-energy isomers.

4.3.5 Behaviour at Larger Sizes, the Cases of $(H_2O)_{11,12}UH^+$

In the experiments conducted by I. Braud *et al.*,[104] P_{NUL} starts to decrease at n=8. This decrease is not consistent with the above argument of a direct dissociation mechanism and larger species more likely characterized by W-H and W-H-U type structures. This apparent discrepancy motivated us to extend the present study to a larger cluster, namely $(H_2O)_{11,12}UH^+$. For $(H_2O)_{12}UH^+$, the only available experimental data is for collisions with Ne instead of Ar, al-

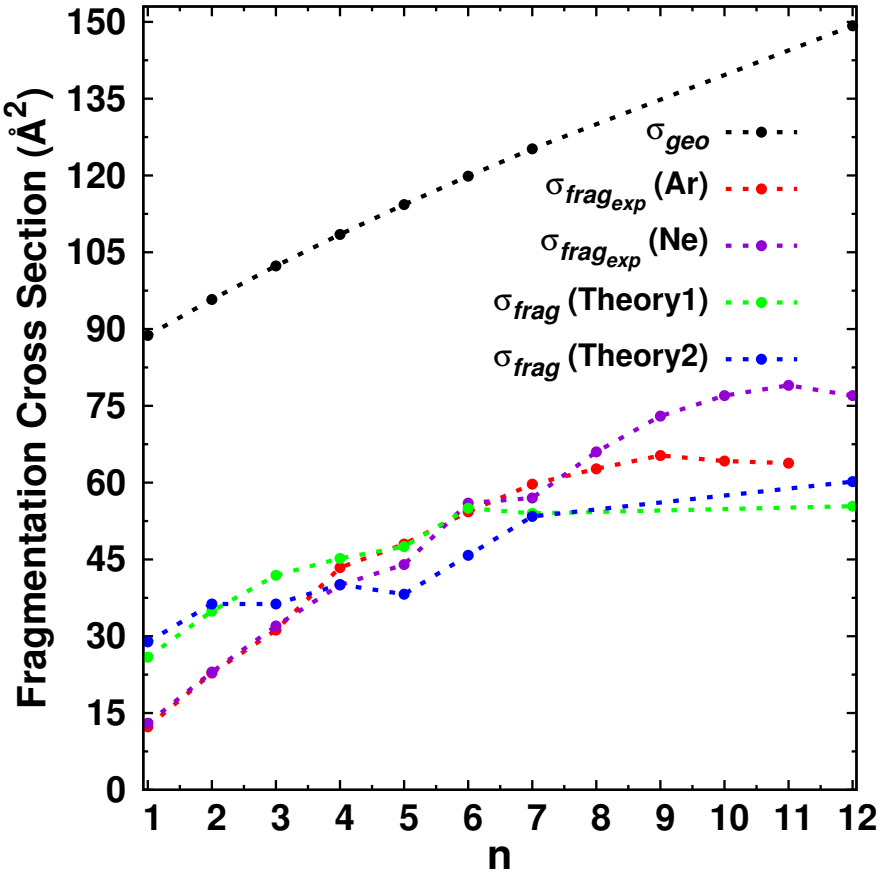

Figure 4.17: Theoretical (green and blue lines) and experimental (red line) σ_{frag} values for the $(H_2O)_{1-7,11,12}UH^+$ clusters. Theory 1 (green line) is obtained from the isomers which P_{NUL} matches best to the experimental data while Theory 2 (blue line) is obtained from lowest-energy isomers.

though for the same center of mass collision energy. As shown in Figure 4.16, experimental P_{NUL} values for Ne or Ar, although not equal, display similar trend. In the following, I thus discuss the experimental data of $(H_2O)_{12}UH^+$ colliding with Ne. For cluster $(H_2O)_{1-7,11}UH^+$, keep discussing the experimental data from colliding with Ar.

The behaviour for $(H_2O)_{11}UH^+$ and $(H_2O)_{12}UH^+$ is rather different when looking at detailed properties. Indeed, for $(H_2O)_{11}UH^+$, P_{NUL} values for isomers 11a, 11b, 11c, 11e, and 11f are very similar as they range from 22.7 to 29.8 %. For 11d, P_{NUL} equal 15.6 % which fits best to the experiment. These P_{NUL} values are lower than those of $(H_2O)_6UH^+$, as observed experimentally, and in the same range as $(H_2O)_7UH^+$. All isomers display a W-H type configuration as seen in Figure 4.18. P_{PU} is very small for all $(H_2O)_{11}UH^+$ isomers which shows

that on the time scale of the simulations, protonation of uracil hardly occurs.

For $(H_2O)_{12}UH^+$, 12c isomer, which has a W-H type configuration (see Figure 4.19), has a P_{NUL} value which fits best to the experiment, 10.8 % against 12.2 %, while isomer 12a, also a W-H type configuration (see Figure 4.19), has a P_{NUL} value equal to 7.6 %. Overall, P_{NUL} values calculated for $(H_2O)_{12}UH^+$ isomers are lower than those of $(H_2O)_6UH^+$ and $(H_2O)_7UH^+$, which is in line with the experiment. The main difference with the $(H_2O)_{1-7}UH^+$ aggregates is that no clear relation exist between the P_{NUL} value and the initial localisation of the excess proton. Indeed, 12a, 12b and 12c are all W-H type configurations but with P_{NUL} values ranging from 7.6 to 22.4 %. The same is observed for 12d, 12e and 12f although they are all W-H-U type configurations. Similarly, no difference in behaviour is obtained between W-H and W-H-U type configurations. This can be explained by assuming that the dissociation mechanism in $(H_2O)_{12}UH^+$ involves some amount of structural rearrangement that softens the impact of the isomer undergoing the collision. Indeed, as $(H_2O)_{12}UH^+$ has more degrees of freedom, it can more easily accommodate the kinetic energy transferred by the colliding atom prior to dissociation which thus takes place on a longer time scale. This excess of internal energy thus fosters structural rearrangements, in particular proton transfers toward the uracil, explaining the smaller P_{NUL} value for $(H_2O)_{12}UH^+$. This is in full agreement with the conclusions obtained in section 4.3.3 from Figures 4.9, 4.10 and 4.11. To further support this conclusion, I conducted 200 MD simulations in the micro-canonical ensemble in which the whole kinetic energy of Ar was randomly distributed in all the vibrational modes of isomer 12c by drawing initial velocities in a 1185 K Boltzmann distribution. Among them, 166 simulations display dissociation with one or two water molecules dissociating from the main cluster. No neutral uracil loss is observed. To conclude, although the present simulations are too short to assert that $(H_2O)_{12}UH^+$ undergoes a statistical dissociation mechanism, they clearly show that a direct mechanism is not sufficient to account for the theoretical and experimental results. Consequently, structural rearrangements are very likely to occur prior to dissociation and the experimental results for P_{NUL} and σ_{frag} values can not result from a single $(H_2O)_{12}UH^+$ isomer. In contrast, similarities in both P_{NUL} and P_{PU} values for all considered $(H_2O)_{11}UH^+$ isomers, as well as P_{NUL} values close to $(H_2O)_7UH^+$ ones, do not evidence structural rearrangements in this species although they could be present.

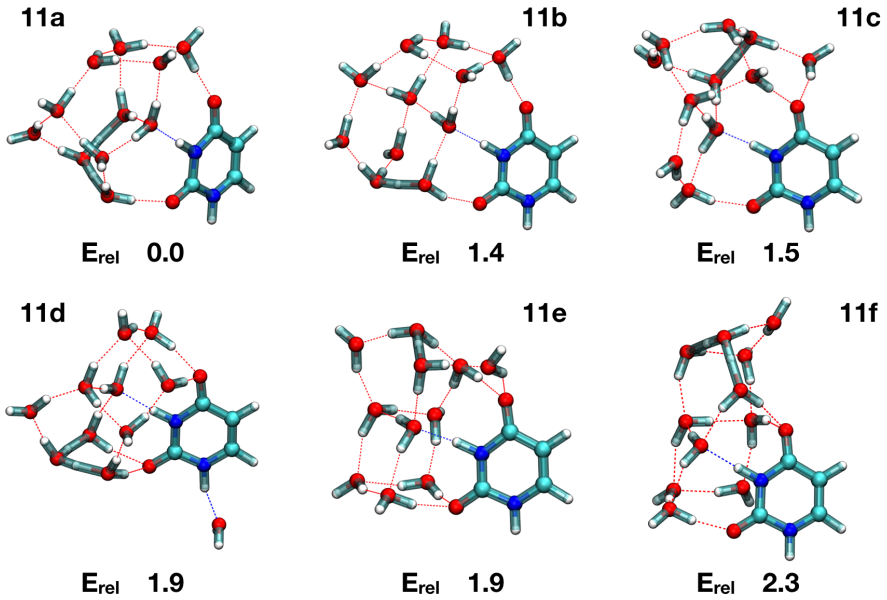

Figure 4.18: Selected low-energy configurations of $(H_2O)_{11}UH^+$. Relative energies at the MP2/Def2TZVP level are in kcal.mol^{-1}.

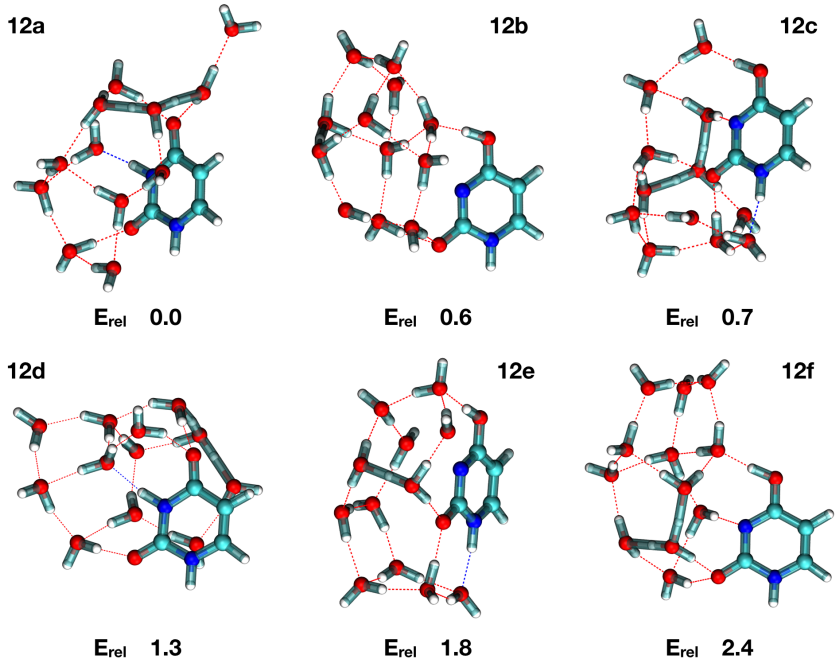

Figure 4.19: Selected low-energy configurations of $(H_2O)_{12}UH^+$. Relative energies at the MP2/Def2TZVP level are in kcal.mol^{-1}.

4.3.6 Mass Spectra of Fragments with Excess Proton

In this section, in order to analyse collision products in more details, the branching ratios of the different fragments containing the excess proton were extracted from the collision simulations of clusters $(H_2O)_{1-7,11,12}UH^+$ and compared with the experimental ones shaped as mass spectra.[104] For each cluster size, only simulations corresponding to the isomer which P_{NUL} value fits best to the experiment were considered (1a, 2b, 3b, 4b, 5d, 6f, 7d, 11d, 12c). The results are presented in Figures 4.20, 4.21 and 4.22. For cluster $(H_2O)_{12}UH^+$, there is no experimental data for collision with argon. For $(H_2O)_{12}UH^+$, experimental results were obtained for collision with neon. From the experimental results for argon and neon for 1a, 2b, 3b, 4b, 5d, 6f, 7d, and 11d, it shows the branch ratios for collision with argon and neon are close and have the same trend. So it should be reasonable to compare the simulated branch ratios of 12c with the ones of experimental data from the collision of $(H_2O)_{12}UH^+$ with argon.

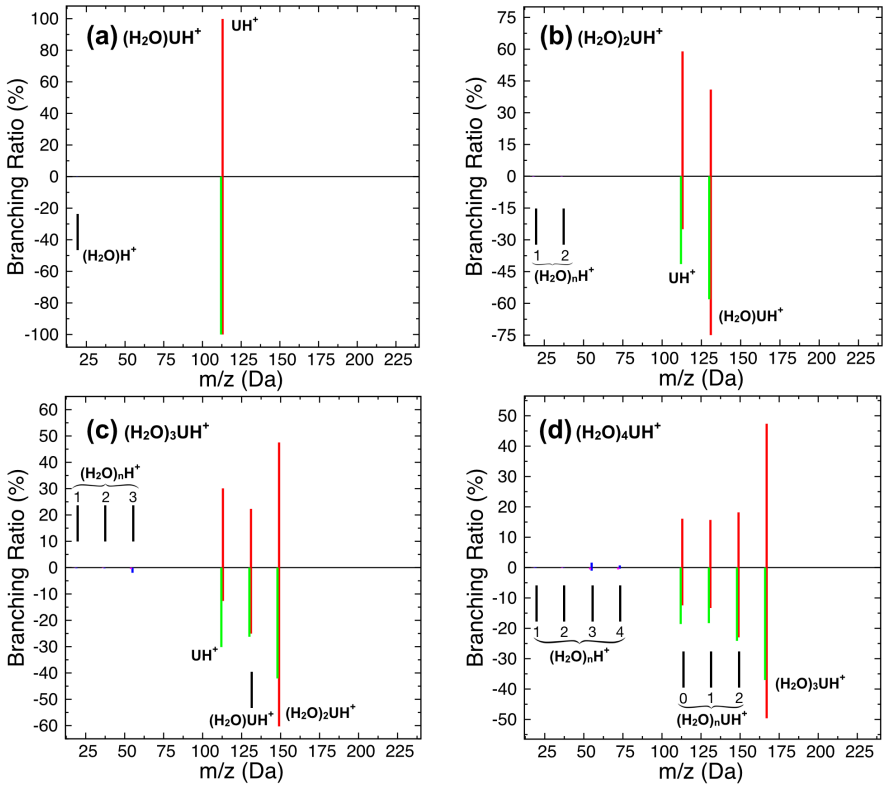

Figure 4.20: Simulated mass spectra (positive area) of the charged fragments after 15 ps simulation time (fragments $(H_2O)_nH^+$ in red and $(H_2O)_nUH^+$ in blue for argon; $(H_2O)_nH^+$ in pink and $(H_2O)_nUH^+$ in green for neon) from isomers (a) 1a, (b) 2b, (c) 3b, (d) 4b. The counterparts in experiment are plotted (negative area).

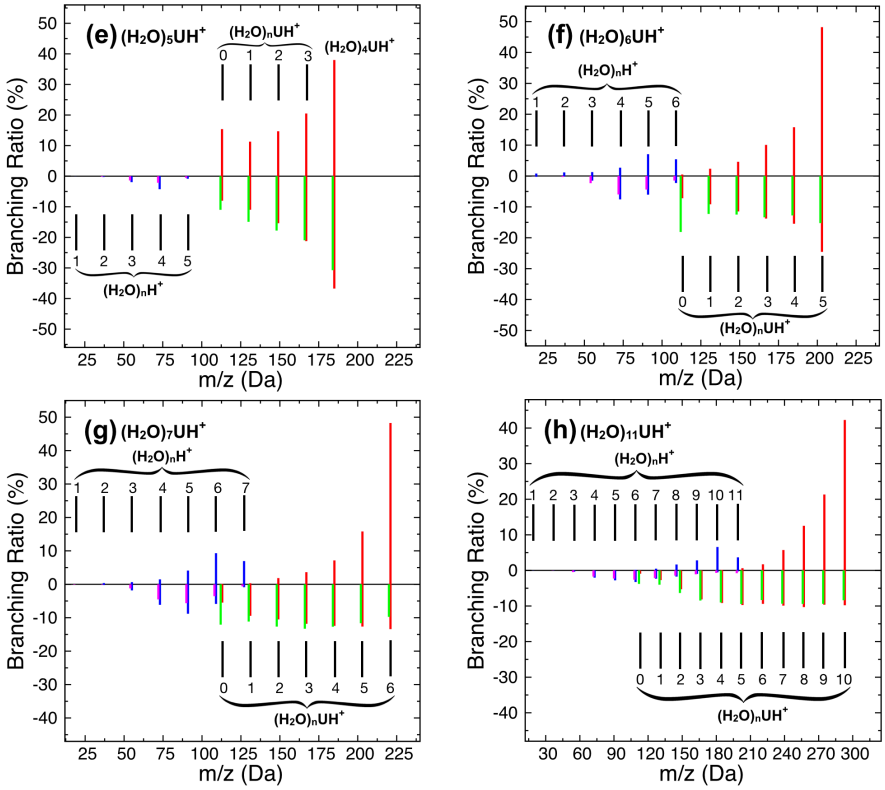

Figure 4.21: Simulated mass spectra (positive area) of the charged fragments after 15 ps simulation time (fragments $(H_2O)_nH^+$ in red and $(H_2O)_nUH^+$ in blue) from isomers (e) 5d, (f) 6f, (g) 7d, and (h) 11d. The counterparts in experiment are plotted (negative area).

Overall, the experimental and theoretical spectra present the same general trends: (i) The mass spectra present a broad distribution of sizes, without prominence of a particular peak; (ii) All the spectra are dominated by the heaviest protonated uracil containing fragment (loss of a single water molecule) with the exception of the simulated mass spectrum for 2b; (iii) Fragments containing protonated uracil prevail over pure protonated water fragments, as already observed from the P_{NUL} values provided in Table 4.3; (iv) Pure protonated water fragments only appear for the largest cluster sizes. Indeed, although very minor contributions are observed in both the simulated and experimental spectra for parent clusters with n=3-5, significant contributions of these species only appear when the parent cluster contains at least 6 water molecules.

A more detailed discussion of the simulated and experimental mass spectra will be made as follows. For $(H_2O)_2UH^+$, fragments $(H_2O)UH^+$ and UH^+ are observed in both experiment and theory although their relative ratio is different. For $(H_2O)_3UH^+$, the simulated and exper-

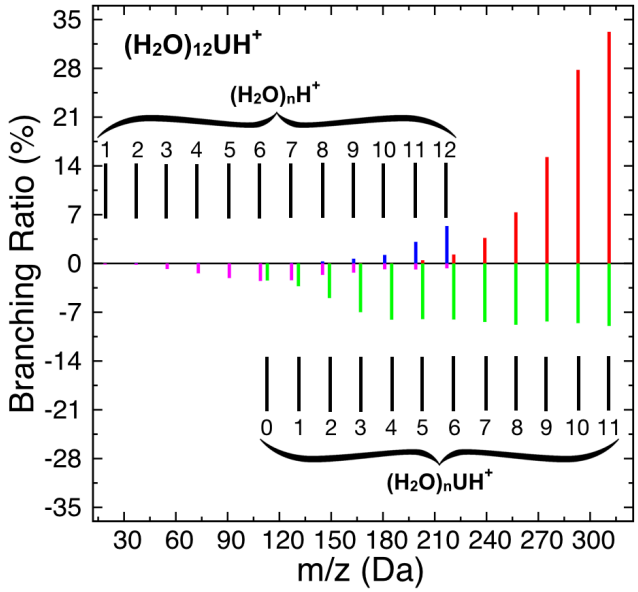

Figure 4.22: Simulated mass spectra (positive area) of the charged fragments after 15 ps simulation time (fragments $(H_2O)_nH^+$ in red and $(H_2O)_nUH^+$ in blue) from isomers 12c. The counterparts in experiment obtained for collision with neon are plotted in negative area $(H_2O)_nH^+$ in pink and $(H_2O)_nUH^+$ in green).

imental spectra agree quite well with a dominant peak for $(H_2O)_2UH^+$. For $(H_2O)_4UH^+$, in both experimental and theoretical spectra, the peak intensity of the fragments containing protonated uracil increases with the number of water molecules. For $(H_2O)_5UH^+$ and $(H_2O)_6UH^+$, this is also the case except for the UH+ fragment which is overestimated when compared to the experimental result in Figure 4.21 (e). For $(H_2O)_{7,11,12}UH^+$, the intensities for the heaviest fragments are overestimated.

From Figures 4.20, 4.21 and 4.22, it is clear that the smaller the cluster (except Figure 4.20 (b)) is, the better the agreement between the simulated and experimental branching ratios is. This trend indicates that for small clusters, *i.e.* for $n = 1-6$, short simulation time is enough to capture the full dissociation pattern, in other words, the dissociation mechanism is direct with no noticeable contribution of long term evolution. However, for larger clusters, starting at n=7, owing to the larger number of degrees of freedom, short simulation time does not capture the full dissociation pattern, *i.e.* long term statistical dissociation is more likely to play a noticeable role. This is fully in line with the conclusions obtained in section 4.3.5 for $(H_2O)_{12}UH^+$ and refine the interpretation given in section 4.3.4 for $(H_2O)_7UH^+$. This also shows that although the data presented in section 4.3.5 for $(H_2O)_{11}UH^+$ do no evidence the

where $E_{Ar}^{k,0}$ is the initial argon kinetic energy whereas E_{Ar}^{k} and E_{td}^{k} correspond to kinetic energies at the end of the MD simulation. In the case of dissociated dimers at the end of the simulations, the energy deposited in the rovibrational modes of the monomers can be deduced as:

$$\Delta E_{int}^{Py^1+Py^2} = E_{Ar}^{k,0} - E_{Ar}^{k} - E_{td}^{k} - E_{Re}^{k} \tag{4.11}$$

4.4.3 Simulation of the Experimental TOFMS

The experimental TOFMS are reproduced by simulating the ion trajectories through the experimental setup in the presence of the electric fields. These are calculated by solving numerically the Laplace equation. Equations of motion are integrated using the fourth order Runge-Kutta method with adaptive step size. The occurrence of collision or dissociation is decided at each time step of the ion trajectory based on the collision and dissociation probabilities.

In the work of S. Zamith *et* al., [65] the energy transfer was treated upon collision by using the Line of Center model (LOC) [484]. In the LOC model, the transferred energy is the kinetic energy along the line of centers. Evaporation rates were then estimated using PST, in which only statistical dissociation to be possible after energy deposition in the cluster by collision was conside. Although this approach, which will be referred to as PST in the following, has been proved to be able to satisfactorily reproduce CID cross section experiments,[65] it fails to reproduce in details the shape and position of the fragment peaks in the TOFMS, as will be shown in section 4.4.4.1.

In order to better reproduce the position and peak shapes, the MD and PST methods were combined. The outputs of the MD simulations were used to treat the collisions in the ion trajectories. At each time step the probability for a collision is evaluated. The principle of MD+PST is displayed in Figure 4.23.

One MD trajectory (with proper weighting of the b values) was randomly picked from all outputs of MD simulations at a given collision energy. Then two cases have to be considered. First, if the dissociation occurred during the picked MD calculation (short time dissociation), then the MD final velocities of the fragments are used to further calculate the ion trajectories. On the other hand, if the pyrene dimer is still intact at the end of the picked MD calculation, then the dimer velocity is updated and use the collision energy transfer $\Delta E_{int}^{Py_2}$ deduced from the MD calculation to increase the internal energy of the cluster. The dissociation rate resulting from this new internal energy is then evaluated using PST. In the latter case, if dissociation occurs (long time dissociation), the relative velocities of the fragment are evaluated using the PST

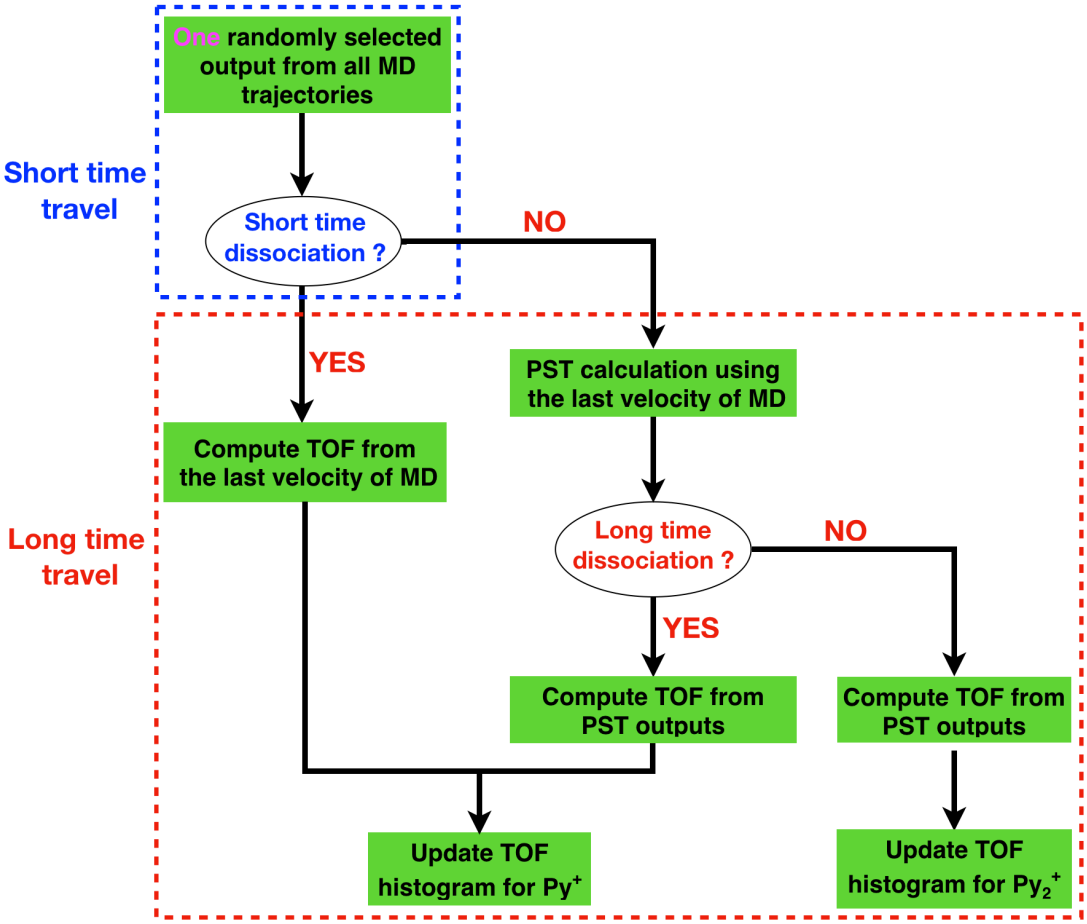

Figure 4.23: Principle of MD+PST.

outcome. The whole process of MD+PST is performed many times for different trajectories to ensure the reliability of the final obtained data. For each time, the TOFMS of Py^+ or Py_2^+ is updated.

Here I emphasize that, due to the short time scale of the MD calculations (3 ps), only direct dissociation can be captured by the MD simulations. Therefore, one has to evaluate the probability of dissociation at longer time scales after the energy deposition by collision. This is done here by considering that at longer time scales, dissociation occurs statistically and is treated by using PST.

4.4.4 Results and Discussion

In the following, I will discuss the dissociation at short, experimental and infinite timescales. The first two ones correspond to dissociation occurring during the MD simulation only or with the MD+PST model. The dissociation at infinite time accounts for all MD trajectories where the amount of energy transferred to the internal dimer rovibrational modes $\Delta E_{int}^{Py_2}$ is larger than the dissociation energy of 1.08 eV (value from references [65, 457]). It can be regarded as the dissociation occurring after an infinite time neglecting any cooling processes, such as thermal collisions or photon emissions.

4.4.4.1 TOFMS Comparison

An example of TOFMS is given in Figure 4.24. Figure 4.24(a) is centered around the intact parent mass (Py_2^+) whereas in (b) is displayed the region around the fragment peak (Py^+).

In Figure 4.24(a) are displayed three curves corresponding to the experimental one and the results of the two simulations (PST and MD+PST) for the parent ion. One can see that the peak shape and position are properly reproduced using the simulations; therefore, the essential of the ion propagation is captured by the simulations. Although some of the detected parent ions have undergone a collision without dissociation, no difference is seen in the parent peak since the collision rate is kept very small.

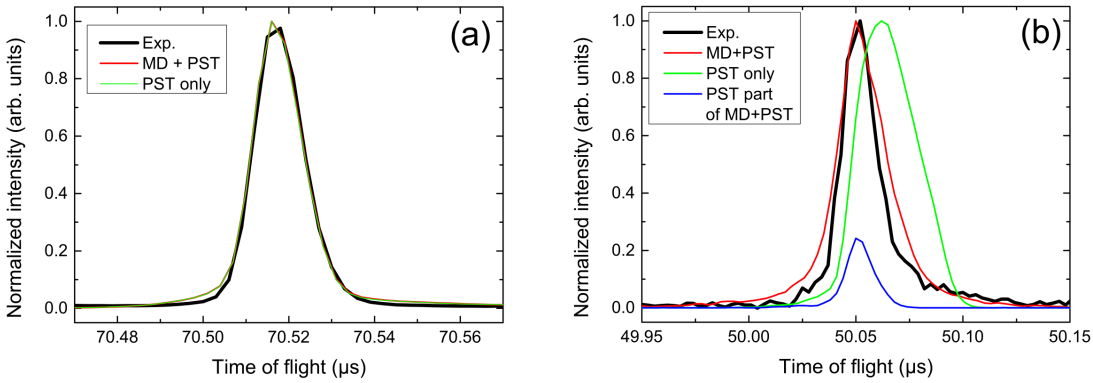

Figure 4.24: Normalized time of flight mass spectra of the parent pyrene dimer cation (a), and the pyrene fragment Py^+ (b) resulting from the collision of Py_2^+ with argon at a center of mass collision energy of 17.5 eV. The black line is for the experimental result whereas red and green curves are the MD+PST and PST model results. The blue curve is the PST subcontribution of the MD+PST model.

In Figure 4.24(b), the experimental result is compared to the PST and MD+PST simulations. Clearly, the PST based simulation fails to reproduce both the position and the shape of the peak. On the other hand, a much better agreement is found when using the output of the MD+PST simulations. This agreement is a good indication that this scheme captures the essence of the pyrene dimer cation dissociation induced by argon collisions at this collision energy. Actually, in this scheme, the largest contribution to the TOFMS results from dimers dissociating on short timescales, *i.e.* during the MD simulation. The remaining contribution, *i.e.* resulting from dimers dissociating at longer timescales and computed from the second step PST calculation, is minor and represented in blue in Figure 4.24(b).

4.4.4.2 Molecular Dynamics Analysis

Description of selected trajectories

A first qualitative description of the collision processes can be obtained from the analysis of some arbitrarily selected MD trajectories. Figure 4.25 (top and bottom) reports some snapshots extracted from two trajectories with the same collision energy (17.5 eV) and impact parameter (3.5 Å). Only the top one leads to the Py_2^+ dissociation. During the results collection, the final snapshot for each trajectory is extracted and the dimer is dissociated is considered if the distance between the two monomers molecular mass centers is larger than 10 Å. Figures 4.25-1/1* represent the system after its preliminary thermalization, when the argon atom introduced in the simulation with its initial velocity. Figures 4.25-2/2* and 3/3* represent the beginning and end of the collision. From these points, the two trajectories show different behaviors. For the top trajectory in Figure 4.25, snapshot 5 corresponds to the step where the two pyrene monomers start to go away from each other. After this, the intermolecular distance continues to increase further in snapshot 6. For the bottom trajectory in Figure 4.25, Figures 4.25-5* and 6* correspond to the middle and ending snapshots of the simulation, respectively. The snapshots 4*, 5* and 6* show the process of energy redistribution within the clusters. In particular, the soft modes associated to global deformation of the molecular planes appear to be excited.

From these two particular cases, it can be seen that the evolution of the trajectory either toward a dissociation or a redistribution of the transferred energy strongly depends on the process of energy transfer during the collision. In the top trajectory in Figure 4.25, the argon atom is pushing the two monomers far away from each other, *i.e.* the transferred energy is mostly localised in an intermolecular dissociative mode. On the opposite, in the bottom trajectory in

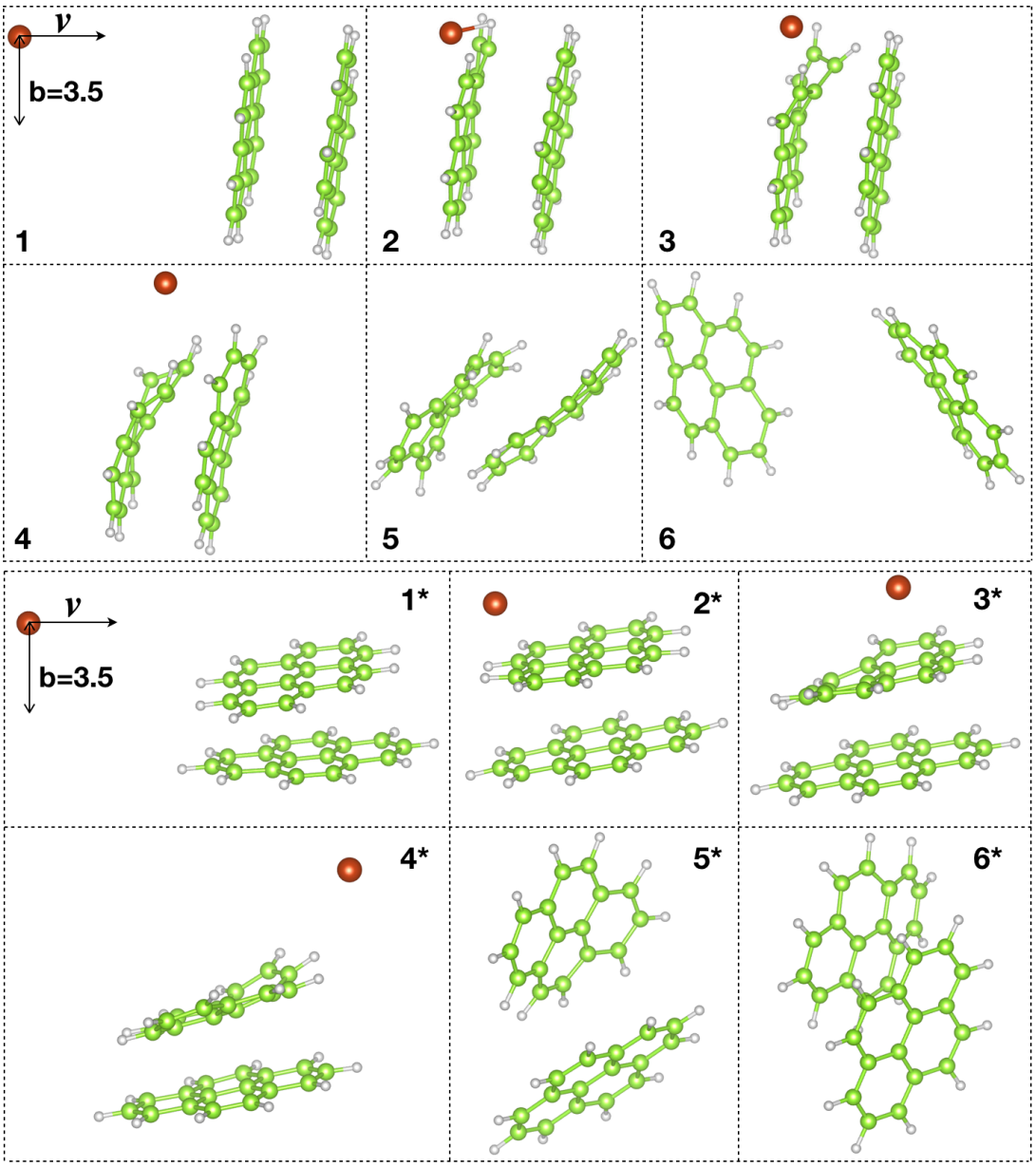

Figure 4.25: Snapshots for two different molecular dynamics trajectories. Top and bottom: trajectories with impact parameter of 3.5 Å and a collision energy of 17.5 eV, leading to dissociation and non-dissociation (top and bottom, respectively).

Figure 4.25, the collision mostly involves an intramolecular soft vibrational mode. The transferred energy is then redistributed over all the other modes. The statistical distribution of this energy is then hardly favorable to the dissociation due to the large number of intramolecular modes (72 per pyrene) with respect to the 6 intermolecular modes, only 3 of them (1 breathing and 2 parallel displaced modes) being dissociative modes.

The amount of transferred energy is also a major ingredient for the fate of the cluster. Depending on the details of the collision such as impact parameter or cluster orientation, very different amounts of energy can be transferred. This is illustrated in Figure 4.26 where the distribution of transferred energy $\Delta E_{int}^{Py_2}$ restricted to trajectories that would dissociate after infinite time, is plotted for simulations at the experimental collision energy of 17.5 eV. This distribution could hardly be guessed without a dynamical description of the collision at the atomic level. Indeed, a simpler model such as the LOC model (used in the pure PST approach) would lead to a constant distribution between the binding energy and the maximum collision energy as shown in Figure 4.26. In the distribution resulting from MD simulations, lower transferred energies are favored with respect to the distribution extracted from the LOC model. All these effects are intrinsically taken into account in the MD simulations on the opposite to the pure PST model, explaining the better agreement of the MD+PST scheme with the experimental results.

Finally, I note that the pyrene monomers remained intact (no fragmentation) up to collision energies of 25 eV. The snapshots of a fragmentation trajectory at collision energy of 27.5 eV are shown in Figure 4.27. It can be seen that the pyrene molecule impacted by the argon undergoes an opening of an aromatic cycle and the loss of two hydrogen atoms, leaving as a H_2 molecule. As the study of monomer's fragmentation is beyond the scope of the present paper, I will focus on trajectories with collision energies below this fragmentation threshold energy in the following.

Dissociation cross section

The opacity curves are presented in Figure 4.28 for various collision energies. At low impact parameters, the dissociation is very efficient even at low collision energy. At the lowest collision energy of 2.5 eV, the opacity curve presents a smooth decrease from 2 to 5 Å, whereas for collision energies larger than 10 eV, all curves are very similar. These high energy curves show high dissociation probability below 3.5 Å, reach 50% at about 4.5 Å and drop to zero for values larger than 5.5 Å. These values can be compared to the van der Waals radius of argon (1.88 Å) plus half of (i) the distance between the two molecules centers of masses (3.04 Å),

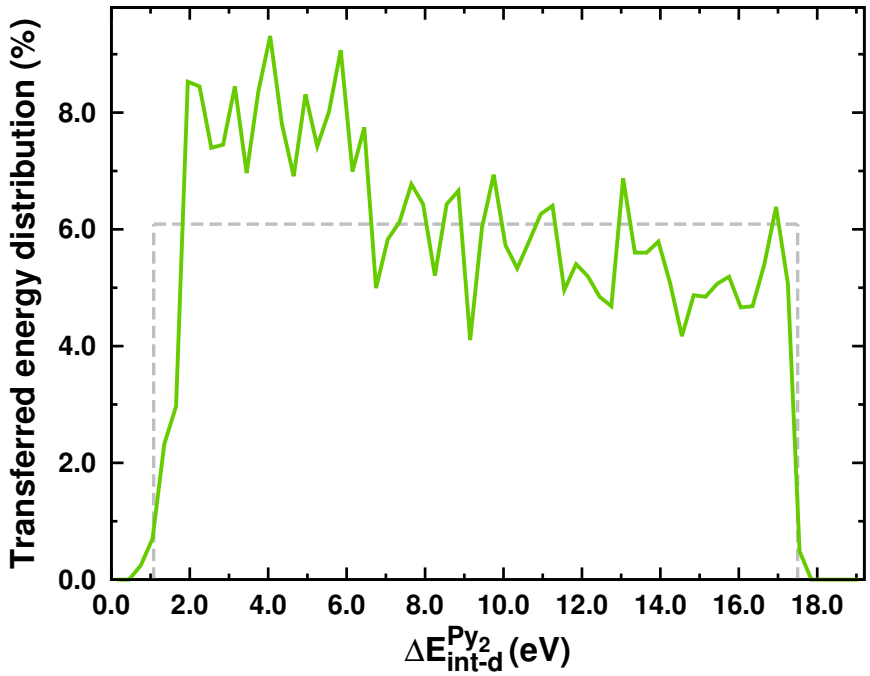

Figure 4.26: Distribution of transferred energy in rovibrational modes $\Delta E_{int}^{Py_2}$ for trajectories leading to dissociation at the end of MD (center of mass collision energy of 17.5 eV). The dashed line shows the distribution of transferred energy used in the LOC model.

(ii) the smallest (6.82 Å) or (iii) largest pyrene axes (9.25 Å) leading to distances of 3.40, 5.29 and 6.50 Å, respectively. Below 3.40 Å, all trajectories involve a frontal impact of the argon on the dimer carbonaceous system and almost all of them lead to dissociation. Unexpectedly, the opacity curve drops to zero at 5.5 Å which is lower than the largest computed value of 6.5 Å. Interestingly, taking the largest distance between carbon atoms in pyrene (7.0 Å) instead of that between hydrogen atoms (9.25 Å) leads to a value of 5.4 Å which is in line with the opacity curves. This suggests that the dissociation is efficient only if the carbonaceous skeleton area is impacted, the impact in the region of external hydrogen atoms resulting mostly in an intramolecular C-H mode excitation at the expense of dissociative modes. As a conclusion, it seems that for energies larger than 10 eV, the opacity curves are similar as they are driven by simple geometric rules, in other words, if the dimer receives a direct impact of the argon on the carbonaceous skeleton area, it will dissociate. Interestingly, this seems to be in agreement with previous works [483, 485] which also pointed out the efficient nuclear stopping power of carbon atoms in a very different context (higher energy collisions leading to knock-out process).

The blue curve in Figure 4.29 shows the MD dissociation cross sections of pyrene dimers

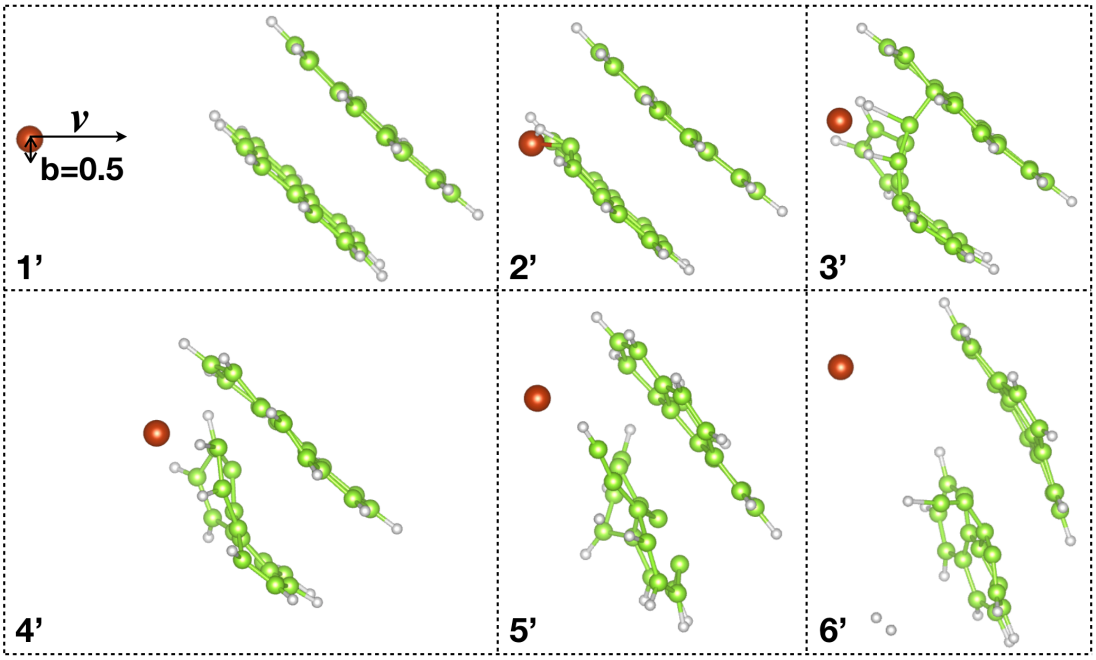

Figure 4.27: Snapshots for molecular dynamics trajectory with impact parameter of 0.5 Å and a collision energy of 27.5 eV leading to intramolecular fragmentation.

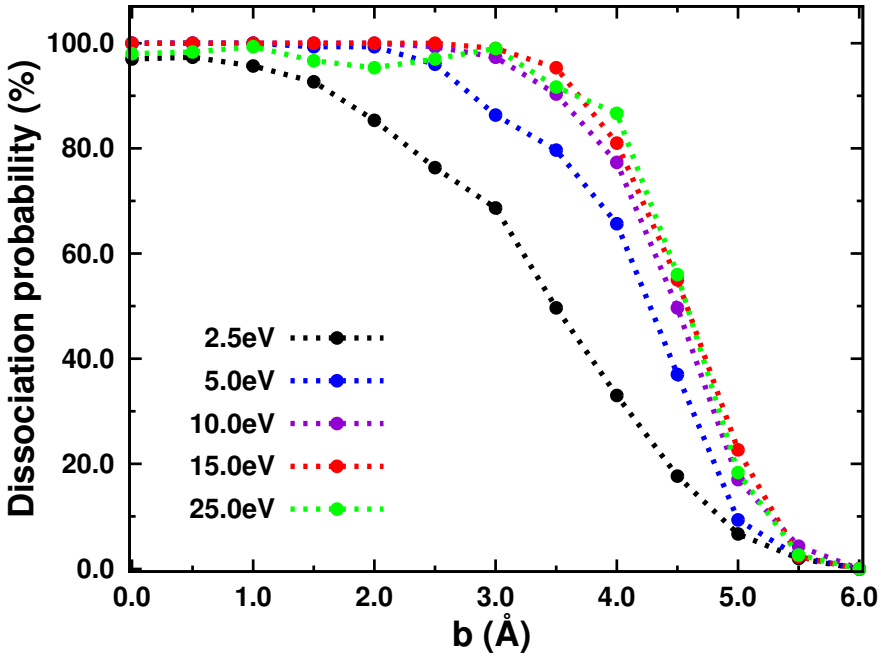

Figure 4.28: Opacity curves as a function of the impact parameter *b* for several selected center of mass collision energies.

obtained from the opacity curves following eq. 4.3. It presents a steep increase for energies bellow 7.5 eV before remaining almost constant around 65 Å^2 for collision energies greater than 10-15 eV. This is a direct consequence from the already discussed similarity of opacity curves for the high collision energies. The purple curve corresponds to dissociation at infinite timescales. Figure 4.29 also reports the cross sections computed from the MD+PST model. It can be seen that, for low collision energies, the MD and MD+PST cross sections are very close, indicating that most of the dissociations occur on the short timescales. On the opposite, at high collision energies, a non-negligible fraction of the dimers, which are not dissociated at the end of the MD simulation, carry enough energy to evaporate on the experimental timescales. At the experimental center of mass collision energy of 17.5 eV, the MD+PST cross section (about 70 Å^2) is slightly above the pure MD dissociation ratio, which indicates that the dissociation at long timescales represents a small fraction of the dissociated pyrene dimers as already seen from the TOF spectra analysis (see Figure 4.24).

I have also plotted in Figure 4.29 the model cross section σ_∞ that successfully reproduced the threshold collision-induced dissociation experimental results [65]. This model cross section is obtained by considering that the collision energy transfer is given by the LOC model and the expression for the cross section is given by:

$$\sigma_{LOC}(E_{col}) = \sigma_0(E_{col} - D)/(E_{col}). \tag{4.12}$$

where $D = 1.08$ eV is the dissociation energy [65, 457] and $\sigma_0 = 63$ Å^2 is a scaling factor usually thought as the geometrical cross section. This model cross section is usually further convolved with dissociation rates, collision energy distributions and internal energy distributions in order to be compared with experimental results. However, since here for the theoretical calculations there is no collision energy distribution, this curve could in principle be directly compared with the purple one in Figure 4.29, namely the cross section for infinite time. One can see that the MD, MD+PST results and the model cross section have similar collision energy dependence. The magnitude of the two cross sections is rather different at high collision energy, with about 60 Å^2 and 74 Å^2 for the model and infinite timescale cross sections respectively. Nevertheless, this difference is probably within the error bars of the experimental cross section measurement.

The dissociation cross sections for MD timescales with time step being 0.1 fs at collision energy of 20 and 25 eV ($\sigma_{\mathrm{MD}}(0.1)$) in Figure 4.29 are close to the ones of time step being

0.5 fs (σ_{MD}), which indicates a time step of 0.1 fs used in the MD simulation does not change significantly the corresponding dissociation cross section.

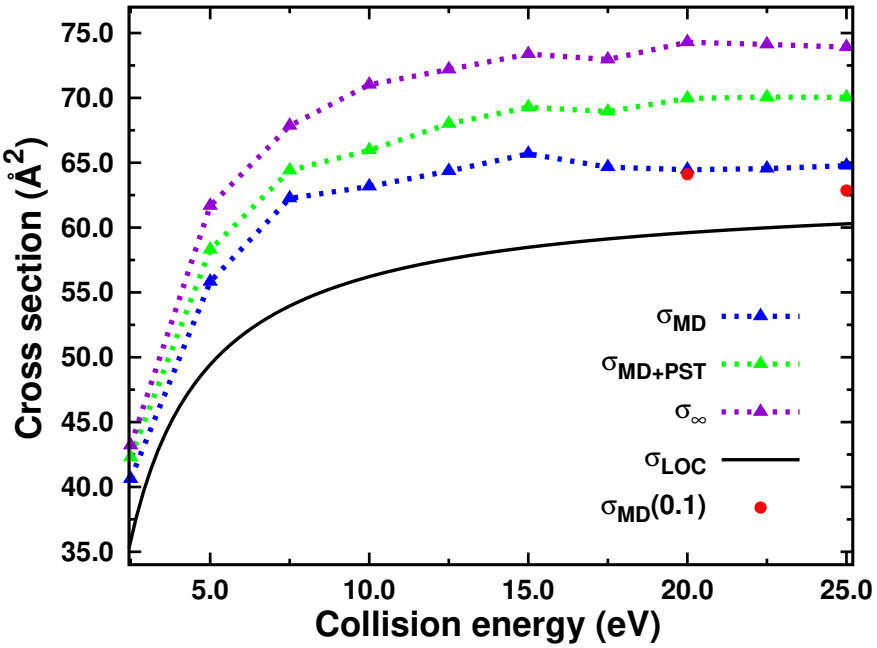

Figure 4.29: Dissociation cross sections of Py_2^+ after collision with argon as a function of center of mass collision energy for the short (MD), experimental (MD+PST) and infinite timescales. Cross sections resulting from the LOC model are also plotted. σ_{MD} (0.1) denotes the dissociation cross section for short (MD) timescale with a time step of 0.1 fs.

Energy partition

The mean value obtained for the transferred energy after removing the translation kinetic energy of the dimer, namely $\Delta E_{int}^{Py_2}$, is plotted in Figure 4.30 as a function of the collision energy. Although this quantity evolves almost linearly with the collision energy, the curves are different when one considers only the trajectories leading to dissociation or non-dissociation. For trajectories where the dimer does not dissociate, $\Delta E_{int-ud}^{Py_2}$ remains small for all collision energies below 20 eV and shows a very slight increase for collision energies larger than 20 eV. For trajectories leading to dissociation, $E_{int-d}^{Py_2}$ grows almost linearly, but above 10-15 eV most of the absorbed energy is actually used to heat the individual monomers (the green curve) whereas the energy given in the dissociative mode (difference between the blue and green curves) remains almost constant. I note that, despite the trends of the mean energy values derived from all simulations or restricted to the undissociated cases are interesting, their absolute values have

small meaning as they depend on the arbitrarily chosen b_{max} value, *i.e.* increasing b_{max} would result in more undissociated trajectories with less and less energy transfer. On the opposite, absolute values of mean energies for the dissociation trajectories are relevant, as increasing the b_{max} value would not result in new dissociation trajectories.

For MD simulations with time step being 0.1 fs at collision energy of 20 and 25 eV, the corresponding energies in Figure 4.30 are close to the ones of time step being 0.5 fs, which indicates a time step of 0.1 fs used in the MD simulation does not change significantly the corresponding deposition of the total transferred energy.

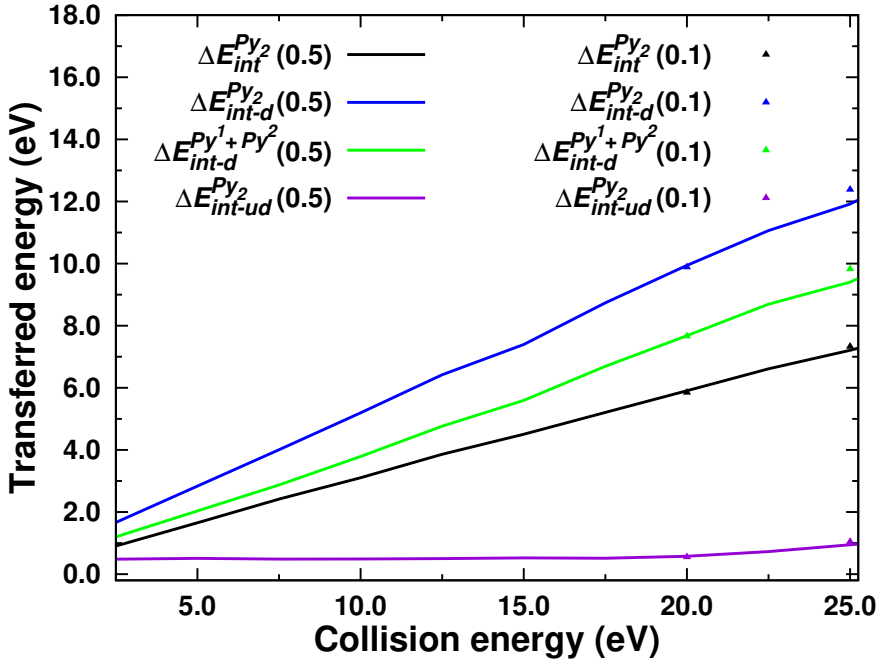

Figure 4.30: At the end of the MD collision simulations with a time step of 0.1 and 0.5 fs, the total transferred energy $\Delta E_{int}^{Py_2}$ to the rovibrational modes or restricted to the sole dissociated ($\Delta E_{int-d}^{Py_2}$) or undissociated ($\Delta E_{int-ud}^{Py_2}$) pyrene dimers as a function of collision energy. The transeferred energy to the monomers rovibrational modes for the dissociated dimers $\Delta E_{int-d}^{Py^1+Py^2}$ is also plotted.

It is also interesting to focus on the kinetic energy partition, in particular because its decomposition in sub-contributions (dissociative vs non-dissociative modes) is easier (see eqs. 4.5) than that of the potential (and consequently total) energy. For each simulated collision energy, the values for the kinetic energy sub-contributions (eqs. 4.5) are averaged over all the trajectories and reported in Table 4.5 and Figure 4.31. In addition, the averaged kinetic energy sub-contributions are also calculated over the dissociated and undissociated trajectories

Table 4.5: The kinetic energy partition after the collision of pyrene dimer with argon at different collision energies E_{col}. All energies are in eV.

E_{col}	E^k_{td}	E^k_{Ar}	$E^k_{Py^1}$	$E^k_{Py^2}$	E^k_{Re}
2.5	0.17	1.67	0.25	0.25	0.19
5.0	0.30	3.52	0.40	0.41	0.41
7.5	0.42	5.38	0.55	0.56	0.64
10.0	0.53	7.32	0.71	0.70	0.80
12.5	0.65	9.20	0.89	0.88	0.95
15.0	0.74	11.20	1.03	1.03	1.06
17.5	0.82	13.16	1.16	1.22	1.18
20.0	0.89	15.12	1.37	1.32	1.30
22.5	0.96	17.09	1.52	1.51	1.36
25.0	1.01	19.18	1.61	1.69	1.45

separately for each simulated collision energy. Then sum the contributions of dissociated and undissociated trajectories (black curves in Figure 4.31) calculated by the following eqs 4.13,

$$\begin{aligned} E^k_1 &= E^k_{td-d} * P + E^k_{td-ud} * (1-P) \\ E^k_2 &= E^k_{Re-d} * P + E^k_{Re-ud} * (1-P) \\ E^k_3 &= (E^k_{Py^1} + E^k_{Py^2})_{-d} * P + (E^k_{Py^1} + E^k_{Py^2})_{-ud} * (1-P) \end{aligned} \tag{4.13}$$

where P refers to the dissociation probability at a given center of mass collision energy. The results of sum the contributions of dissociated and undissociated trajectories are the same with the ones over all the trajectories (see Figure 4.31). This ensures our calculations for the mean kinetic energy sub-contributions are right.

The comparison of these kinetic energy sub-contributions between the time step being 0.1 and 0.5 fs used in the MD simulations is shown in Table 4.6 and Figure 4.32, which indicate a time step of 0.1 fs almost didn't affect the results of kinetic energy sub-contributions.

In Figure 4.33 are reported the ratios of the pyrene dimer translational kinetic energy E^k_{td}, relative kinetic energy E^k_{Re} and monomers rovibrational kinetic energies $E^k_{Py^1} + E^k_{Py^2}$ over the total pyrene dimer kinetic energy $E^k_{tot} - E^k_{Ar}$. It clearly appears that, whereas the contribution of the dimer translation kinetic energy (E^k_{td}) remains almost constant (very slight decrease from

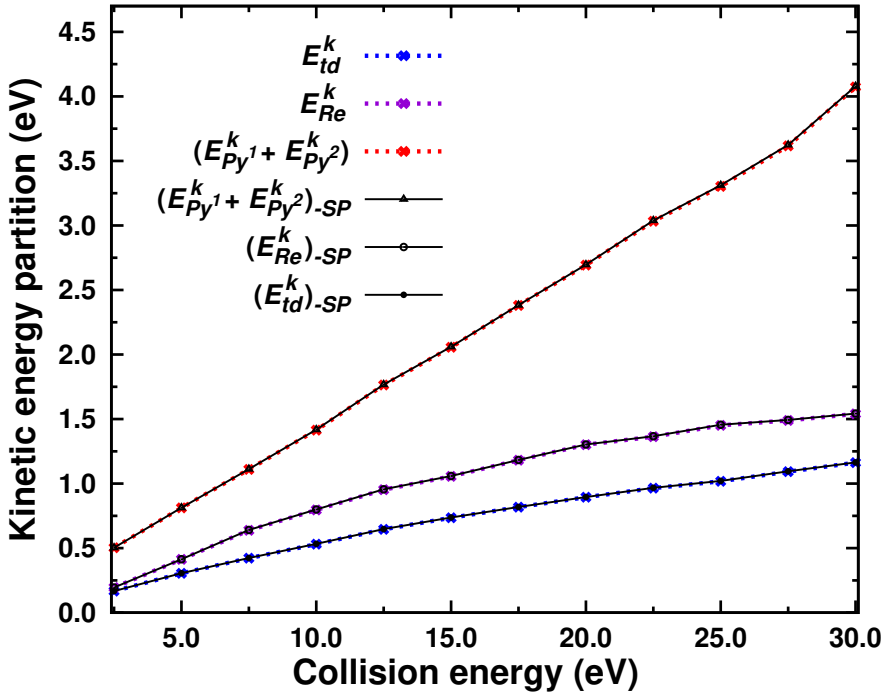

Figure 4.31: Mean kinetic energy partition at the end of the MD simulations.

about 20% to 18% of the dimer kinetic energy), this is not the case for the other two contributions. For collision energies below 7.5 eV, the proportion of the kinetic energy associated to the center of mass relative velocities increases whereas the opposite is observed for the monomers rovibrational kinetic energy. These two trends are reversed above 7.5 eV.

Again, it is convenient to analyse separately the kinetic energy partition for trajectories leading to dissociation or not as done in Figure 4.34 for E^k_{td}, E^k_{Re} and $E^k_{Py^1} + E^k_{Py^2}$. For both dissociated and undissociated trajectories, the total energy in the system computed from the initial energy at 25 K (0.32 eV) plus the transferred energy is twice the final kinetic energy computed from velocities shown in Figure 4.34 (black curves). This is exactly what one should expect from the Virial theorem.

In the absence of dissociation, the transferred energy is either small or redistributed over all the vibrational modes of the dimer, leading to small values for E^k_{Re-ud} (mean value always below 0.04 eV). The monomers rovibrational kinetic energies remain constant with an increase for collision energies above 20 eV, indicating that the slight increase of transferred energy results in a heating of the monomers, as already inferred from Figure 4.30. Once a dimer dissociates, the two pyrene molecules relative kinetic energy E^k_{Re-d} can not be transferred back

Table 4.6: The kinetic energy partition and cross section at the end of MD simulations with time step being 0.1 and 0.5 at different collision energies of 20 and 25. All energies are in eV. Time step ($Tstep$) is in fs. Cross section σ_{MD} is in Å.

E_{col}	$Tstep$	E^k_{td}	E^k_{Ar}	$E^k_{Py^1}$	$E^k_{Py^2}$	E^k_{Re}	σ_{MD}
20.0	0.1	0.89	15.18	1.34	1.35	1.28	64.11
20.0	0.5	0.89	15.12	1.37	1.32	1.30	64.45
25.0	0.1	1.03	19.04	1.71	1.67	1.44	62.86
25.0	0.5	1.01	19.18	1.61	1.69	1.45	64.77

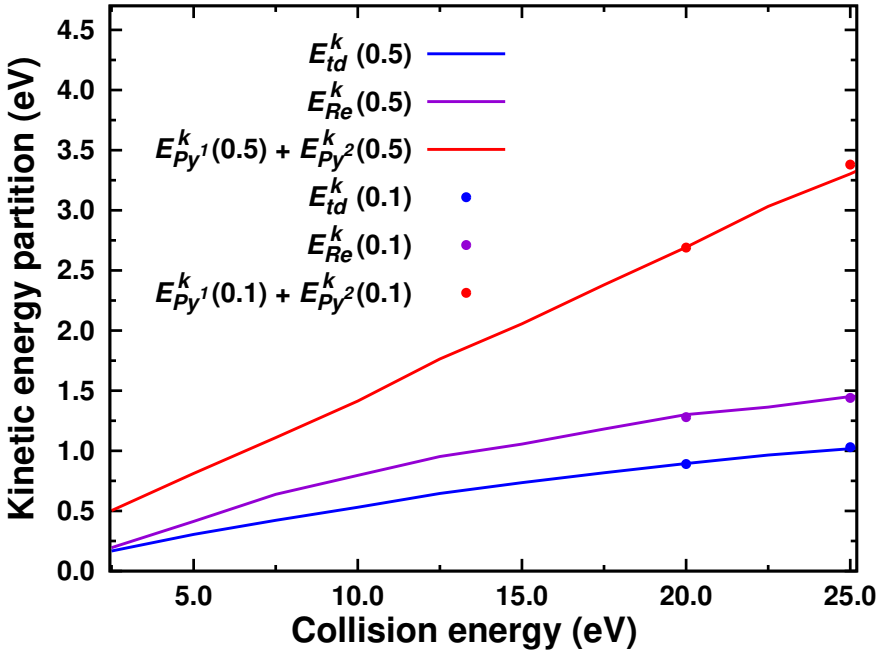

Figure 4.32: Mean kinetic energy partition at the end of the MD simulations with time step being 0.5 fs at the center of mass collision energy from 2.5 to 25 eV. The mean kinetic energy partition with time step being 0.1 fs at center of mass collision energies of 20 and 25 eV are plotted with filled round circles.

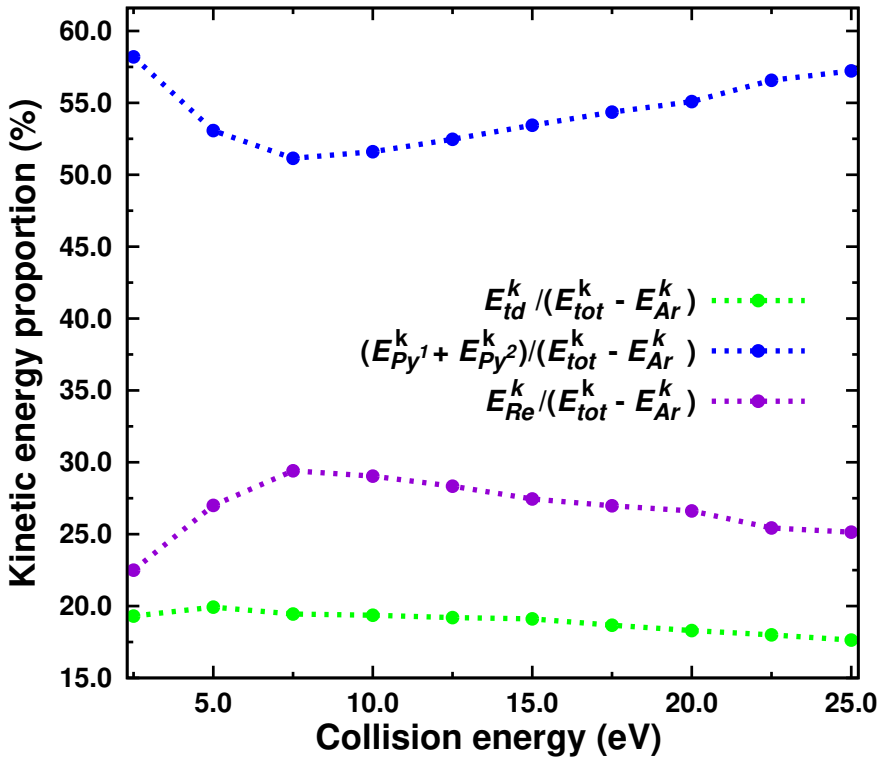

Figure 4.33: Kinetic energy proportion after collision of Py_2^+ with argon as a function of collision energy.

to the intramolecular modes and its mean value is never negligible with respect to the monomers rovibrational kinetic energies $(E^k_{Py^1} + E^k_{Py^2})_{-d}$. However, although the slope of $(E^k_{Py^1} + E^k_{Py^2})_{-d}$ remains constant with collision energies, that of E^k_{Re-d} decreases clearly. This is in line with the analysis of Figure 4.30, which shows the amount of energy transferred to the dissociative modes remains constant for high collision energies whereas the monomers are getting more internal energy.

Finally, some characteristic timescales are computed, which are presented in Figure 4.35. They correspond to the timescales for the argon with its initial velocity to travel across some characteristic distances, namely, a C-H (1.10 Å) or a C-C bond (1.40 Å) and the largest molecular axis (9.25 Å). These timescales can be compared with those of the pyrene dimer vibrational modes as an efficient energy transfer would be favored by similar orders of magnitudes. The intermolecular dimer modes possibly mixed with very soft folding modes are lying within the 70-120 cm^{-1} spectral range [480] with corresponding half-periods of 130-240 fs. These timescales are of the same order of magnitude as the time for the argon to travel across the

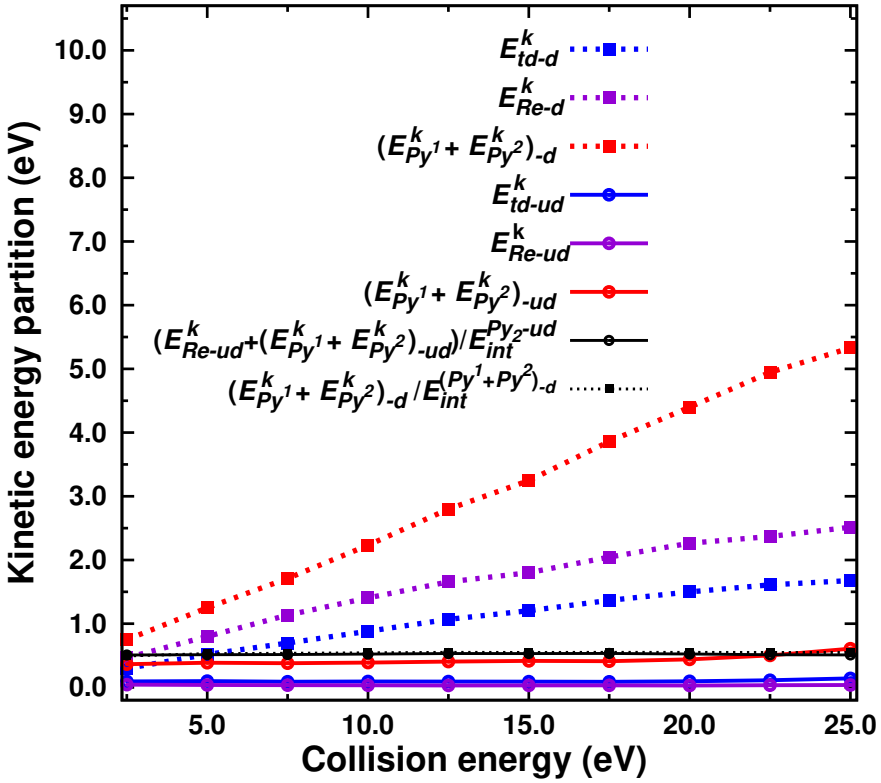

Figure 4.34: Kinetic energy partition for dissociated (-d) and undissociated (-ud) trajectories at the end of the MD simulation as a function of collision energy.

largest pyrene axis for collision energies below 10 eV. Typical frequencies for intramolecular non-soft modes are lying from 500 cm^{-1} to 3000 cm^{-1} (C-H stretching modes), leading to half-periods of 5-33 fs. For all the simulated collision energies, the characteristic times required for the argon to travel across typical C-H or C-C bond distances belong to the same order of magnitude as some of the intramolecular hard modes. Therefore, it appears from this qualitative description that the collision energy transfer toward the intermolecular modes is easier at collision energies lower than 10 eV whereas the transfer toward intramolecular modes is efficient for all the simulated collision energies. This is actually in line with the fact that the part of the absorbed collision energy taken by the non-soft intramocular modes is increasing with the collision energy at the expense of that taken by the intermolecular and soft intramolecular modes, which is in agreement with the previous energy analysis (Figures 4.30, 4.33 and 4.34).

Efficiency of energy transfer within the dimer

In this section, I address how the energy is shared inside the dimer after the collision. In par-

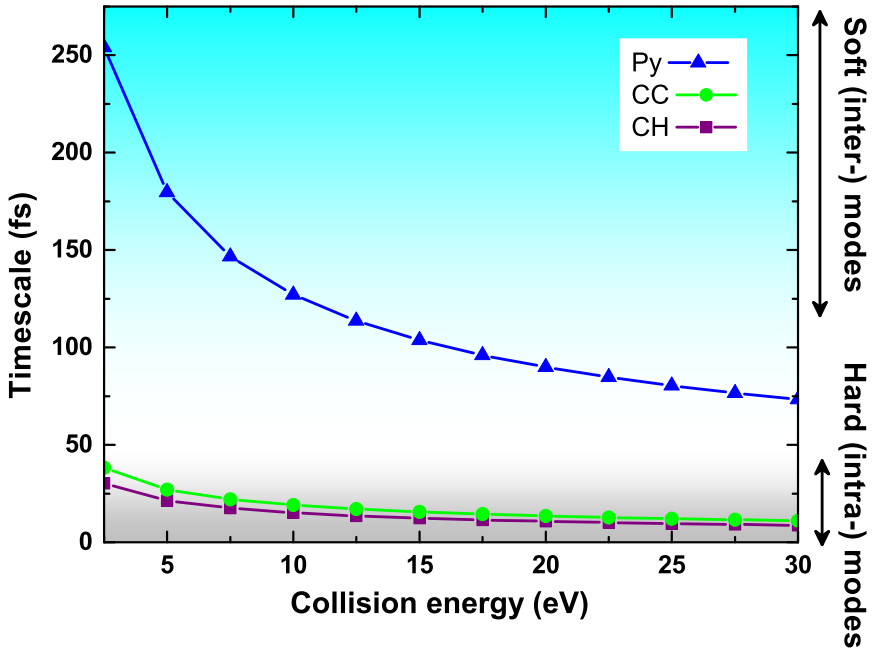

Figure 4.35: Timescales, as a function of center of mass collision energy, for argon to travel across some typical distances: a carbon-carbon bond (green), a carbon-hydrogen bond (purple) or the largest axis of the pyrene molecule (blue).

ticular, I look at the efficiency of energy transfer between the intramolecular modes of each unit and the intermolecular modes. The amount of deposited energy as well as its partition between the intramolecular modes of each molecule and the intermolecular modes is strongly dependent on the collision condition: the impact parameter, the orientation of the dimer, whether a head on collision occurs with one of the dimer atoms (and its nature, carbon or hydrogen). This results in very different evolutions of the subsequent energy flows for which precise values concerning timescales can hardly be derived. Nevertheless, the analysis of the trajectories allows to identify some characteristic behaviors. In order to estimate the thermalization process efficiency, the instantaneous intra and intermolecular kinetic temperatures are evaluated using the following formula:

$$T^k = 2\frac{< E^k >}{nk_b} \tag{4.14}$$

where k_b refers to the Boltzmann constant. n is the number of involved modes and E^k is the kinetic energy for the intra or intermolecular modes (see eqs. 4.5). T^k is plotted in Figure 4.36 for some selected trajectories obtained for collision energies of 22.5 eV and various impact pa-

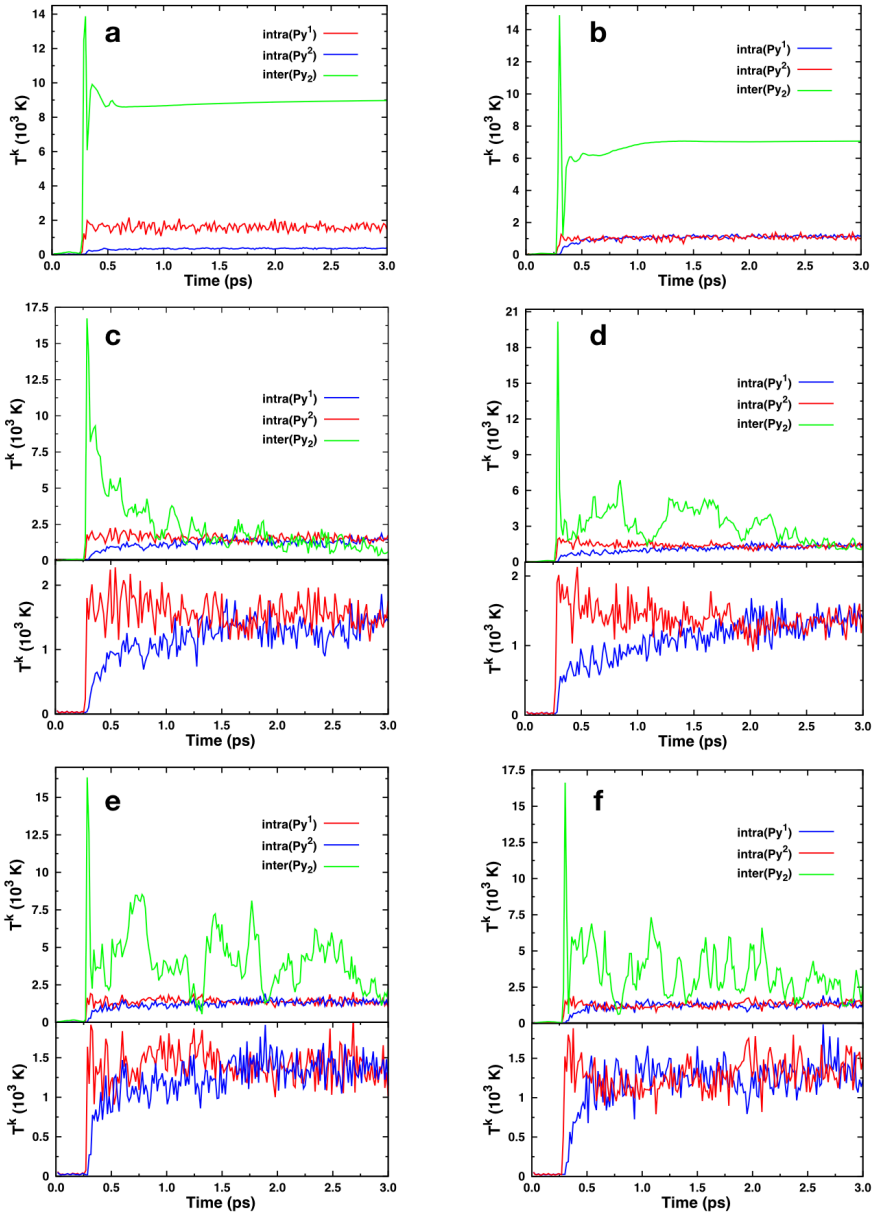

Figure 4.36: Instantaneous kinetic temperatures as a function of time for intra and intermolecular modes of the pyrene dimer at a collision energy of 22.5 eV. Impact parameters *b* are (a) 2, (b) 3, (c) 0, (d) 2.5, (e) 2, and (f) 2 Å. In cases (a) and (b) dissociation takes place whereas in the other cases the dimer remains undissociated at the end of the MD simulation. In (c) to (f) the lower panel is a vertical zoom of the corresponding intramolecular parts in upper panel.

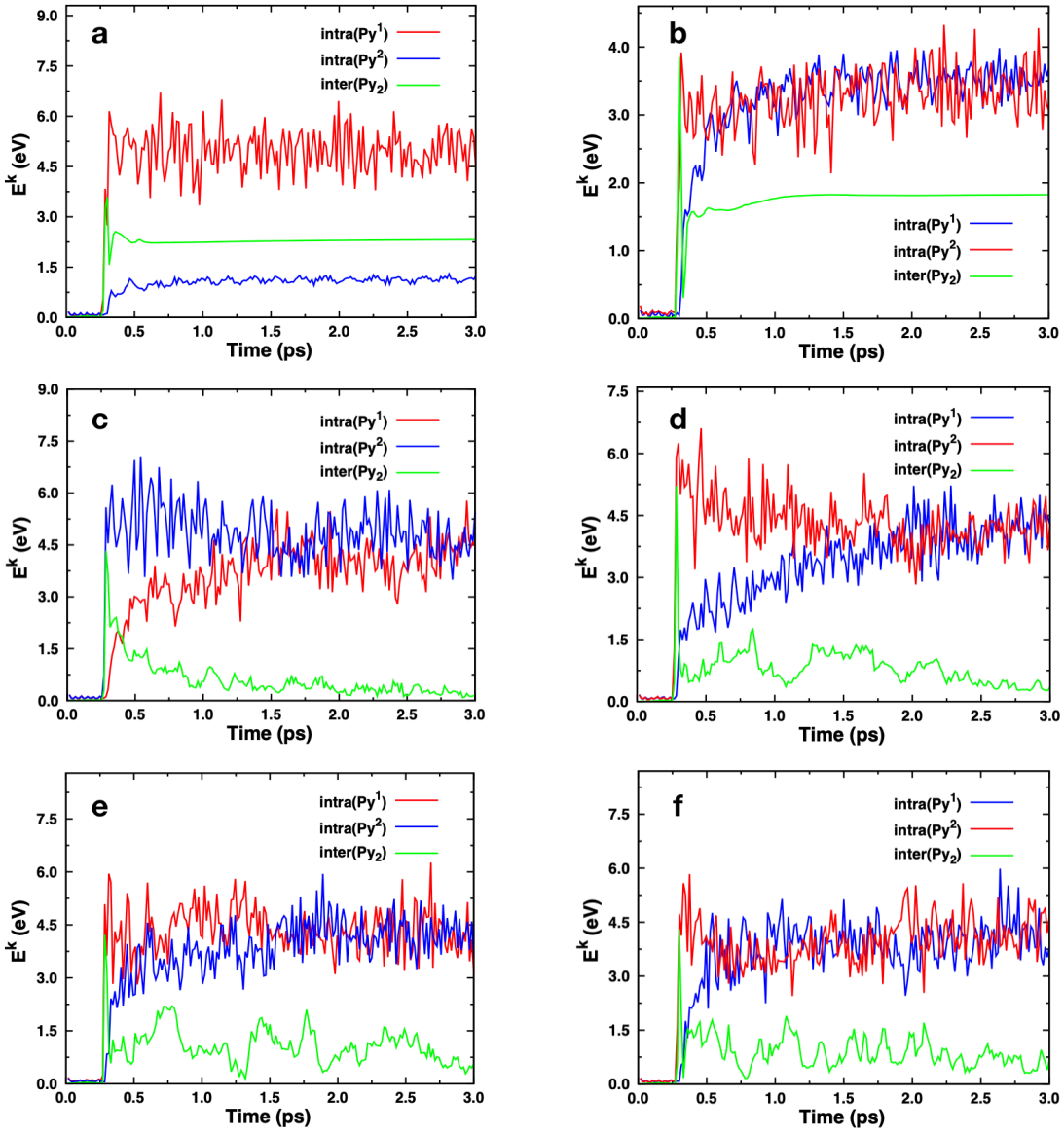

Figure 4.37: Instantaneous kinetic energies as a function of time for intra and intermolecular modes of the pyrene dimer at a collision energy of 22.5 eV. Impact parameters *b* are (a) 2, (b) 3, (c) 0, (d) 2.5, (e) 2, and (f) 2 Å. In cases (a) and (b), dissociation takes place whereas in the other cases the dimer remains undissociated at the end of the MD simulation.

rameters. The evolution of the corresponding energies ($E^k_{intra^1}$, $E^k_{intra^2}$ and E^k_{inter}) are presented in Figure 4.37. In Figures 4.36 and 4.37, simulations (a) and (b) correspond to trajectories for which dissociation occurred, whereas the dimer remained intact in the other simulations. In the simulation (a), a larger amount of energy is deposited in the first monomer with respect to the second one. The dissociation occurs before an efficient energy transfer takes place between the two monomers, leading to one hot monomer and one cold monomer at the end of the simulation. The situation is slightly different in the dissociation trajectory (b): there is a much smaller difference between the energies received during the collission by each of the monomers. One can observe that the equilibration of the two monomers intramolecular energies can take place before dissociation, leaving the two monomers with similar energies/kinetic temperatures. In the other four pictures (c, d, e, and f), corresponding to undissociated trajectories, one can see that the thermalization between the two monomers intramolecular modes occurs with timescales from 0.2 to 1.5 ps shown in Figure 4.36. On the other side, the energy equilibration between intra and intermolecular modes takes more time. Indeed, the thermalization is almost achieved in simulations (c) and (d) at 1.5 and 2.5 ps, respectively, but would take more than the simulated duration 3 ps for trajectories (e) and (f) displayed in Figure 4.36. As a conclusion of these trajectories analyses, it seems that the thermalization between intramolecular modes of the two monomers is relatively efficient (on the order of ps). On the other hand, the thermalization with the intermolecular modes is less efficient and sometimes is not observed during the simulated time of 3 ps. The direct dissociation of the dimer is a fast process (on the order of a few tenths of ps) which may prevent the thermalization taking place, leading to monomer temperatures reflecting the initial energy deposition.

4.4.5 Conclusions about CID of Py_2^+

A QM/MM dynamics study of the collision of Py_2^+ with argon at various collision energies were carried out. Argon was treated as a polarisable MM particle and Py_2^+ was treated using the SCC-DFTB method. In the dynamical simulations, a time step of 0.5 fs is proper even for high collision energies 25 eV. The TOF mass spectra of parent Py_2^+ and dissociation product Py^+ were simulated by the PST using the MD outputs at a centre of mass collision energy of 17.5 eV. With respect to TOF mass spectra extracted from pure PST simulations, considering non-statistical dissociation processes that take place before the energy redistribution from MD simulations improves the match between experimental and theoretical TOF spectra. The agreement between the measured and simulated mass spectra peak shapes and positions shows